

Document downloaded from:

<http://hdl.handle.net/10251/165302>

This paper must be cited as:

Niu, J.; Albero-Sancho, J.; Atienzar Corvillo, PE.; García Gómez, H. (2020). Porous Single-Crystal-Based Inorganic Semiconductor Photocatalysts for Energy Production and Environmental Remediation: Preparation, Modification, and Applications. *Advanced Functional Materials*. 30(15):1-51. <https://doi.org/10.1002/adfm.201908984>



The final publication is available at

<https://doi.org/10.1002/adfm.201908984>

Copyright John Wiley & Sons

#### Additional Information

This is the peer reviewed version of the following article: Niu, J., Albero, J., Atienzar, P., García, H., Porous Single-Crystal-Based Inorganic Semiconductor Photocatalysts for Energy Production and Environmental Remediation: Preparation, Modification, and Applications. *Adv. Funct. Mater.* 2020, 30, 1908984, which has been published in final form at <https://doi.org/10.1002/adfm.201908984>. This article may be used for non-commercial purposes in accordance with Wiley Terms and Conditions for Self-Archiving.

**Porous single crystal based inorganic semiconductor photocatalysts for energy production and environmental remediation: preparation, modification and applications**

*Jinan Niu\* Josep Albero, Pedro Atienzar and Hermenegildo García\**

Dr. J. Albero, Dr. P. Atienzar and Prof. H. García  
Instituto Universitario Mixto de Tecnología Química (UPV-CSIC), Universitat Politècnica de València, Avda. de los Naranjos s/n, 46022, Valencia (Spain).  
E-mail: hgarcia@qim.upv.es

Prof. J. Niu  
School of Materials Science and Engineering, China University of Mining and Technology, Daxue Road, No. 1, Xuzhou, Jiangsu (China).

Keywords: photocatalysis, single crystal, environmental remediation, photovoltaics, solar fuels

Semiconductor photocatalytic and photovoltaic performance depends on a large extent on crystallinity and surface area. One strategy to improve semiconductor photoresponse efficiency that has recently emerged is their synthesis as porous single crystals (PSCs), therefore enjoying simultaneously high crystallinity, minimization of grain boundaries and large specific surface area. Other factors, such as high density of active sites, high dye loading and enhanced light absorption, also contribute to increase PSC photoresponse respect to analogous bulk or amorphous materials. The present review starts presenting the concept and main properties of PSCs. The two main sections are the description of the synthetic routes and the applications as photocatalysts and in photovoltaic devices, mainly in sunlight applications. The synthetic procedures have been classified according to the mechanism of pore generation. Applications cover photocatalysis for environmental remediation, solar fuels production, selective photooxidation of organic compounds and photovoltaic devices. The conclusion section summarizes the review and provides views on future development. The purpose of the review is to show how the use of PSCs is a powerful general methodology applicable beyond metal oxides and can ultimately lead to sufficient photoresponse efficiency to bring some of these processes close to commercial application.

## 1. Introduction

There is a continuous effort aimed at increasing the photoresponse of semiconductors. Among the main parameters that influence semiconductor efficiency, crystallinity and surface area play a major role. Crystallinity determines the charge separation/recombination rate and charge mobility, while high surface area is necessary for efficient interfacial charge transfer processes beyond the particle domain. One recent strategy to improve semiconductor photoresponse performance is to synthesize these materials as porous single crystals (PSCs), providing simultaneously high crystallinity, minimization of grain boundaries and large specific surface area. The present review describes the current state of the art in the synthesis procedures and application of PSCs as photocatalysts and in photovoltaic devices. It would be shown that the combination of crystallinity and porosity determines an improved performance of the semiconductor response respect to analogous bulk materials.

The first example of PSCs was probably reported by Domen et al. in 2002. This study described the synthesis of (Nb, Ta)<sub>2</sub>O<sub>5</sub> PSCs obtained using the block co-polymer HO(CH<sub>2</sub>CH<sub>2</sub>O)<sub>20</sub>(CH<sub>2</sub>CH(CH<sub>3</sub>)O)<sub>70</sub>(CH<sub>2</sub>CH<sub>2</sub>O)<sub>20</sub>H as structure directing agent (SDA) through first formation and aging of the metal oxide and then calcination.<sup>[1]</sup> This work opened the door to elaborately regulate simultaneously the microstructure of materials with respect to continuity and porosity. However, the booming in this area seems to begin in 2013, when Snaith et al reported the synthesis of the uniform anatase TiO<sub>2</sub> mesoporous single crystals (MSCs).<sup>[2]</sup> The reasons for the impact of this contribution derives from the preponderance of TiO<sub>2</sub> as semiconductor in renewable energy and environment remediation due to its low cost, high chemical stability and band structure,<sup>[3]</sup> finding applications in solar cells, gas sensors and photoelectrocatalysis).<sup>[2, 4]</sup> The TiO<sub>2</sub> PSCs synthesized by Snaith et al have truly attractive

appearance with a perfectly defined crystalline shape and uniform pore distribution.<sup>[2]</sup> Since then, various preparation methods for other PSCs with different morphologies have been described showing the potential application in a wide range of areas.

In the current literature there are different definitions for PSCs that make the situation confusing. Herein, to clearly present the current development in the field of PSCs, three points are previously discussed before giving the definition of PSCs adopted in the present review.

#### (1) Crystals or crystal?

In an ideal situation, only one big crystal with continuous end-to-end pores endowing the materials with large surface area and good interconnectivity would be enough for some applications, for example as the anode of a solar cell. In this case, only one TiO<sub>2</sub> crystal on the surface of conductive fluor-doped tin oxide (FTO) glass would afford probably the highest efficiency of the whole device due to the absence of grain boundaries. For this ideal case, the word “crystal” appears as the most appropriate because the material consists only of one particle. However, in real situations powdered materials contain a large number of small crystalline particles, whose sizes range up to several tens of micrometers, but rarely reaching millimetric length. Therefore, it is reasonable to use “crystals” to describe multi particulate powdered materials. Note that in some specific context, the use of “crystals” or “crystal” will depend on the number of particles discussed within a multi particulate material. For example, “crystal” should be used when the focus is on a single particle in a microscopic analysis.

#### (2) Alternative terms for “single crystals”

Currently, there are at least four alternatives to denote this type of topical materials, (i) single crystals, (ii) monocrystals, (iii) single crystal-like and (v) quasi-single crystals. “Single crystals” and “monocrystals” seem to have the same meaning, both of which can correctly reflect the absence of different crystalline domains within the limits defined by the particle surface, the whole material comprising many small single crystals. When compared with “monocrystals”, “single crystals” seems easier to be understood, so it is the term used in most

of the papers in the field and also the one adopted in this review. In some studies, PSCs were actually obtained according to micrographic and structural data, but authors have preferred to use “single crystal-like” or “quasi-single crystalline” to describe these powdered materials in order to distinguish them from the ideal case of a single crystal of millimetric dimensions.<sup>[5]</sup> However, adopting here any of these two terms may result in some confusion because aggregates of nanocrystals forming larger particles have also been described as “single crystal-like” or “quasi-single crystalline” in some other papers, meaning in these cases that there is not only one crystal in the particle.<sup>[6]</sup> This review covers those materials called as “single crystal-like” or “quasi-single crystalline” when the study includes specific evidence regarding single crystal structure in each individual particle. Another word, “mesocrystal” describes aggregation of nanocrystals with the same crystalline orientation in each individual crystal of the aggregate, which usually has a clear analogy as a single crystal and can also be confused with PSCs. The most obvious difference between “mesocrystal” and “porous single crystal” is the presence of grain boundaries. In selected area electronic diffraction (SAED), a mesocrystal particle displays a set of spots similar to the case of a single crystal, being necessary to observe grain boundaries to correctly distinguish it from a single crystal of similar size.<sup>[7]</sup> However, very frequently the spots for mesocrystals are elongated and less clearly defined. This feature can also be used to distinguish mesocrystals from a single crystal, as it reflects the existence of boundaries of small particles. In this review, the papers regarding mesocrystals applied in solar utilization will not be covered so that our scope is better focused on PSCs.

### (3) Pores in crystals

The word “porous” in PSCs means internal voids within each crystal that allows mass transfer from the exterior to intracrystalline position. This definition does not include the voids among individual crystals. Accordingly, studies regarding aggregation of dense single-phase nanocrystals defining interparticle voids are not included in this review. In addition, since the

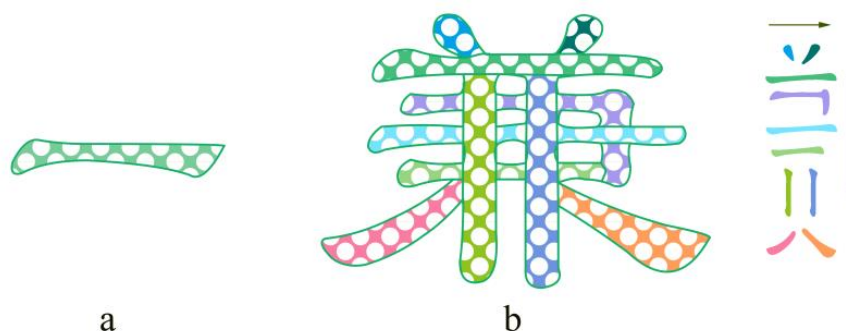
pore sizes of PSCs can have different length scale, several prefixes to modify the word “porous”, for example “mesoporous” and “microporous” can be adopted to indicate the pore size<sup>[5a]</sup>. In order to cover single crystals with different pore sizes, a more general name, “porous single crystals” is adopted here. It should be indicated at this point that due to the existence of several recent reviews and the general lack of photoresponse,<sup>[8]</sup> the present article does not include the field of PSCs of zeolites, but focus specifically on inorganic semiconductors such as metal oxides, nitrides, oxynitrides, chalcogenides, titanates and vanadates, among others. For these materials, pore dimensions are more frequently nanopores due to the current limitations in the synthetic methods and the sizes of formed crystals. However, this pore range and the corresponding specific surface area appear to be suitable for many applications, particularly for solar energy utilization that is the target of the present review.

## 2. Basic features of PSCs

### 2.1. PSCs definition

Based on the above discussion, *porous single crystals* can be defined as a kind of unique materials comprising simultaneously single-crystal particles with porous structure. This definition is rather general and comprehensive. Accordingly, zeolites, metal organic framework (MOFs) among other solids can also be considered as PSCs, and the semiconducting inorganic materials reviewed in this work are just a subclass of PSCs family characterized by their photoresponse. In summary the key point to classify a material as PSCs is to determine for each particle a single crystalline domain and porosity. Scheme 1 illustrates the PSC definition adopted in this manuscript. In this, two Chinese characters, “Yi” and “Jian”, have been represented. ‘Yi’ means ‘single’, while ‘Jian’ means ‘possessing two or

more features at the same time'. Thus, ten different "Yi" characters have formed the character "Jian", representing an aggregate of ten PSCs exhibiting different features.



**Scheme 1.** Schematic illustration of (a) a 'Yi'-shaped PSC, and (b) a 'Jian'-shaped aggregate consisting of ten PSCs as example of the PSC definition presented in this manuscript.

## 2.2. Main aspects of PSCs

Porosity and lattice-continuity are, therefore, the two basic features of PSCs. On one hand, these two features directly determine the fundamental properties of PSCs as semiconductor; on the other hand, they also determine ways to prepare PSCs and where to apply these materials.

### 2.2.1. Porosity

The porosity is closely linked to high specific surface area and the possibility of mass transfer from the outer to inner crystal space. For the **nonporous bulk crystals**, exposure of high energy facets, doping and other structural modifications can improve their activity, but they are **typically characterized by a relatively small surface area**. Porosity can in an effective way overcome this shortcoming of nonporous materials. Note that it is not always true that PSCs with the largest surface area exhibit the highest activity, because other factors such as pore dimensions can also play a role, hindering, for instance, mass transfer involving large

molecules. As a general rule, it is necessary to adjust pore size and porosity to achieve a balance between surface area and high diffusion coefficient inside the pores.

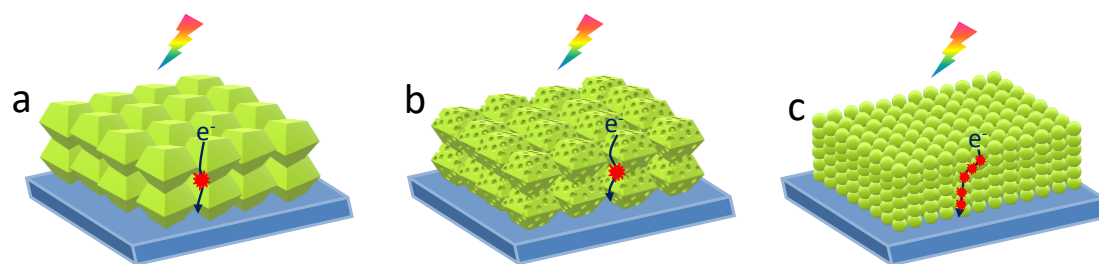
### 2.2.2. Lattice-continuity

The lattice continuity is another characteristic of PSCs. In a PSC, a single lattice domain should run through the whole particle. This implies that there are no grain boundaries in each PSC unit. This feature is extremely important for the performance of semiconductors, where the charge carrier migration through a PSC unit is much faster than through the same volume in aggregates. Generally, the size of a PSC unit is also much larger than that of a small nanocrystal, making PSC materials easier to recycle from aqueous suspension in practical applications. In order to achieve lattice continuity in a relatively large region, the control of the crystallization process is crucial. Usually crystallization of PSCs is a hydrothermal reaction, the resulting solid being submitted to low-temperature aging and high-temperature calcination. Therefore, the control of temperature, reaction time, and capping reagent are among the main parameters to be considered during the synthesis.

It is worth noticing that, similarly to PSCs, nanocrystal arrays exhibit ultrahigh surface areas and large number of active sites. However, they present lack of lattice continuity and the photogenerated charges in nanocrystal arrays must pass through numerous grain boundaries, being most of these charges lost during transport. On the contrary, PSC may drastically shorten the transport path for electrons, which is beneficial in photocatalysis and solar cells applications. As a result of the structural characteristic, PSCs simultaneously possess the merits from the bulk crystals (high crystallinity and large crystal size), and from the nanocrystals (large surface area). These features, together with the above-mentioned tunable pore size and shape have been found very convenient properties for energy conversion and catalysis applications. To further clarify this, the comparison of the basic features of PSCs,



bulk crystals and nanocrystals is illustrated in **Scheme 2** taking photocurrent generation as a typical example.



**Scheme 2.** Illustration of photocurrent generation in one material with three different morphologies: (a) bulk crystals, (b) PSCs and (c) nanocrystals. The dots indicate interparticle migration in the pathway of the electron to the electrode.

Compared to nanocrystals and PSCs, bulk crystals possess too small surface area to provide enough active sites for effective interaction with electrolyte or substrates. Compared to bulk crystals and PSCs, the photoanode made of nanocrystals contain a large number of grain boundaries which will act as recombination centers for photogenerated carriers and greatly reduces the photoelectric conversion efficiency. Due to large size of the crystals and large surface area derived from porosity, PSC-based photoanode has less grain boundaries but still high number of sites, which clearly reduces the energy waste recombination pathways and increases solar energy utilization.

### 2.3. Preparation of PSCs

In the past twenty years, significant progress has been made developing a wide range of methods for the synthesis PSCs with various morphologies, structures and properties.

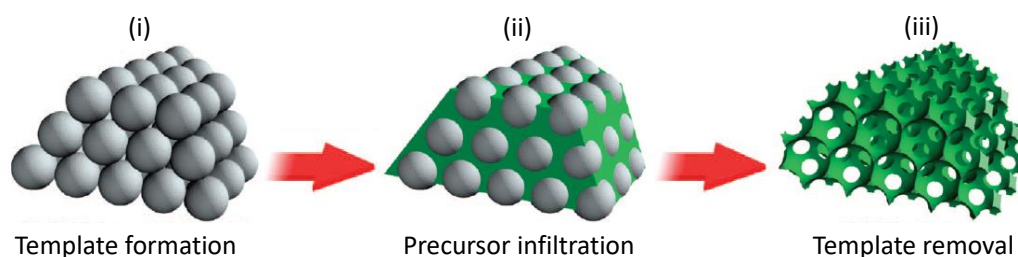
Depending on the criterium employed, several different classifications are possible. In this way, the methods can be grouped according to the reaction type as solvothermal

(hydrothermal),<sup>[2, 9]</sup> sol-gel synthesis,<sup>[10]</sup> chemical vapor deposition (CVD),<sup>[11]</sup> molten-salt

reaction,<sup>[12]</sup> electrochemical<sup>[13]</sup> and ion-exchange methods.<sup>[14]</sup> Moreover, based on the strategy to generate porosity, preparation procedures for PSCs can also be divided into hard-templating,<sup>[2, 5a, 9, 14a, 15]</sup> soft-templating,<sup>[16]</sup> and template-free.<sup>[13, 17]</sup> For the purpose of the present review, PSCs preparation procedures have been classified according to the manner employed to create porosity, so that the amazing range and variety of PSCs can be remarked. It includes (1) inverse replication, (2) decomposition of organic groups, (3) decomposition of inorganic groups, (4) imperfect merging of nanoparticles (NPs), (5) self-etching, (6) ion-exchange induced growth and (7) other preparation methods such as competitive adsorption, CVD epitaxial growth and ion implantation procedure etc. Furthermore, inverse replication can be subdivided into two kinds, “regular procedure” and “irregular” shape depending on the morphology of crystals. Moreover, the methods corresponding to “regular procedure” can be further subdivided into “seeding-based” and “seeding-free”. These subdivisions are closely associated with the occurrence of surface capping and nucleation-growth control of crystals, as it will be discussed in the following section.

### 2.3.1. Inverse replication

Inverse replica, also called hard-templating, is a common strategy to prepare porous materials with precise control of the size, density and morphology of pores. This method relies in the combination of templation by some objects and replication by a precursor of the inorganic semiconductor. However, in the case of PSCs, the single crystal growth is also a prerequisite, which is obviously not necessarily occurring in other common porous materials.<sup>[18]</sup> Usually, most of the inverse duplication procedures consist in three basic steps: (i) template formation, (ii) precursor infiltration, and (iii) template removal and semiconductor formation<sup>[19]</sup> (**Scheme 3**).



**Scheme 3** Schematic illustration of the inverse replica procedure for preparation of PSCs indicating the three steps: (i) template formation, (ii) precursor infiltration and (iii) template removal. Reproduced with permission. <sup>[19]</sup> Copyright (2008) American Chemical Society.

At present, silica spheres,<sup>[2]</sup> poly(styrene-co-methyl methacrylate-co-potassium sulfopropyl methacrylate) (P(St-MMA-SPMAP)) spheres,<sup>[15a]</sup> and the internal pores of zeolites (SBA-15 and KIT-6)<sup>[5a]</sup> have been used as hard templates in synthesis of PSCs. The main prerequisite is the narrow size distribution of the hard template. Of them, silica spheres are the most widely used template due to the well-established Stöber synthesis of uniform silica spheres of various dimensions and its convenient removal by NaOH leaching.<sup>[20]</sup> Silica and organic polymer spheres can both be obtained in a wide range of diameters from a few nanometers to the micrometer scale. The difference between them is the manner in which they are removed and, probably, the mechanism of nucleation-growth of the semiconducting crystals due to their different surface properties. Regarding zeolites as templates, these crystalline aluminosilicates are a large family of porous materials,<sup>[21]</sup> but the pore dimensions in most of them belong to the microporous or small mesoporous range. This limitation in the available pore sizes is a strong drawback for their use as template in inverse replication.

Hydrothermal (or solvothermal) treatments are common procedures widely used in replication synthesis, since the reactive solution phase is well suited to perfectly infiltrate the hard template during the synthesis of PSCs. A precursor solution can be first formed by hydrolysis of appropriate metal salts or by dissolution of soluble inorganic salts, and then used to

infiltrate by capillarity or reduced pressure filling completely the inner space of templates.

Subsequent nucleation and growth by increasing the temperature are usually carried out to form the crystals on the templates.

Due to the wanted requirement of large size particles that should embed as many as possible templates, some special considerations have to be usually taken into account. They include optimization of the reaction conditions and the use of morphology controlling agents.

In the synthesis of PSCs, strong basic and HF solutions are often used to remove silica and zeolite templates. In order to accelerate and complete the etching process, heating, for example, at 80 °C, is usually preferred. Some metal oxides that cannot stand extremely basic or acid environment. In these cases carbon templates can be suitable alternative since these templating spheres can be removed by controlled combustion of the template at temperatures about 500 °C.

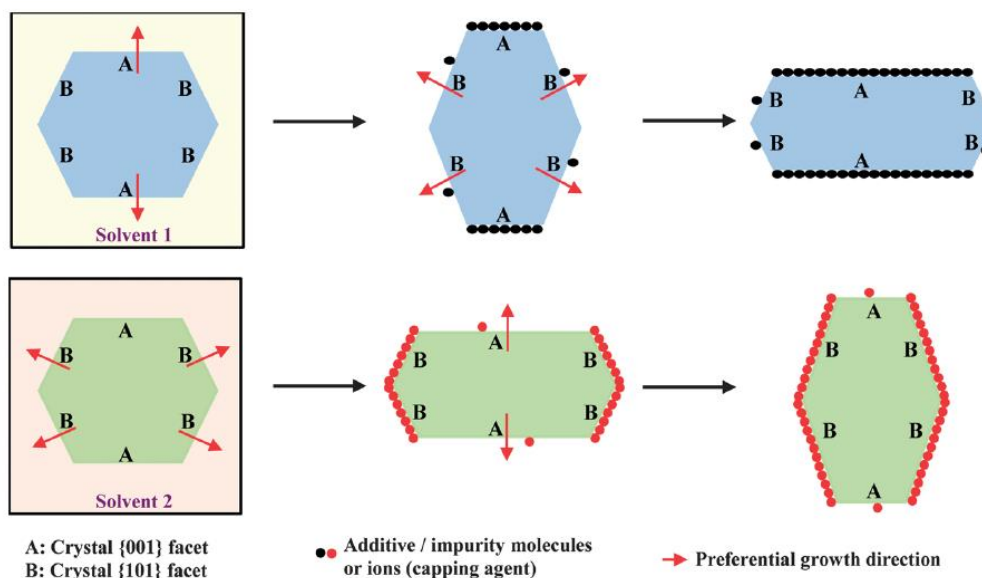
Currently, the PSCs materials that have been reported to be prepared by this method include  $\text{TiO}_2$ ,<sup>[2, 4a, 9b, 15b, 15c, 22]</sup>  $\text{ZnO}$ ,<sup>[15a]</sup>  $\text{BiVO}_4$ ,<sup>[9a]</sup>  $\text{SnO}_2$ ,<sup>[23]</sup>  $\text{CeO}_2$ ,<sup>[4a]</sup> and  $\text{Fe}_2\text{O}_3$ <sup>[24]</sup>, among others. The crystals produced by this procedure can display regular and irregular crystalline shapes, depending on whether or not there is a preferential growth in the crystal of some specific facets. In this regard, to obtain uniform PSCs, a pre-seeding step is sometimes necessary, so that growth of the crystals can occur preferentially on the template surface rather than in the bulk solution. Depending on the type of precursor<sup>[4a]</sup>, the pre-seeding step can be not necessary. In addition, several procedures have been reported for photoelectrode preparation that consists on the direct growth of PSCs film on FTO glass.

### *Regular crystal shape*

The development of the crystal morphology is a complicated process controlled by various chemical, thermodynamic and kinetic factors. Besides Gibbs free energies (surface energies)

of facets, time, temperature and solute distribution also play important roles in the formation of a preferential crystal shape. In general, when surface facet energies dominate the morphology of the particle, the facets with high energies grow quickly and the facets with low energies are comparatively less developed.<sup>[25]</sup> However, if the facets with high energies adsorb some appropriate molecules or ions, its surface energy can be greatly reduced and other facets may have a favorable growth under these conditions, growing with even better quality than that of original low-energy facets. Consequently, crystals with unusually clear facets could be obtained. This strategy based on the use of adsorbates can be used to prepare single crystals with controllable proportion of different facets.

One illustrative example of this strategy is anatase TiO<sub>2</sub>. Thus, using common wet-chemical methods it has been difficult to obtain regular crystals.<sup>[26]</sup> However, the {001} facets of anatase with high energy can be stabilized by preferential adsorption of capping agents, and single crystals with adjustable ratio between {001} and {101} facets can be in this way conveniently prepared, as illustrated in **Scheme 4**.<sup>[27]</sup> In this way, Yang et al<sup>[28]</sup> first achieved in 2008, well-shaped single crystals of anatase TiO<sub>2</sub> of micrometer size, by a hydrothermal reaction of titanium tetrafluoride (TiF<sub>4</sub>) as titanium source and hydrogen fluoride as capping agent. The obtained crystals showed well-defined morphology of truncated bipyramid with two square {001} surfaces and eight isosceles trapezoidal {101} surfaces, with a relative area percentage of {001} and {101} facets of 47 and 53 %, respectively. Almost all the subsequent syntheses of TiO<sub>2</sub> PSCs are based on this achievement.<sup>[2]</sup> The case of anatase TiO<sub>2</sub> with preferential facet growth is one example showing that the preparation of regular PSCs greatly depends on the development of synthetic technologies for single crystals.



**Scheme 4.** Effect of surface capping agent on the morphological control the {001} and {101} facets in TiO<sub>2</sub> crystals. Reproduced with permission.<sup>[27]</sup> Copyright 2014. Royal Society of Chemistry.

#### *With pre-seeding treatment*

Pre-seeding is an effective strategy to take advantage of the energy barrier associated with homogeneous nucleation in bulk solution to limit the growth of the crystals to the surface of the templating agent. Seeding the template with submicroscopic seeds can lead to heterogeneous nucleation, favoring the growth of the vast majority of crystals on the hard template rather than in the bulk solution.

Anatase TiO<sub>2</sub> PSCs with perfect external shape were first obtained by Snaith et al<sup>[2]</sup> using silica spheres as a hard template and a hydrothermal reaction similar to that developed by Yang. Silica spheres were pre-seeded by immersion in a diluted TiCl<sub>4</sub> solution and TiF<sub>4</sub> was used as titanium source. In the formation of anatase PSCs, one key point is that seed growth of TiO<sub>2</sub> crystals is insensitive to the silica template. It appears that the growth of TiO<sub>2</sub> crystals depends mainly on the external conditions such as reaction solution media, seed concentration and temperature, without interference of the silica template in the crystallization process. In

this case,  $\text{TiO}_2$  crystals grow wrapping the template spheres. Another feature in this synthesis is the quasi close-packed array formed by the silica spheres that is crucial to achieve simultaneously porosity and single crystallinity. Close packing of silica spheres contacting each other assists the generation of coherent holes inside the crystals by inverse replica. Subsequent etching of the silica spheres by NaOH solution renders the  $\text{TiO}_2$  PSC<sup>[15b]</sup> (**Figure 1**).

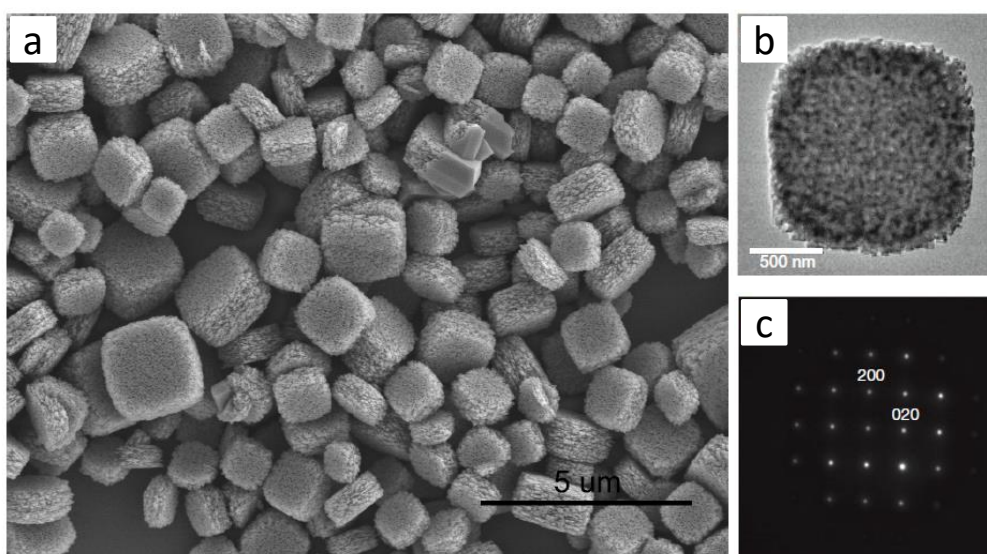


**Figure 1.** (a) SEM image of  $\text{TiO}_2$  PSCs prepared by 50 nm silica bead templation (seeding with 0.015 mM  $\text{TiCl}_4$ ); and (b) TEM and (c) SAED pattern of a  $\text{TiO}_2$  PSC synthesized using 40 mM  $\text{TiF}_4$ . Reproduced with permission.<sup>[2]</sup> Copyright (2013) Springer Nature.

Different Ti sources employed in the seeding-template strategy to fabricate anatase  $\text{TiO}_2$  PSCs are those that have been extensively used for the synthesis of anatase single crystals with exposed  $\{001\}$  facets.<sup>[3, 27]</sup> Besides  $\text{TiF}_4$ ,<sup>[2, 15b, 15c]</sup> tetrabutyl orthotitanate (TBOT) is another Ti source that has been widely used in PSC synthesis.<sup>[22]</sup> Zheng et al. have reported that pre-seeding is necessary when using silica template and TBOT as the Ti precursor. Otherwise the amount of PSCs obtained is very little because the hydrophobic alkyl groups of TBOT have a poor affinity for the silica template, retarding the formation of  $\text{TiO}_2$  PSCs.<sup>[4a]</sup>

Rutile  $\text{TiO}_2$  PSCs with well-defined facets have also been prepared by the seeding-template strategy. With TBOT as Ti source, the evolution as a function of the external conditions of the morphology and size of rutile and anatase  $\text{TiO}_2$  PSCs has been systematically investigated by Zheng.<sup>[22a]</sup> Generally, a low HF concentration in concentrated HCl facilitates the formation of the rutile phase (**Figure 2**). An increase of the seed density on the template or the raise of the reaction temperature decrease generally the size of PSCs. It was again observed that the presence of the silica template does not interfere on the crystallization and only serves for directing the reverse replication. Moreover, by tuning the amount of NaF in the HCl solution  $\text{TiCl}_4$  can also be employed to synthesize rutile PSCs with different  $\{111\}/\{110\}$  facet ratios.<sup>[4b, 29]</sup> The percentage of  $\{111\}$  facets increased with the amount of NaF and eventually the whole rutile  $\text{TiO}_2$  PSCs exposed exclusively the reactive  $\{111\}$  facet.

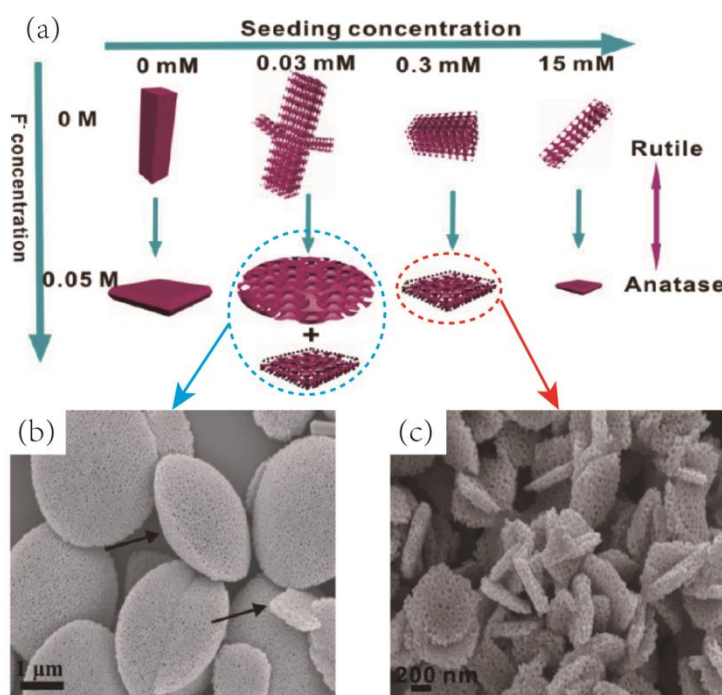
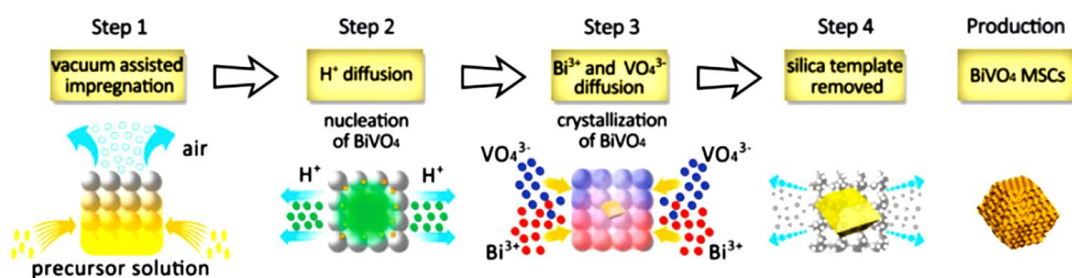


**Figure 2.** (a) Schematic evolution of morphology and size for of  $\text{TiO}_2$  PSCs at different HF concentrations and with different seeding concentrations; SEM images of (b) the PSC mixture of olive-shaped and nanosheet anatase (seeding concentration: 0.03 mM, HF: 0.05 M), and (c) anatase nanosheet PSCs (seeding concentration: 0.3 mM, HF: 0.05 M). Reproduced with permission.<sup>[22a]</sup> Copyright (2013) American Chemical Society.



Apart from  $\text{TiO}_2$ ,  $\text{BiVO}_4$  is another inorganic semiconductor that can be obtained as PSCs through the hard template strategy and hydrothermal synthesis<sup>[9a]</sup>. The most obvious difference between  $\text{BiVO}_4$  PSC and the synthesis of oxide PSCs is the “pre-seeding” step. At this step, the voids among silica template were filled with the  $\text{BiVO}_4$  precursor solution.<sup>[2]</sup> In the subsequent hydrothermal step, the impregnated silica template was suspended into a solution of amorphous  $\text{BiVO}_4$ . Due to equilibrium between redissolution of amorphous  $\text{BiVO}_4$  in the bulk solution and double-ion diffusion, the nucleation and growth can be deferred and the slow crystallization facilitates the formation of a PSC structure (**Scheme 5**).

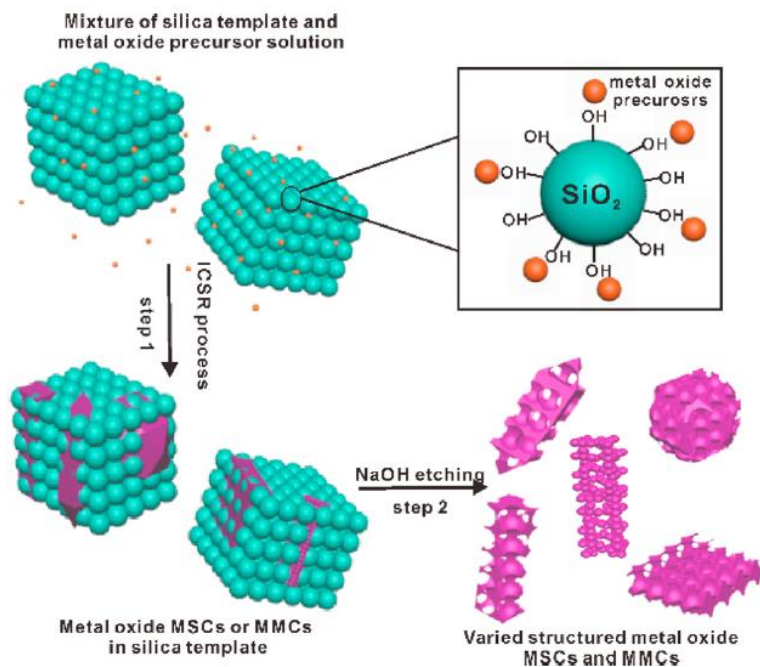


**Scheme 5.** Illustration of the formation mechanism of  $\text{BiVO}_4$  PSCs. Reproduced with permission.<sup>[9a]</sup> Copyright (2016) Royal Society of Chemistry.

#### *Without pre-seeding treatment*

From thermodynamic considerations, template pre-seeding favors heterogeneous nucleation and confined growth of the crystals inside the template voids rather than in the bulk solution. In this way, a near quantitative yield of PSCs based on the precursor can be obtained.<sup>[2]</sup> However, it has been found that some metal oxide PSCs could still be obtained in high yields without seeding treatment, by adequate selection of the precursor.<sup>[4a]</sup> The reason why in certain cases pre-seeding is not necessary is the presence of silanol ( $\text{Si-OH}$ ) groups on the dense silica surface. Silanol groups are hydrophilic and can adsorb the precursors. In these

cases, the bare silica plays the same role as the seeded silica, providing sites for heterogeneous nucleation, interacting with the growing crystals through interfacial forces, and preventing them from aggregation (**Scheme 6**).



**Scheme 6.** Fabrication process of metal oxide MSCs and mesocrystals (MMCs) with various morphologies. Step 1: metal oxide nucleates at the surface of silica sphere template, crystallizing around where the local concentration of precursor is high. Step 2: the MSCs or MMCs are obtained by removal of the silica template by NaOH etching. Reproduced with permission.<sup>[4a]</sup> Copyright (2014) American Chemical Society.

In the synthesis of TiO<sub>2</sub> PSCs, when selecting hydrophilic TiCl<sub>4</sub> as precursor, high yield and high quality rutile and anatase TiO<sub>2</sub> MSCs can be directly obtained without pre-seeding treatment. However, when using TBOT with the hydrophobic alkyl groups as precursor, little TiO<sub>2</sub> MSCs would be obtained without pre-seeding, due to the poor affinity of TBOT for the silica template. By increasing the HF concentration, the change of phase from rutile to anatase can be achieved, accompanied by the change in morphology from porous nanorod to porous cuboid.<sup>[4a]</sup>

Besides  $\text{TiCl}_4$ , other inorganic titanium salts have also been utilized to produce  $\text{TiO}_2$  PSCs. Using  $\text{TiB}_2$  as titanium precursor, rutile  $\text{TiO}_2$  PSCs were obtained by hydrothermal reaction in the presence of  $\text{HCl}$  and  $\text{NH}_4\text{F}$ .<sup>[4c]</sup>  $(\text{NH}_4)_2\text{TiF}_6$  has also been employed to fabricate anatase  $\text{TiO}_2$  PSCs.<sup>[9b]</sup> In the last case, only  $(\text{NH}_4)_2\text{TiF}_6$ , silica template and water were used, making the whole procedure quite facile. The obtained material exhibits the morphology of microspheres composed of PSCs with exposed  $\{001\}$  facets. These successful cases further confirm the importance of choosing the appropriate precursor, avoiding the seeding treatment and simplifying the fabrication process.

Based on the above knowledge that the properties of the precursor should match the hydrophilicity of the silica surface, it is also possible to synthesize other metal oxide PSCs with tailored structures by the non-seeded silica templated strategy. In this procedure,  $\text{HCl}$  and ethanol are usually introduced to the solution to achieve an adequate control of the metal oxide precursor hydrolysis rate.<sup>[4a]</sup> In addition, polyvinylpyrrolidone (PVP) has also been reported as additive to control the crystal shape and preferential facet formation, for example, in the case of  $\text{SnO}_2$  PSCs.<sup>[4a, 23]</sup> Because of the slow hydrolysis rates of Ce and Fe cations, aqueous solutions of  $\text{NaF}$  as morphology control agent can lead to the growth of  $\text{CeO}_2$ <sup>[4a]</sup> and  $\text{Fe}_2\text{O}_3$ <sup>[24]</sup> as PSCs.

#### *In-site formed PSCs-films on substrates*

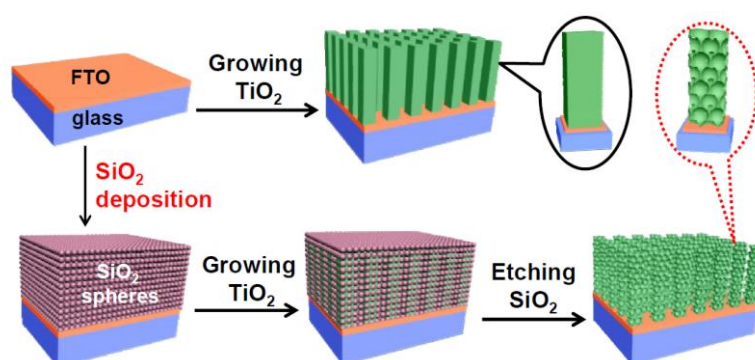
The structural coherence present in PSCs determines a good long-range charge mobility through the crystals. This property makes PSCs highly suitable for directional charge transport from PSCs to conductive substrates, or vice versa. Consequently, several studies have reported the growth of PSCs-films on conductive substrates. Compared to the direct casting of preformed PSC powders on substrate by spin-coating<sup>[2]</sup> or doctor blading,<sup>[15c]</sup> in-

in-situ formation of PSC films on substrates results in films that exhibit a better structural coherence and an enhanced connectivity at the semiconductor/substrate interface.<sup>[30]</sup>

Generally, films of performed PSCs are composed of several layers of disordered particles. In order to improve the adherence between film and substrate and other properties, a compact seed layer using a  $\text{TiO}_2$  sol is first coated on the FTO substrate, then the silica template without seeding can be screen-printed using a silica paste. After the hydrothermal growth in a Ti precursor solution, the silica template can be selectively etched. This procedure results in an anatase  $\text{TiO}_2$  PSC-film with a seeded layer on substrate.<sup>[30]</sup>

Another type of in-situ PSC film is composed by ordered PSC arrays, that is, the film of one-dimensional (1-D) porous rods or tubes, which can achieve the vectorial charge transport from the outer surface of the film to the substrate without extra boundaries. The close packed silica template on FTO substrate is formed in these cases by centrifugation of the vessel filled with the precursor solution including dispersed silica spheres with the FTO glass being placed at the bottom of vessel. In a subsequent hydrothermal reaction, the  $\langle 001 \rangle$  oriented rutile  $\text{TiO}_2$  rods can grow on a special FTO substrate with  $\langle 002 \rangle$  preferential facet orientation of the F-doped  $\text{SnO}_2$  film as a seed layer due to the coincident crystal structures and similar lattice parameters of rutile  $\text{TiO}_2$  and  $\text{SnO}_2$ . Selective template etching from the obtained  $\text{SiO}_2$ - $\text{TiO}_2$  composite film leads finally to the formation of the rutile  $\text{TiO}_2$  PSC array film on FTO

(Scheme 7).<sup>[31]</sup>



**Scheme 7.** Schematic illustration of the synthesis procedures of films of non-PSC rod arrays (top panel) and PSC rod arrays (bottom panel) of rutile TiO<sub>2</sub> on FTO glass substrates.

Reproduced with permission.<sup>[31]</sup> Copyright (2015) Elsevier.

### *Irregular crystal shape*

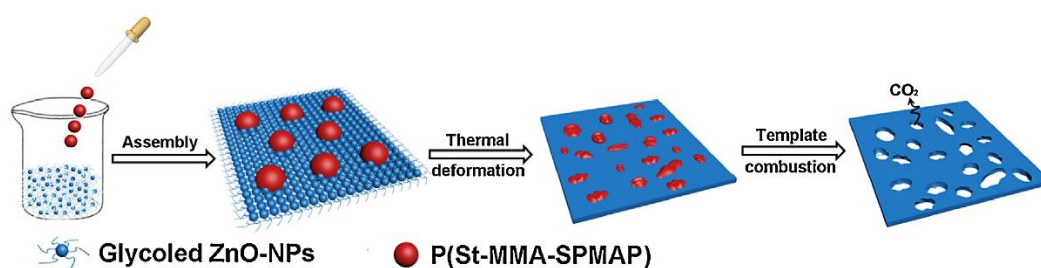
The crystal shape evolution is greatly driven by the growth rates of different facets. These rates can be manipulated by selection of capping agents to adjust surface energies. In the absence of appropriate capping agents in the reaction system, PSCs with irregular shape are generally formed. In addition, low reaction temperatures or short reaction times can also cause incomplete development of the crystal shape in hydrothermal or solvothermal synthesis. In the literature, the number of studies describing irregular PSCs by hard templating strategy is rather small compared to regular PSCs.

Anatase TiO<sub>2</sub> PSCs with 2D and 3D ordered mesoporous structure have been prepared by confining the crystal growth within the mesopores of SBA-15 and KIT-6 silica, respectively, via a solvothermal reaction with TiOSO<sub>4</sub> as precursor.<sup>[5a, 32]</sup> In these syntheses, the growth of anatase PSCs involves basically three important steps.<sup>[5a]</sup> The first step is the formation of NPs in solution. The second one is the assembly of the previously formed NPs. The last step is the fusion and crystallization of the NP aggregates. In the synthesis, the templates act as structure directing agent, obtaining finally an ordered porous structure. The unique crystal shape can be attributed to thermodynamic driving forces minimizing surface energy by adopting a spherical shape.

With SBA-15 as template, rutile PSCs have also been prepared using freshly synthesized titanium nitrate as precursor which was prepared by dissolving the hydrolyzed precipitate of titanium tetra-isopropoxide (TTIP) or TBOT in nitric acid<sup>[33]</sup> In the process, the long Ti-O-Ti

chains in titanium oxynitrate from hydrolysate of titanium nitrate are believed to be the key intermediates for the formation of large  $\text{TiO}_2$  crystals inside the SBA-15 pores.

ZnO PSC in the shape of nanosheets have been prepared by a novel filtration-assembling approach using the P(St-MMA-SPMAP) bead of as hard template.<sup>[15a]</sup> Ethylene glycol (EG)-capped ZnO NPs were first synthesized through solvothermal reaction in viscous EG solution of  $\text{Zn}(\text{AcO})_2 \cdot 2\text{H}_2\text{O}$  as source. Then, P(St-MMA-SPMAP) colloids were added to form a ZnO/colloid suspension. The suspension was slowly filtered to allow the formation of ZnO/colloidal composites by self-assembling. During the combustion step, the polymer colloids tend to soften and deform in small fragments. After the total combustion of the small fragments, ZnO PSC nanosheets with irregular shapes with exposed  $\{0001\}$  polar facets are obtained (**Scheme 8**). In such synthesis, the infiltration rate is an important factor to control the formation of 2D PSC nanosheets, otherwise, a hierarchically macro-mesoporous ZnO/colloid structure is obtained. EG capping of ZnO is also very important improving the interaction between ZnO NPs and colloidal spheres, and assisting the formation of continuous nanosheets during the calcination process. An evidence in support of the previous claims is that in the absence of polymer colloids only  $\sim 30$  nm irregular ZnO NPs are obtained.



**Scheme 8.** Schematic illustration of the synthetic procedure of ZnO PSC nanosheets by means of poly(St-MMA-SPMAP) beads as template. Reproduced with permission.<sup>[15a]</sup> Copyright (2016) Elsevier.

### 2.3.2. Decomposition of organic groups

Organic additives are often used to assist the generation of pores. In the material formation process, organic molecules or their self assemblies occupy some space at determined positions. In the subsequent high-temperature crystallization process, these organics are decomposed in water, CO<sub>2</sub>, ammonia and other gases. Consequently, pores in the crystals are created where these organics were located. The origin of this porosity is the formation of thermodynamically stable aggregates of nanoscale dimensions from the organic additives.<sup>[16e]</sup> Different additives can exhibit different mechanisms leading to the synthesis of nanostructures. There are mainly two classes of organic additives employed in the synthesis of PSCs. The first one is surfactants which act as structure directing agents that self-assemble to produce some specific form of microparticles, for example micelles. Micellization takes place beyond critical micellar concentration (CMC) and is generally driven by minimization of the interfacial energy between the hydrocarbon chains and water.<sup>[18]</sup> The precursor bound on the micelle surface would further aggregate to reduce surface energy. Consequently, the surfactants are incorporated in the precursor. The second type of organic additives are molecules that can form metal-organic networks by metal-ligand coordination bonds, for example carboxylates, polyethylene glycol, cellulose, etc. During the reaction, the pore structure is originated by the coordination geometry of organic molecules with metals. In addition, there are some organic molecules which can influence also the morphology of the growing particles acting as capping agents controlling the growth rate of different crystal facets. Overall, it is because of self-aggregation and interaction forces why organic additives favor simultaneous the appearance of single crystal domains and porosity upon crystallization and subsequent removal of organics.

Until now, many metal oxides have been prepared by this strategy, for example (Nb,Ta)<sub>2</sub>O<sub>5</sub>, BiVO<sub>4</sub>, WO<sub>3</sub>, Bi<sub>2</sub>O<sub>3</sub>, β-Ga<sub>2</sub>O<sub>3</sub>, ZnO, Fe<sub>2</sub>O<sub>3</sub>, TiO<sub>2</sub>, among others. Of them, ZnO and WO<sub>3</sub> have also been deposited as thin films on different substrates to achieve additional properties.

*Surfactant templation*

Amphiphilic block copolymers have been widely used as soft templates in preparing porous materials.<sup>[34]</sup> Poly(ethylene oxide)-*b*-poly(propylene oxide)-*b*-poly(ethylene oxide) (PEO-PPO-PEO) is a commercially available type of triblock copolymer. Examples of these triblock copolymers are Pluronic P123 (EO20-PO20-EO20) and Pluronic F127 (EO106-PO70-EO106). As already commented, the first example of mesoporous single crystals, (Nb, Ta)<sub>2</sub>O<sub>5</sub> was prepared by Kondo et al. in 2002 using P123 as soft template through an aging-calcination procedure<sup>[16a]</sup>. After mixing the same amount of Nb and Ta chlorides in ethanol with P123, the colloidal suspension was aged for about one week. Then, the obtained amorphous precursor was calcined at 673 K to crystallize and remove the surfactant. In this way, a wormhole-like structure with the pore size distribution centered at ca. 10 nm was obtained. (**Figure 3**).

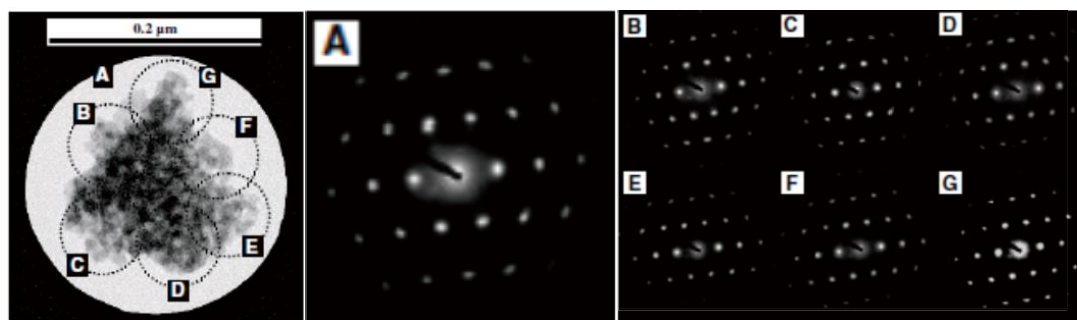


**Figure 3.** TEM image of a PSC, and SAED patterns of the whole (A) and six different parts (B–G) marked by dotted circles in TEM image. Reproduced with permission.<sup>[16a]</sup> Copyright (2002) Springer Nature.

Monoclinic BiVO<sub>4</sub> single crystals with a porous spherical or porous octapod-like morphology have also been prepared via a hydrothermal reaction assisted by P123.<sup>[16b]</sup> The mechanism of this synthesis is suggested to start with surfactant molecules adsorbed on the surface of BiVO<sub>4</sub>



nuclei, decreasing the surface energy of the nanocrystals. Then, P123-adsorbed NPs undergo aggregation and self-assembly depending on the solution pH and reaction temperature. The growth rate of the adsorbed crystal faces was reduced by the adsorbed P123 as capping agent, inducing a compression along the axis perpendicular to these facets. Consequently, two-dimensional (2D) nanosheets or thin plate-like entities are formed. Through the simultaneous collective self-assembly of 2D nano entities after the Ostwald ripening process and subsequent calcination,  $\text{BiVO}_4$  PSCs with a variety of different morphologies are finally obtained under different hydrothermal conditions.

Using Pluronic F127 as directing agent,  $\text{TiO}_2$  PSCs were obtained by Liu et al. Olive-shaped precursor mesocrystals (FDU-19) were initially obtained by an evaporation-driven oriented assembly approach in a solution containing tetrahydrofuran (THF), F127,  $\text{H}_2\text{O}$ , HCl, acetic acid (HOAc) and TBOT followed by calcination under  $\text{N}_2$ . After heating at air, the olive-shaped mesoporous  $\text{TiO}_2$  single crystals (SC-FDU-19) are obtained.<sup>[16c, 16d]</sup> The oriented growth of the FDU-19  $\text{TiO}_2$  mesocrystals is driven by two solvents with different boiling-point (THF and water). In the first stage, spherical Pluronic F127/titania micelles are formed at the interface between the THF and water-rich phases. With a continuous solvent evaporation, these small micelles undergo an increasing anisotropic aggregation due to the different boiling points of THF and water. The preferential evaporation of THF results in olive-shaped micelle aggregates. Finally, an evaporation of residual THF and water from the center to outside of the particles causes the fusion of the micelles into cylindrical channel-like micelles. Subsequently, cross-linked  $\text{TiO}_2$  oligomers are formed around Pluronic F127 cylindrical micelles, resulting into flake-like nano crystalline particles. Calcination under  $\text{N}_2$  removes the template and  $\text{H}_2\text{O}$ , originating the olive-shaped morphology with a large porosity (**Figure 4**). Upon further annealing in air, increasing fusion of the adjacent nanocrystal blocks occurs by condensation of surface  $-\text{OH}$  groups. During this process, surface energy diminishes, healing the crystal defects and producing fusion of the nanoplatelets along the

[001] direction, resulting in the mesoporous single-crystals FDU-19 (SC-FDU-19). In the process, the olive-like morphology is preserved, and the mesopores in FUD-19 are converted to 3D open spherical mesopores throughout the whole particle.

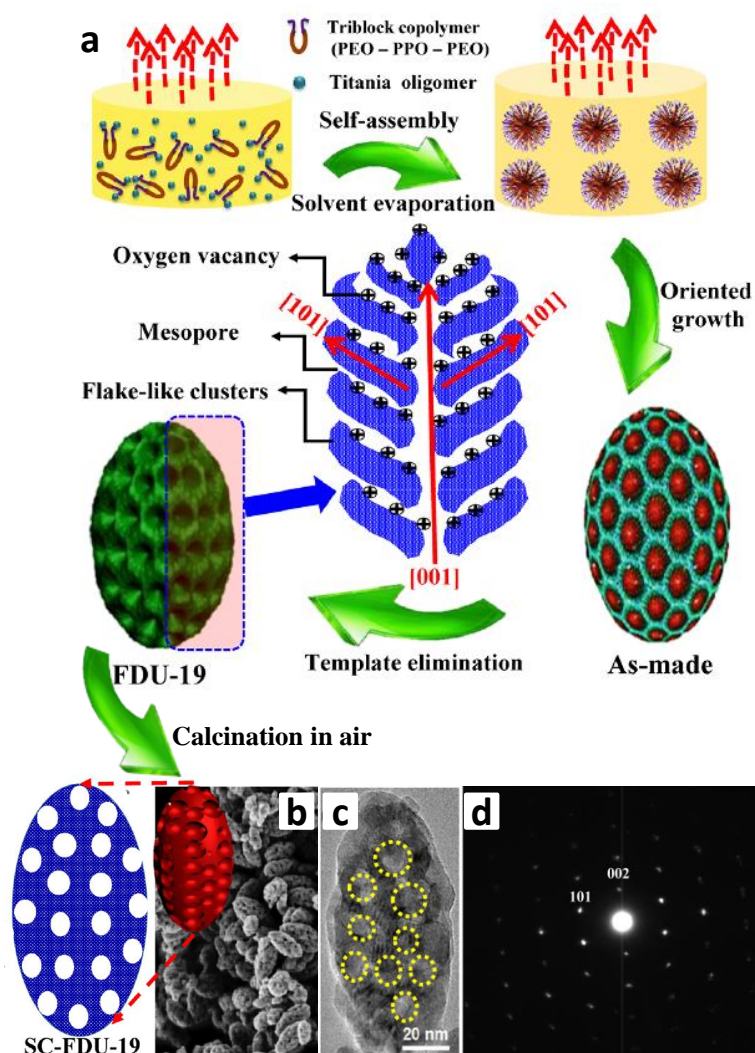


**Figure 4.** (a) Schematic illustration of the formation of olive-like mesoporous  $\text{TiO}_2$  single crystals (SC-FDU-19) through the evaporation-driven oriented assembly process. b, c and d are SEM, TEM and SAED pattern, respectively. Reproduced with permission.<sup>[35]</sup> Copyright (2015) American Chemical Society.

With additional assistance of 3D ordered macroporous carbon (3DOMC), Liu et al. further prepared a more complicated 3D ordered mesoporous  $\text{TiO}_2$  superstructure (Level-1).<sup>[36]</sup> These

superstructures consist of a spherical core and 12 symmetric satellite hemispheres epitaxially growing out of the core vertices. In the mesoporous structures, each individual hemispherical satellite is confirmed to be single crystal. A more complex and asymmetric  $\text{TiO}_2$  superstructure (Level-2) with 13 spherical cores and up to 44 symmetric satellite hemispheres could be also obtained by increasing the content of impregnated  $\text{TiO}_2$  emulsion droplets (Figure 5).

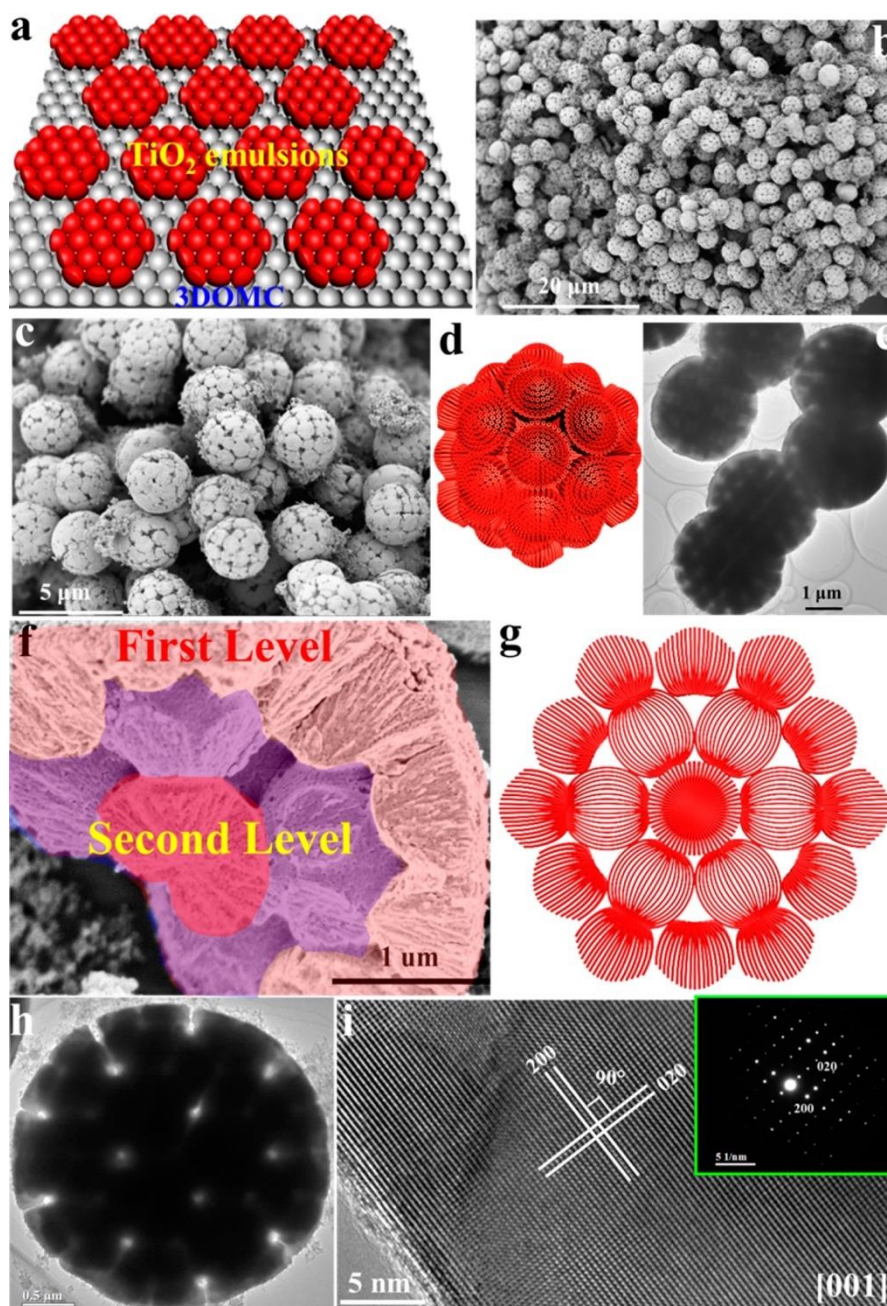


**Figure 5.** (a) Schematic representation of the nucleation and growth of the Level 2 3D  $\text{TiO}_2$  microemulsions within 3D ordered 3DOMC scaffolds. (b,c,f) Level 2  $\text{TiO}_2$  superstructure

SEM images. (d) Model structure of a Level 2 mesoporous TiO<sub>2</sub> superstructure, showing 13 spherical cores and 44 satellite hemispheres. (e,h) Level 2 mesoporous TiO<sub>2</sub> superstructure TEM images. (g) The corresponding interior mesopore model. (i) HRTEM image taken from the area of the cylindrical mesopore bundles of an ultramicrotomed Level-2 mesoporous TiO<sub>2</sub> superstructure with [001] incidence. Inset of panel I is the corresponding SAED pattern. Reproduced with permission.<sup>[35]</sup> Copyright (2017) American Chemical Society.

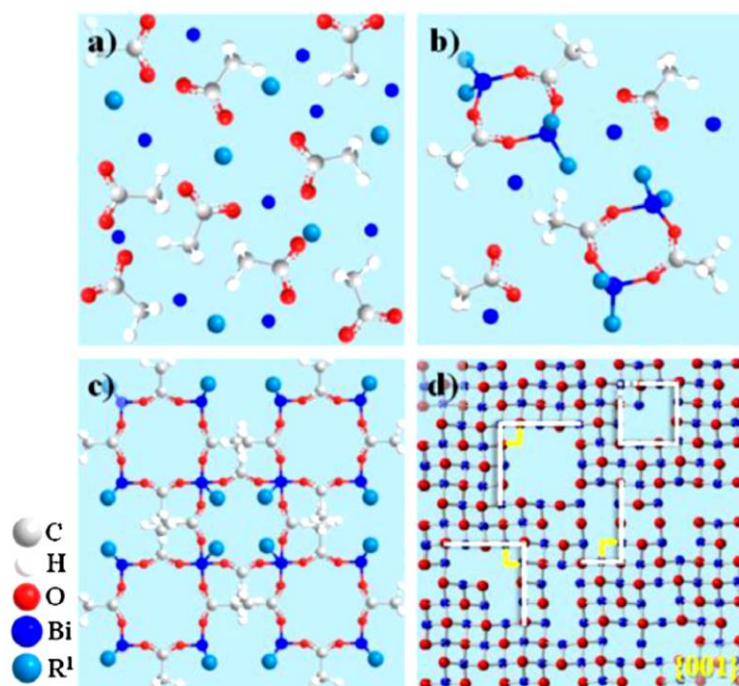
In addition, cetyltrimethylammonium bromide (CTAB) has also been used for the synthesis of PSC inorganic semiconductors, for example  $\beta$ -Ga<sub>2</sub>O<sub>3</sub> PSC blocks.<sup>[16e]</sup> Under hydrothermal treatment, CTAB (CTA<sup>+</sup>, Br<sup>-</sup>) primarily acts as structure directing agent to generate a monolayer which would gradually change into micelles. Ion pairs between inorganic species and surfactant could be formed by electrostatic interaction. The system adopts a block-like micelle structure with minimum energy configuration. Finally, porous nanoblocks are formed after thermal treatment.

#### *Dynamic, soft supermolecular aggregates*

Organic molecules can bind to metal ions or particles in various ways, such as poly-coordinative metal-ligand interaction, electrostatic forces, hydrogen bonds or van der Waals (VDW) interactions. This may result in the formation of a non-rigid network in the liquid phase. In some cases, organic ligands directly connect metal ions or particles to form metal-organic-metal networks. In other cases, the organic molecules (e.g. single coordinative organic ligands) first connect with metal ions or they modify particles. Then the resulting metal ion-ligand or particle-ligand self-assemble by intermolecular forces, to form metal-organic-organic-metal network. The resulting dynamic soft species largely depends on

molecular structure of the organic molecule and the reaction conditions (e.g. pH values, solvent ratio, temperature, etc.).

Acetic acid can be used to form this type of supermolecular structure with metal ions. In the formation of  $\text{Bi}_2\text{O}_3$  PSC nanosheets with exposed {001} facets and regular square holes,<sup>[16f]</sup> two  $\text{Bi}^{3+}$  ions first combine two acetic acid molecules generating a complex. The alcohol molecules are electrostatically adsorbed on these complexes, preventing their longitudinal growth. Subsequently, the formed complex-alcohol aggregate adds more acetic acid molecules forming larger and sheet-like entities, where every  $\text{Bi}^{3+}$  connects with four separate acetic acid molecules forming a 2D network. In the final  $\text{Bi}_2\text{O}_3$  precursor, a considerable density of defects are left due to the soft and dynamic nature of the supermolecular precursor and the presence of organics that will be removed in the calcination step, leading to the generation of square holes with various sizes in the  $\text{Bi}_2\text{O}_3$  sheets (**Scheme 9**). The existence of three coordination modes between acetic acid and  $\text{Bi}^{3+}$  ions in the hydrothermal reaction, namely, unidentate, bidentate and bridging forms has been proposed, and their relative proportion depends on the amount of ethanol. With only a little amount of ethanol, a bidentate mode is preferentially formed; with larger amount of ethanol, a bridging mode would be the prevalent species resulting in relative slower reaction rate and bigger sheets.



**Scheme 9.** Proposed mechanisms leading to the formation of  $\text{Bi}_2\text{O}_3$  PSC nanosheets with quadrature holes and exposed  $\{001\}$  facets. Reproduced with permission.<sup>[16f]</sup> Copyright (2013) Elsevier.

It has also been proposed that esters formed in situ from acetic acid and alcohols which can modify and connect particles by intermolecular interaction. With this method, anatase  $\text{TiO}_2$  PSCs with special polyhedral pores have been prepared via a hydrothermal reaction, followed by calcination at  $500\text{ }^\circ\text{C}$ .<sup>[37]</sup> In the hydrothermal reaction, chain bundles were first generated through the acidolysis of TBOT catalyzed by acetic acid. These nascent nanochains, surrounded by hydrophobic groups, were then drawn together by interaction with esters formed in the system and assembled into regular repeating structures. Finally, calcination at high temperature leads to the formation of MSCs. According to this proposal, the esters behave as a *de facto* template during the formation of  $\text{TiO}_2$  PSCs.

Besides acetic acid, oxalic acid was also employed to provide bridging coordination and, then, direct the morphology of precursors. Using a strategy of morphology-conserved transformation,  $\text{WO}_3$  flowers with PSC sheets were synthesized.<sup>[16g]</sup> In the solvothermal

reaction, oxalate ions could interlink with W=O or W-OH<sub>2</sub> species, being responsible for the formation of a plate-like structures in the precursor. Then, these plates continue to grow eventually generating the flower-like aggregates. WO<sub>3</sub> flowers with PSC sheets were formed by a final thermal pyrolysis treatment. In addition, WO<sub>3</sub> PSC nanoflakes were also fabricated on FTO substrate by solvothermal method.<sup>[38]</sup>

Using urea to promote supermolecular aggregation, Bi<sub>3</sub>NbO<sub>7</sub> single crystal nanosheets were fabricated through a solvothermal method.<sup>[39]</sup> The phase and morphology could be manipulated by varying both the urea content and pH value. Under appropriate conditions, Bi<sub>3</sub>NbO<sub>7</sub> nanosheets with square pores can be formed. In the reaction, the metallic ions not only connected with HO<sup>-</sup>, but also coordinate with O and N atoms of urea. Subsequently, upon rising reaction temperature and prolonging the reaction time causes urea decomposition generating defects and resulting in the formation of porous nanosheets.

Ionic liquids could produce extended hydrogen-bond systems in the liquid state. Hematite PSC nanorods have been synthesized by a hydrothermal process and subsequent heat treatment in air with assistance of 1-n-butyl-3-methylimidazolium chloride ([BMIM][Cl]).<sup>[16h]</sup> In the liquid phase, [BMIM][Cl] acts as a soft template and a capping agent facilitating the formation of nanorods, due to its ability to undergo poly-coordination. The imidazolium cations of ionic liquids could be adsorbed on O-terminated surface by electrostatic force and by hydrogen bond between the hydrogen atom at the C2 position of the imidazole ring and the oxygen atoms of O-Fe. In this way, the O-terminated plane of the nascent metal oxide nuclei will strongly adsorb [BMIM]<sup>+</sup> cations. By additional  $\pi$ - $\pi$  interactions between the imidazolium rings, the [BMIM]<sup>+</sup> cations will be aligned facilitating organization of these cations respect to the material surface, thus, leading to defined morphology of the NPs. The pores are formed by removal of the ionic liquid and of the generated H<sub>2</sub>O in  $\alpha$ -FeOOH nanorods (**Figure 6**).

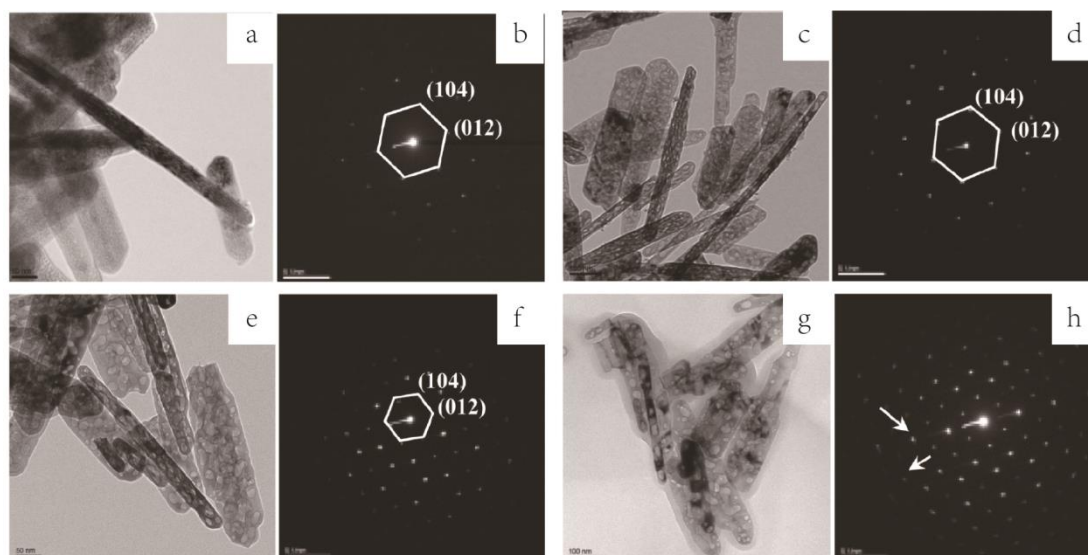
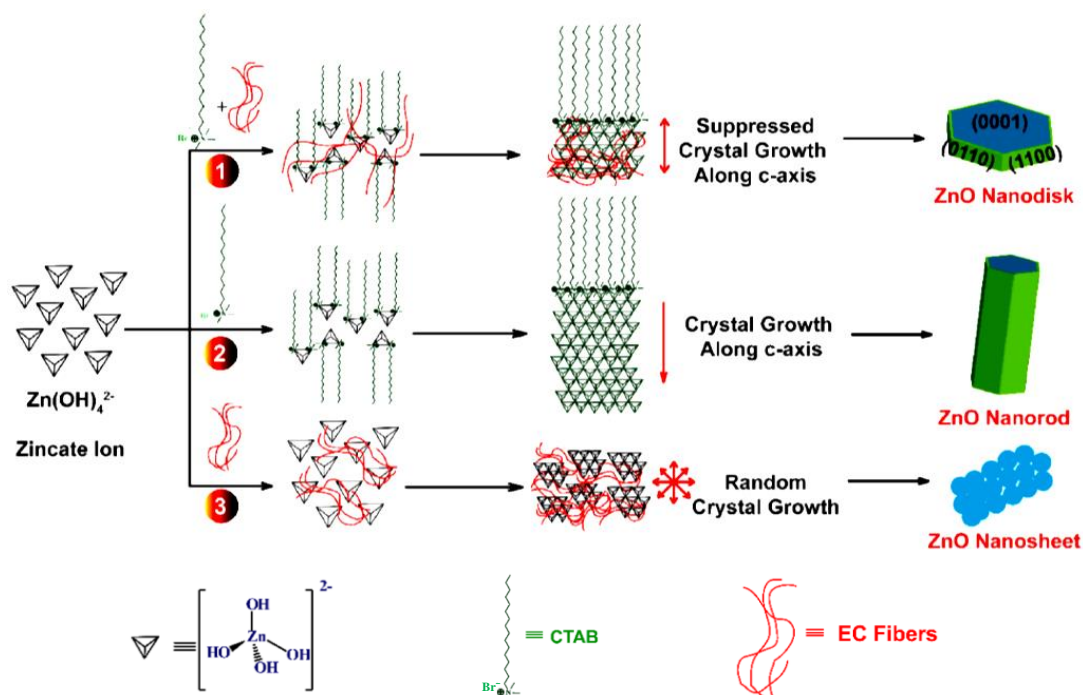


**Figure 6.** TEM images and SAED patterns of the hematite PSC nanorods with different pore size prepared by heat treatment of  $\alpha$ -FeOOH nanorods at 523 (a and b), 623 (c and d), 673 (e and f), and 723 K (g and h) for 3 h in air.  $\alpha$ -FeOOH was prepared by a hydrothermal process with assistance of ionic liquid. Reproduced with permission.<sup>[16h]</sup> Copyright (2011) American Chemical Society.

Polyethylene glycol (PEG) can chelate metal ions in solutions. Spindle-shaped anatase  $\text{TiO}_2$  PSCs have been obtained by hydrothermal synthesis and subsequent annealing using PEG-400 as soft template.<sup>[40]</sup> At the beginning, a titanium precursor would form by chelation of PEG-400 to titanium centers. The controlled hydrolysis-condensation of the chelated titanium precursor in the presence of water leads to the formation of Ti-O-Ti bonds, producing a large number of anatase nanocrystals. These nascent anatase nanocrystals are temporarily stabilized by PEG-400 and start to aggregate along the [001] direction, together with some lateral attachment of the {101} facets, leading to the formation of mesocrystalline anatase aggregates. In the subsequent calcination step, the anatase building blocks are fused to form single crystals with the spindle crystal shape and numerous nanopores. In another example, PEG-200 was also used to synthesize  $\beta$ - $\text{Ga}_2\text{O}_3$  PSC rods.<sup>[16e]</sup>



Cellulose can also provide adsorption sites to direct the growth of PSC precursor. Hexagon shaped mesoporous zinc oxide nanodisks (ZnO NDs) with exposed {0001} polar facets have been prepared by hydrothermal-calcination protocol using ethylcellulose (EC) and CTAB as morphology templating agents.<sup>[41]</sup> In the synthesis, CTAB molecules are proposed to act decreasing the surface tension of the solution, dismissing the energy required to form a new phase. CTA<sup>+</sup> ions bind by electrostatic interaction to negative zincate [i.e., Zn(OH)<sub>4</sub><sup>2-</sup>] ions organizing the growth of ZnO nanorod around the micelles. EC molecules are attached preferentially on the Zn<sup>2+</sup> populated (0001) crystal surface favoring the growth of those facets. Upon calcination, the EC molecules decompose and release CO<sub>2</sub> and H<sub>2</sub>O gas from the ZnO hexagonal disks to form the final porous structure (Path 1 in Scheme 10). Control experiments indicate the cooperation of both CTAB and EC to the formation of ZnO NRs. Using only CTAB or only EC, hexagonal ZnO nanorods (NRs) without porosity (Path 2 in Scheme 10) or ZnO nanosheets (NSs) composed of numerous NPs (Path 3 in Scheme 10) are formed, respectively.



**Scheme 10.** Proposed synthetic route for ZnO PSC nanodisks (NDs) (Path 1), nanorods (NRs) (Path 2), and nanosheets (NSs) (Path 3) under three different reaction conditions using a mixture of CTAB and EC (Path 1), or only CTAB (Path 2), and only EC (Path 3). Reproduced with permission.<sup>[41]</sup> Copyright (2015) American Chemical Society.

### 2.3.3. Decomposition of inorganic crystals

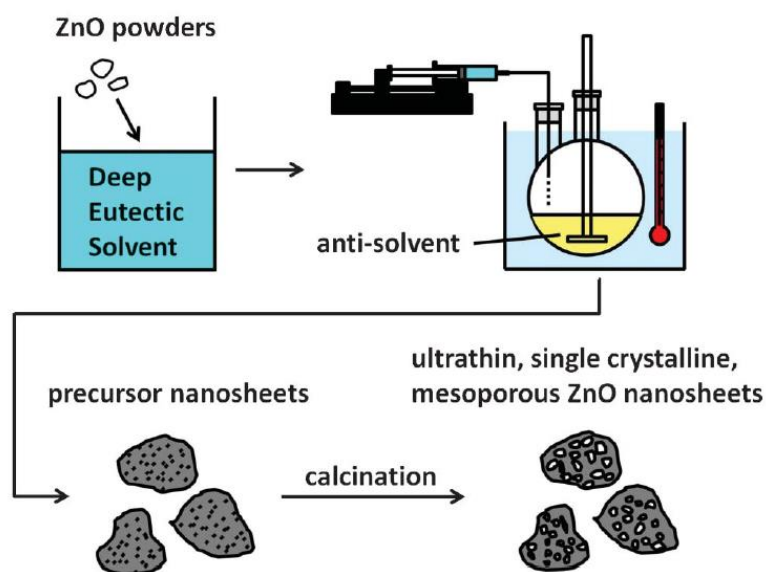
In this strategy, inorganic crystals with similar morphology than the final PSCs are first prepared by a liquid-phase reaction. Subsequently, these non-porous precursors are then decomposed by heating and transformed into PSCs with a considerable density of small voids which can further merge at high temperature into the desired porous structure. In the first step of this method, organic molecules rather than occupying lattice positions of crystalline compound precursors are acting as morphology controlling agents, or they are decomposed into simple inorganic ions such as  $\text{CO}_3^{2-}$  and  $\text{OH}^-$  able to react with metal ions. In a subsequent step, the formation of a porous structure is mainly caused by the decomposition of inorganic crystalline precursors, not organic templates. This method holds a special merit in the manipulation of the porous structures of materials. Usually, the metal compound precursors have their intrinsic crystal structures and morphologies that are different from the subsequent inheritors. However, the formation of derivative materials can be sensitive to antecessor structures, morphologies and forming procedures. Thus, this precursor-based decomposition method provides the opportunity for constructing a series of materials derived from precursors with similar morphologies and structures that would be difficult to obtain by other methods.<sup>[42]</sup> For instance, hematite ( $\text{Fe}_2\text{O}_3$ ) PSC can be prepared by the decomposition of iron hydroxide precursor. In this way hematite porous nanorods have been obtained from akagenite previously prepared by refluxing method.<sup>[17a]</sup> In the process, urea acts as the gradual precipitating agent for the controlled release of hydroxyl ions during the reaction.  $\text{Fe}(\text{OH})_3$

initially formed by reaction with the released hydroxyl ions is unstable in aqueous solution, and is quickly transformed into  $\beta$ -FeOOH upon prolonged reflux. Next, the akagenite nanostructures are topotactically transformed to porous hematite nanorods upon calcination. Using a different dehydration strategy, porous hematite nanopillars on FTO substrate have been synthesized from FeOOH nanorods.<sup>[17b]</sup> In this route, the FeOOH was directly placed into a 250 °C furnace to induce fast dehydration, instead of the conventional slow temperature-rising process, followed by a two-step high temperature annealing. The FeOOH nanopillars undergo immediate dehydration and quickly transform into Fe<sub>2</sub>O<sub>3</sub>. Due to its high melting point, the Fe<sub>2</sub>O<sub>3</sub> preserved the morphology of robust pillar arrays from the as-grown FeOOH, avoiding collapse, shrinking, and coalescence of the resulting Fe<sub>2</sub>O<sub>3</sub> 1D structure. The formation mechanism of nanopores in Fe<sub>2</sub>O<sub>3</sub> can be attributed to the fast release of water in the fast FeOOH dehydration during the initial annealing process. In another example, a mixture of PSC and polycrystalline nanowire (NWs) hematite has been also obtained by thermal conversion of  $\alpha$ -FeF<sub>3</sub>·3H<sub>2</sub>O prepared through a solution growth.<sup>[17c]</sup> The FeF<sub>3</sub>·3H<sub>2</sub>O precursor includes two types of morphologies, single-crystal NWs with smaller diameters and polycrystalline NWs with larger diameters. Because of their small size, short diffusion distance, and fast transformation, the thin NWs are quickly converted in the annealing routine into  $\alpha$ -Fe<sub>2</sub>O<sub>3</sub> PSC NWs without disturbing their single crystallinity.

ZnO PSC can be conveniently prepared by decomposing zinc carbonate hydroxide hydrate (Zn<sub>5</sub>(CO<sub>3</sub>)<sub>2</sub>(OH)<sub>6</sub>). Urea is often used to synthesize the Zn<sub>5</sub>(CO<sub>3</sub>)<sub>2</sub>(OH)<sub>6</sub> precursor through hydrothermal precipitation at moderate temperature. Under these conditions urea is decomposed to OH<sup>-</sup> and CO<sub>3</sub><sup>2-</sup> ions. Subsequent heat treatment would cause the release of H<sub>2</sub>O and CO<sub>2</sub> from Zn<sub>5</sub>(CO<sub>3</sub>)<sub>2</sub>(OH)<sub>6</sub>, generating numerous vacancies on ZnO particles resulting in the formation of ZnO PSCs. Following this method, ZnO porous nanoplates can be reliably synthesized.<sup>[43]</sup> By further adjustment of the temperature in the precursor synthesis, different morphologies such as porous nanosheet-assembled microflowers

(PNMFs), porous dispersed nanosheets (PDNs), and porous nanosheet-assembled microspheres (PNMSs) composed of PSC nanosheets can be prepared.<sup>[44]</sup> In addition, using CTAB as capping agent in the precursor synthesis, a nearly spherical morphology of hierarchically assembled PSC ZnO nanoplates can also be obtained.<sup>[45]</sup> Furthermore,  $\text{Zn}_5(\text{CO}_3)_2(\text{OH})_6$  can be decomposed during the hydrothermal process in competition with particle growth. Using CTAC, the growth of  $\text{Zn}_5(\text{CO}_3)_2(\text{OH})_6$  could be inhibited and in this way ZnO spherical particles formed by the stacking of PSC nanosheets could be obtained by a topotactic-like transformation of layered hydroxide zinc acetate (LHZA). LHZA was prepared in ethanolic-aqueous zinc acetate solution.<sup>[46]</sup> The formation of ZnO PSCs having mesopores occurs mainly due to the volume change during the topotactic transformation. In another example, a deep eutectic solvent (DES) based process was used to synthesize  $\text{Zn}_5(\text{CO}_3)_2(\text{OH})_6$  precursor which was further transformed into ZnO PSC nanosheets by calcination.<sup>[47]</sup> Urea and choline chloride were first mixed under argon at a molar ratio of 2 to 1 to form UCC (urea and choline chloride) as DES. Then, a certain amount of ZnO powder could be dissolved in DES. After addition of water as antisolvent, a precipitate was formed which transforms the dissolved ZnO particles into ZnO nanosheets. In the antisolvent procedure, nanosheets of a mixture of  $\text{Zn}_5(\text{CO}_3)_2(\text{OH})_6$  and ZnO are formed. The reason is that when the ZnO solution of DES is mixed with the antisolvent, the ZnO precursor undergoes precipitation because water does not dissolve ZnO, but water is totally miscible with DES. In DES, urea acts not only as the hydrogen bond donor component necessary in DES formation with choline chloride capable to dissolve ZnO powders, but also as the source of gradual release of carbonate and hydroxide to form the  $\text{Zn}_5(\text{CO}_3)_2(\text{OH})_6$  precursor. The subsequent calcination generates the ZnO nanosheets with a thickness around 10 nm and pore sizes increasing from less than 10 nm to several tens of nanometers by controlling calcination time and temperature (**Scheme 11**). In a different report, formation of ZnO PSC nanosheets

with hexagonal-wurtzite phase on Ti substrate has been described through heating the random zinc hydroxide nanosheet arrays.<sup>[48]</sup>



**Scheme 11.** Preparation procedure of ZnO PSC nanosheets by DES dissolution and subsequent antisolvent addition. Reproduced with permission.<sup>[47]</sup> Copyright (2012) Royal Society of Chemistry.

TiO<sub>2</sub> PSCs can be prepared by decomposing TiOF<sub>2</sub><sup>[42]</sup> and hydrogen titanate.<sup>[49]</sup> TiOF<sub>2</sub> precursor with a flower-like structure formed by assembled nanosheets was prepared by the solvothermal method. After calcination, the sheet-like shape of TiOF<sub>2</sub> precursor is inherited by TiO<sub>2</sub> and the TiOF<sub>2</sub> precursor is transformed to anatase with a high density of square pores generated by HF loss.<sup>[42]</sup> Moreover, TiO<sub>2</sub> films consisting of mesoporous anatase nanowires and rutile nanorods were obtained on PET fabrics by decomposition of hydrogen titanate.<sup>[49]</sup> Due to the poor oxidation resistance at high temperature of PET substrates, the decomposition of hydrogen titanate and crystallization of TiO<sub>2</sub> were performed by hydrothermal treatment in aqueous H<sub>2</sub>SO<sub>4</sub>. The SO<sub>4</sub><sup>2-</sup> ions favor anatase formation, while acid pH values are favorable for the formation of rutile. Thus, the final TiO<sub>2</sub> nanowires are a mixture of anatase and rutile PSC structure.

Besides the above commented metal oxides, NiO, CuO, Co<sub>3</sub>O<sub>4</sub> and Ta<sub>2</sub>O<sub>5</sub> PSCs have also been prepared by decomposition of crystalline precursors, in which NiO PSC nanosheets were obtained from nickel hydroxide,<sup>[50]</sup> and dumbbell-shaped CuO particles consisting of microrod-like CuO PSCs were obtained from copper carbonate hydroxide hydrate.<sup>[51]</sup> Hollow Co<sub>3</sub>O<sub>4</sub> microspheres composed of PSC ultrathin nanosheets were synthesized by dehydration of cobalt hydroxide.<sup>[52]</sup> In the last case, the procedures involve three steps: (1) solid cobalt alkoxide microspheres (s-CoA) were synthesized by solvothermal reaction; (2) s-CoA was transformed by the Kirkendall effect into hollow cobalt hydroxide microspheres (h-CoOH) composed of ultrathin nanosheets through hydrothermal treatment.<sup>[53]</sup> Finally, in the last step (3), hollow Co<sub>3</sub>O<sub>4</sub> material was obtained by calcination of h-CoOH in air. Cubic Ta<sub>2</sub>O<sub>5</sub> PSCs with active facets were obtained by calcination TaO<sub>2.18</sub>Cl<sub>0.64</sub> precursor under Ar gas.<sup>[54]</sup> The calcination for the TaO<sub>2.18</sub>Cl<sub>0.64</sub> only caused an intralayer transition; the {001} facets were preserved because of the strong 180 ° Ta–O–Ta structure connecting the layers. Consequently, the crystal structure and cubic morphology of the tantalum oxychloride precursor resulted inherited by Ta<sub>2</sub>O<sub>5</sub> PSCs. The mesoporous structure of Ta<sub>2</sub>O<sub>5</sub> PSCs was induced by the escape of HCl during calcination.

Other material, BiFeO<sub>3</sub> PSCs, was obtained via a multi-step single-crystal to single-crystal transformation of bismuth ferricyanide hydrate (Bi[Fe(CN)<sub>6</sub>]•4H<sub>2</sub>O).<sup>[55]</sup> Firstly, Bi[Fe(CN)<sub>6</sub>]•4H<sub>2</sub>O sheets with X-shape were synthesized by precipitation. Then, Bi[Fe(CN)<sub>6</sub>]•4H<sub>2</sub>O sheets was calcined to produce BiFeO<sub>3</sub> PSCs in air at relatively low temperature, 400 °C. During the calcination, Bi[Fe(CN)<sub>6</sub>]•4H<sub>2</sub>O is first oxidized and transformed to an amorphous matrix. Then, upon calcination BiFeO<sub>3</sub> undergoes gradual crystallization. Finally, the crystalline domains undergo self-adjustment of the orientation leading to a monocrystalline framework. Such multiple-step process exhibits, low energy barriers in each step. For this reason, the crystallization temperature in this procedure is lower compared to other methods to obtain BiFeO<sub>3</sub>.<sup>[56]</sup>

#### 2.3.4. Imperfect merging of NPs

In this strategy, the pores in PSCs are not caused by the occupancy of adventitious templates (hard or soft) or by the decomposition of precursor compounds, but mainly by the imperfect fusion of adjacent NPs. In the examples using this strategy, voids among NPs are preserved when these components merge into a complete crystal. The pore system can evolve into the final porosity structure during the merging process depending on the time and temperature. Fusion of NPs is often caused by dehydration and condensation. The morphology of the NPs can be nanocrystals or amorphous particles. Obviously, such merging is also involved in many other strategies. However, this process may be not dominant in the formation of pores in those other strategies. For example, in the templating approach, although merging of NPs may also cause some pores in PSCs, most pores are induced by the decomposition of templates. Therefore, templates are necessary in the formation of the resulting pores.

Therefore, these studies are better classified into previous sections.

As an example of imperfect fusion of NPs, SrTiO<sub>3</sub> PSC assemblies were produced via a hydrothermal synthesis.<sup>[57]</sup> At the initial stage in the material formation, the local crystallographic transformation is initiated by intercalation of Sr<sup>2+</sup> into titanate during the hydrothermal process, resulting in small SrTiO<sub>3</sub> NPs on titanate nanosheets. In the growth and aging of the crystal, some atom vacancies are generated in the SrTiO<sub>3</sub> NPs through dehydration and condensation. In the aggregation step, the adjacent SrTiO<sub>3</sub> NPs tend to arrange in a similar crystallographic orientation due to the templating effect of titanate. As the reaction proceeds, the small SrTiO<sub>3</sub> nanocubes are dissolved, while the large ones continue the growth and touch each other, according to the Ostwald-ripening mechanism. To minimize the surface energy, the attached SrTiO<sub>3</sub> nanocubes rotate themselves to produce a coherent

lattice structure at the interfaces, thereby forming a single crystal hierarchical structure with numerous pores. **Figure 7** illustrates the various steps in the process.

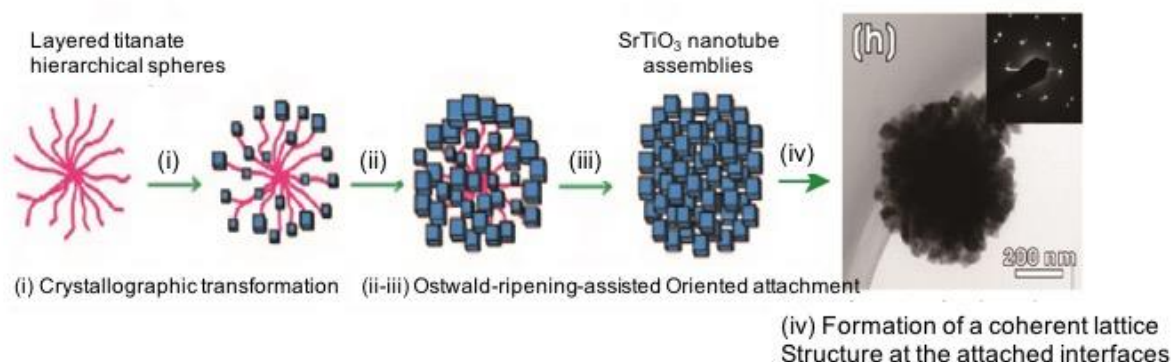


**Figure 7.** Illustration of the growth mechanism from layered titanate hierarchical spheres to SrTiO<sub>3</sub> PSCs. Reproduced with permission.<sup>[57]</sup> Copyright (2013) American Chemical Society.

The aggregation-merge process has also been used to synthesize at a relatively low temperature a SrTiO<sub>3</sub> PSC with shallow pits by an exothermal alkali-dissolution reaction that provides simultaneously alkalinity and temperature for the crystallization of the amorphous precursor.<sup>[10]</sup> A cellular SrTiO<sub>3</sub> sample was prepared by a molten-salt method to control the material synthesis.<sup>[12a]</sup> Similarly, a Bi<sub>2</sub>WO<sub>6</sub> PSCs with tetragonal architecture could be also prepared by a molten-salt method.<sup>[12b]</sup> Moreover, ZnO hierarchical microflowers (MFs) constructed by interlaced nanosheets with many pits were synthesized by the direct precipitation of zinc nitrate hexahydrate in an alkaline environment at room temperature.<sup>[58]</sup> In addition, anatase TiO<sub>2</sub> PSCs with a morphology of disordered mesoporous cages have also been prepared via solvothermal synthesis.<sup>[5a]</sup> In the procedure, clusters of TiO<sub>2</sub> were first formed through hydrolysis and condensation of the precursor. Then, the clusters forming initially amorphous particles undergo crystallization. The adjacent nanocrystals attach with each other along their (101) planes. Finally, these nanocrystals become fused into a continuous single-crystalline structure with a considerable density of pores. It should be noted that chemical etching can also occur, contributing to the formation of small voids or leading



to the enlargement of the pores during the subsequent reaction process (e.g. Ostwald ripening). Based on such dissolution and oriented crystal growth, a mesoporous anatase TiO<sub>2</sub> film with 5 – 10 nm pores and preferred [001] crystalline-orientation has been obtained on FTO glass.<sup>[59]</sup>

### 2.3.5 Self-etching

The crystal growth involves mass transfer in liquid and solid phases near the solid-liquid interface. When the rate of atom migration from liquid to solid is larger than from solid to liquid, the solid grows; otherwise the solid dissolves. This dissolution-crystallization equilibrium is mainly controlled by the local temperature and local solution concentration. The difference in these parameters among different points can lead to surface roughening or even the creation of pores by dissolution. Dissolution of solid often takes place in some instable high energy sites, for example, defects sites. The generated voids are often not healed by atom deposition due to spatial differences of dissolution-precipitation process. The formation of PSC by “*self-dissolution*” is frequently denoted as “*etching*”. This mechanism has been used to obtain a hollow ZnO PSC via microwave-assisted hydrothermal synthesis.<sup>[5b]</sup> The small pores in ZnO PSCs were caused by dissolution of structural defects in contact with liquid phase.

The local solution concentration near interface can be affected by both metal precursors and additives. If the additives themselves or their decomposition products are corrosive to the targeted crystals, an extra etching effect besides “*self-dissolution*” can be produced and removal of parts in the crystal will result in a porous architecture of desired materials. Such etching during the formation of PSCs has been denoted as “*self-corrosion*”. In this mechanism, porosity and pore size are adjusted by varying the starting phase ratio and

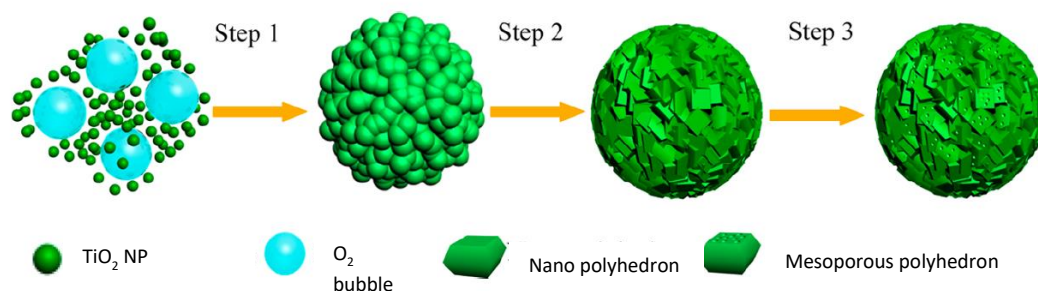
reaction temperature. Most of the current studies regarding the preparation of PSCs belong to this “*self-corrosion*” mechanism.

Due to its good chemical stability, TiO<sub>2</sub> is difficult to be corroded by common reagents. HF is among the few chemicals able to form pores in TiO<sub>2</sub> crystals. HF can be added separately, or this reagent could be generated by decomposition of reactants containing F. In addition, because the presence of F<sup>-</sup> ions can diminish the growth rate of (001) facets in TiO<sub>2</sub>, its presence can result in the formation of anatase TiO<sub>2</sub> single crystals with exposed {001} facets. Thus, formation of pores via HF corrosion is usually associated also with preferential facet orientation of anatase crystals. By adding HF directly into the reaction, TiO<sub>2</sub> PSC films with exposed {001} facets and uniform nanopores have been prepared on a clean Ti substrate by means of hydrothermal synthesis followed by calcination. The sizes of the nanopores could be controlled by adjusting the temperature of the process.<sup>[17d, 17e]</sup> Using NH<sub>4</sub>F as the source of HF, a PSC TiO<sub>2</sub> film was produced by metal sputtering and subsequent anodization.<sup>[13]</sup> The obtained film displays vertically aligned and well-connected one-dimensional PSC nanorods with 10–20 nm width and 40 nm length. In addition, with (NH<sub>4</sub>)<sub>2</sub>TiF<sub>6</sub> as the source of HF, mesoporous TiO<sub>2</sub> single crystal was also synthesized by a hydrothermal-calcination process.<sup>[60]</sup>

The anisotropic corrosion caused by HF attack to different crystalline facets can result in the formation of TiO<sub>2</sub> PSCs.<sup>[61]</sup> In the last stage of a hydrothermal synthesis, excessive HF can etch the more reactive (001) facets and leave the (101) facets with lower surface energy. Such selective corrosion could be not corrected by the crystal growth. Due to the concentration gradient of HF along the corrosion direction, the formed holes may exhibit tapered shape. Consequently, TiO<sub>2</sub> PSCs with exposed (101) facets were synthesized (**Scheme 12**).

Furthermore, it was found that isopropanol (IPA) could accelerate the HF corrosion to TiO<sub>2</sub> crystals.<sup>[62]</sup> In a two-step solvothermal routine, the synthesized square-TiO<sub>2</sub> single crystals

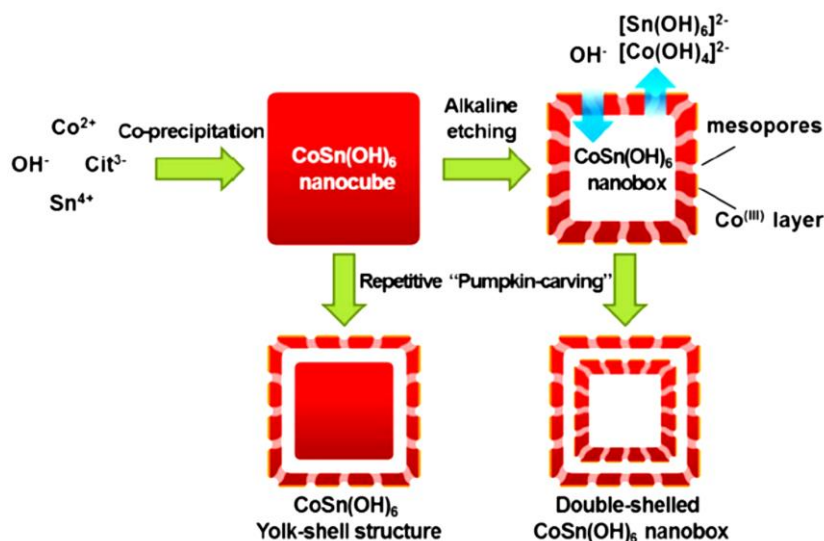
were further treated by the solvothermal method with IPA as additive. The (001) facets of TiO<sub>2</sub> crystals were found to be easily eroded in the solution containing isopropanol.



**Scheme 12.** Steps in the formation of the core–shell-structured TiO<sub>2</sub> PSC microsphere. At step 3, tapered holes on the shell of the NPs are generated due to HF corrosion. Reproduced with permission.<sup>[61]</sup> Copyright (2014) American Chemical Society.

Similarly, NH<sub>3</sub> has been utilized to corrode copper compounds by forming soluble amine complexes and then to generate Cu<sub>2</sub>O PSC spheres.<sup>[63]</sup> The formation of Cu<sub>2</sub>O through a room-temperature precipitation and local corrosion is based on a mechanism of coordination-assisted heterogeneous dissolution (CHD). At the initial stage of reaction, [Cu(NH<sub>3</sub>)<sub>n</sub>]<sup>2+</sup> species are formed. Upon addition of a NaOH solution, OH<sup>-</sup> cannot replace all the NH<sub>3</sub> ligands in the [Cu(NH<sub>3</sub>)<sub>n</sub>]<sup>2+</sup> complex due to the low OH<sup>-</sup>/Cu<sup>2+</sup> molar ratio. Consequently, some NH<sub>3</sub> ligands are still present on the Cu<sup>2+</sup> coordination polyhedron and [Cu(NH<sub>3</sub>)<sub>2-x</sub>(OH)<sub>2+x</sub>]<sup>x-</sup> species are formed. In the structure, NH<sub>3</sub> can be enriched at certain positions around the copper hydroxide, leading to a heterogeneous dispersion of NH<sub>3</sub> in the evolving solid. When adding N<sub>2</sub>H<sub>4</sub> · H<sub>2</sub>O, Cu(OH)<sub>2</sub> becomes reduced to Cu<sub>2</sub>O. Meanwhile, the specific parts of Cu<sub>2</sub>O enriched with NH<sub>3</sub> will heterogeneously dissolve, finally leading to the formation of a porous structure. Because the freshly formed Cu<sub>2</sub>O has a single crystalline structure, the porous structure generated from the non-uniform dissolution still preserves the same single crystalline framework.

By elaborately utilizing alkaline etching process, unique  $\text{CoSn}(\text{OH})_6$  PSC nanoboxes with uniform size and porous shell have been prepared by a precipitation-dissolution protocol.<sup>[64]</sup> Formation of  $\text{CoSn}(\text{OH})_6$  PSC nanoboxes can be attributed to the fast growth of  $\text{CoSn}(\text{OH})_6$  nanocubes and subsequent kinetically-controlled etching in alkaline medium, which includes three steps. Firstly, perovskite-type  $\text{CoSn}(\text{OH})_6$  is formed in aqueous solution by co-precipitation of  $\text{Sn}^{4+}$ ,  $\text{Co}^{2+}$  and  $\text{OH}^-$  in the presence of citrate ions. Single crystalline nanocubes are spontaneously obtained due to intrinsic cubic crystal structure. Owing to the amphoteric nature,  $\text{CoSn}(\text{OH})_6$  nanocubes can be gradually dissolved by excess amount of  $\text{OH}^-$  in alkaline solution, generating soluble  $[\text{Co}(\text{OH})_4]^-$  and  $[\text{Sn}(\text{OH})_6]^{2-}$  species. During this solubilization process, because the thermodynamically favorable aerobic oxidation of  $[\text{Co}(\text{OH})_4]^-$ , an insoluble outermost layer of Co (III) species is quickly produced on the surface of  $\text{CoSn}(\text{OH})_6$  crystals. This  $\text{CoSn}(\text{OH})_6$  layer makes the outer surface of cubes more inert than their interior that undergoes preferential alkaline etching. As the dissolution of the core  $\text{Co}^{+2}$  material continues, mesoporous  $\text{CoSn}(\text{OH})_6$  hollow nanoboxes are eventually generated without the loss of crystallinity. Furthermore,  $\text{CoSn}(\text{OH})_6$  hollow structures with complex interiors, for example yolk-shell and multi-shelled nanoboxes, can be additionally also formed without losing single crystallinity, by repeated deposition of  $\text{CoSn}(\text{OH})_6$  layers on pre-formed  $\text{CoSn}(\text{OH})_6$  nanoboxes and successive alkaline etching (**Scheme 13**).



**Scheme 13.** Procedures for the formation of  $\text{CoSn}(\text{OH})_6$  PSC hollow nanoboxes,  $\text{CoSn}(\text{OH})_6$  yolk-shell particles and multishelled nanoboxes (citrate anion is denoted as  $\text{Cit}^{3-}$ ). Reproduced with permission.<sup>[64]</sup> Copyright (2013) Springer Nature.

### 2.3.6 Ion-exchange

The concept of this strategy is to use ion exchange to replace atoms on the initial lattice inducing a concomitant volume change and eventually the formation of pores. The ion exchange strategy for preparing PSCs can be classified either as cation or as anion exchange. The cation exchange reaction, first proposed by Alivisatos et al.<sup>[65]</sup>, has been widely used to synthesize nanostructured chalcogenides ( $\text{ZnX}$ ,  $\text{CdX}$ ,  $\text{Cu}_{2-x}\text{X}$ , where  $\text{X}=\text{S}$ ,  $\text{Se}$ ,  $\text{Te}$ ).<sup>[66]</sup> Usually, cation exchange occurs under relatively low temperature, mainly due to thermodynamic driving force to form a new structure with lower internal energy. Conversely, external energy is typically needed to promote anion exchange, resulting in higher temperature requirements. Currently PSCs formation by anion exchange is limited to the nitridation of oxides and the oxidation of metal sulfides. The ion exchange strategy can preserve the morphology or crystallographic phase of the precursor material generating numerous pores at the same time, thus, being a promising synthetic method for the preparation of PSC-based materials.

#### *Cation exchange*

A cation exchange strategy has been successfully applied to fabricate  $\text{Cd}_x\text{Zn}_{1-x}\text{S}$  PSC nanosheets using  $\text{ZnS}(\text{DETA})_{0.5}$  (DETA: diethylenetriamine) hybrid sheets as the starting materials.<sup>[14]</sup> Under synthesis conditions, cation exchange occurs fast and most of the zinc ions in  $\text{ZnS}(\text{DETA})_{0.5}$  could be exchanged by cadmium cations in a short time. It was found that the reverse ion exchange, namely starting with  $\text{CdS}(\text{DETA})_{0.5}$  and attempting zinc cation

exchange does not occur under the same conditions, suggesting that the driving force for the cation exchange is the enthalpy-driven formation of CdS.<sup>[67]</sup> Formation of voids in the nanosheets can be understood due to the rapid kinetics and strain release caused by the large lattice mismatch between ZnS and CdS up to 7-8 %. Furthermore, the dissolution of DETA in water is also responsible for void formation. This ion exchange finally results in the formation of  $\text{Cd}_x\text{Zn}_{1-x}\text{S}$  nanosheets with PSC structure. The method has also been used to prepare nanoporous  $\text{Cd}_x\text{Zn}_{1-x}\text{Se}$  and  $\text{Cr}_x\text{Ce}_{1-x}\text{O}$  nanorods.<sup>[14]</sup> Moreover, CdSe PSC nanobelts could also be prepared by similar cation exchange strategy starting from  $\text{ZnSe}\cdot 0.5\text{N}_2\text{H}_4$  hybrid nanobelts as precursors.<sup>[68]</sup>

Unusually, PSCs of relatively inert  $\text{TiO}_2$  could also be produced by the cation exchange strategy.<sup>[69]</sup> A selectively branched, 2D anatase  $\text{TiO}_2$  PSC nanostructure on FTO substrate has been synthesized by ion exchange followed by calcination. Firstly, layered potassium titanate (K-titanate) was synthesized on seeded FTO glass through a hydrothermal-calcination process. Then, the ion exchange treatment was performed on the film by soaking it in HCl solution causing the conversion of 2D K-titanate to protonated titanate (H-titanate). In the ion exchange process, the substitution of  $\text{K}^+$  ions by smaller  $\text{H}^+$  ions causes a structure collapse into small pieces of H-titanate consisting of disordered octahedral  $\text{TiO}_6$  units. In subsequent calcination, the reorganization and dehydration of these  $\text{TiO}_6$  units would cause the formation of crack-free anatase  $\text{TiO}_2$  PSCs with abundant pores (**Figure 8**).

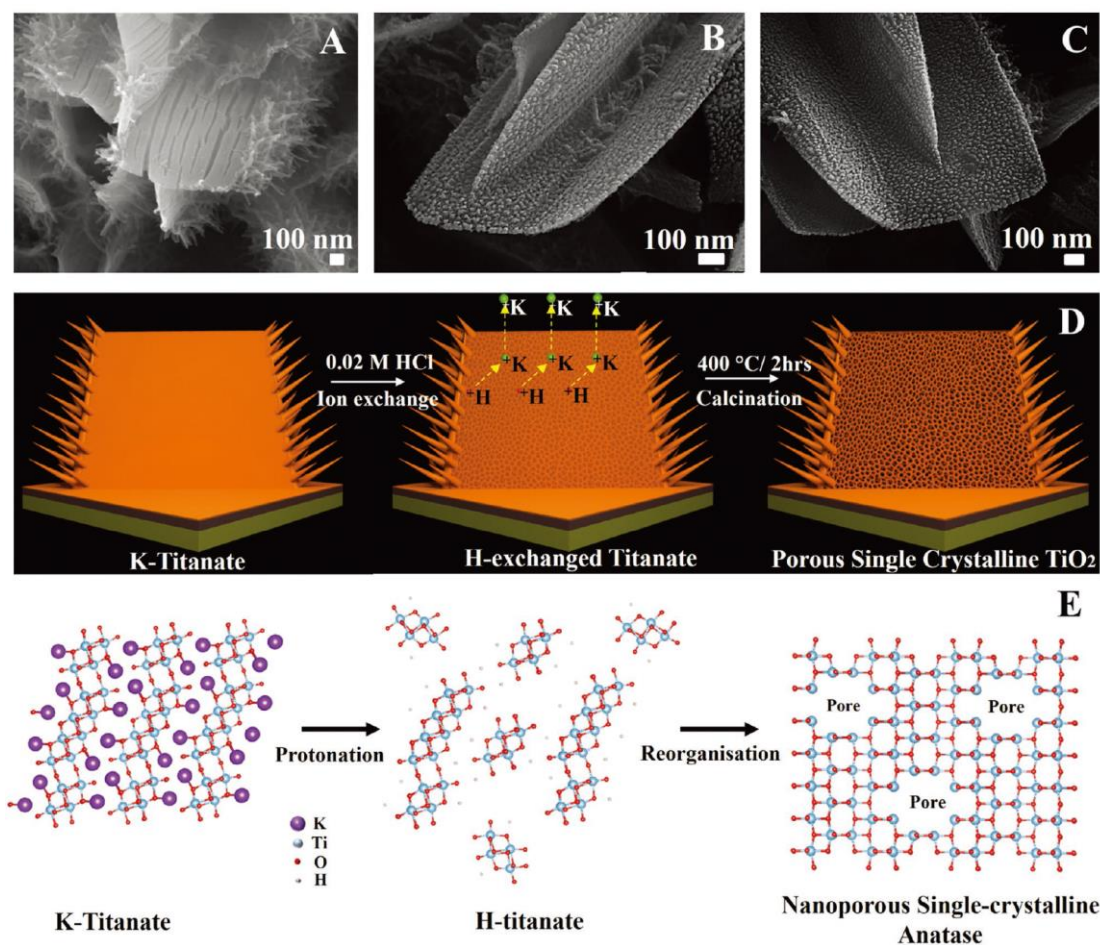


**Figure 8.** SEM evolution from K-titanate to TiO<sub>2</sub> PSC via K<sup>+</sup> to H<sup>+</sup> ion exchange followed by calcination, (A) K-titanate, (B) H-titanate, and (C) TiO<sub>2</sub> PSC; (D) Schematic illustration of the conversion of K-titanate to TiO<sub>2</sub> PSC; (E) Proposed evolution of model crystal structure during ion exchange and calcination processes. Reproduced with permission.<sup>[69]</sup> Copyright (2018) John Wiley and Sons.

### *Anion exchange*

Regarding the formation of PSC materials, anion exchange is limited to the nitridation of metal oxides, and the oxidation of metal sulfides. Due to the smaller sizes of nitrogen than oxygen and oxygen than sulfur, nitridation and oxidation could cause a similar lattice shrinkage to that previously commented in cation exchange resulting in the formation of

pores. Following this strategy, single crystalline meso- and macroporous  $\text{LaTiO}_2\text{N}$  (LTON) has been prepared by a high-temperature ammonization using oxide  $\text{La}_2\text{Ti}_2\text{O}_7$  as precursor<sup>[70]</sup>. In the preparation,  $\text{La}_2\text{Ti}_2\text{O}_7$  oxide precursor was first prepared either by a flux method (noted as FX-LTO) or the polymerized complex method (PC-LTO). Then, both types of LTON were nitrated by high-temperature calcination under a flow of  $\text{NH}_3$ , resulting in the final materials (FX-LTON and PC-LTON, respectively). Formation of pores is not a random process, but depends on the nitridation that generates small pores to compensate for the unit cell volume contraction, while the whole particle size distribution was retained.<sup>[71]</sup> With a similar nitridation strategy, TiN PSC nanoplates on carbon fibers have also been prepared from  $\text{TiO}_2$ .<sup>[72]</sup> In addition, TaON PSC microspheres have been prepared by simultaneous nitridation and crystallization of amorphous  $\text{Ta}_2\text{O}_5$  sphere obtained by hydrothermal synthesis.<sup>[73]</sup> Through thermal oxygen exchange, ZnO PSC nanobelts (NBs) have been prepared by calcination of  $\text{ZnS}(\text{en})_{0.5}$  (en: ethylenediamine) NBs synthesized by a solvothermal procedure on alumina substrates.<sup>[74]</sup> At the starting stage of the ZnS NBs oxidation process, ZnO grains at the ZnS crystal edges are formed through the exchange between oxygen and sulfur, leading to a ZnS core surrounded by ZnO grains oriented according to the original ZnS lattice. After prolonging thermal annealing, aperture of pores occurs releasing the tensile stress caused by strong lattice contraction, due to the large lattice mismatch between ZnS and ZnO. Following a similar method, ZnO PSC platelets have also been synthesized by using  $\text{ZnCl}_2$  or single spheroidal Zn particle as metal source.<sup>[75]</sup> In addition, ZnO PSC nanobelts have also been synthesized by annealing  $\text{ZnSe}\cdot 0.5\text{N}_2\text{H}_4$  precursor prepared via hydrothermal reaction.<sup>[76]</sup>

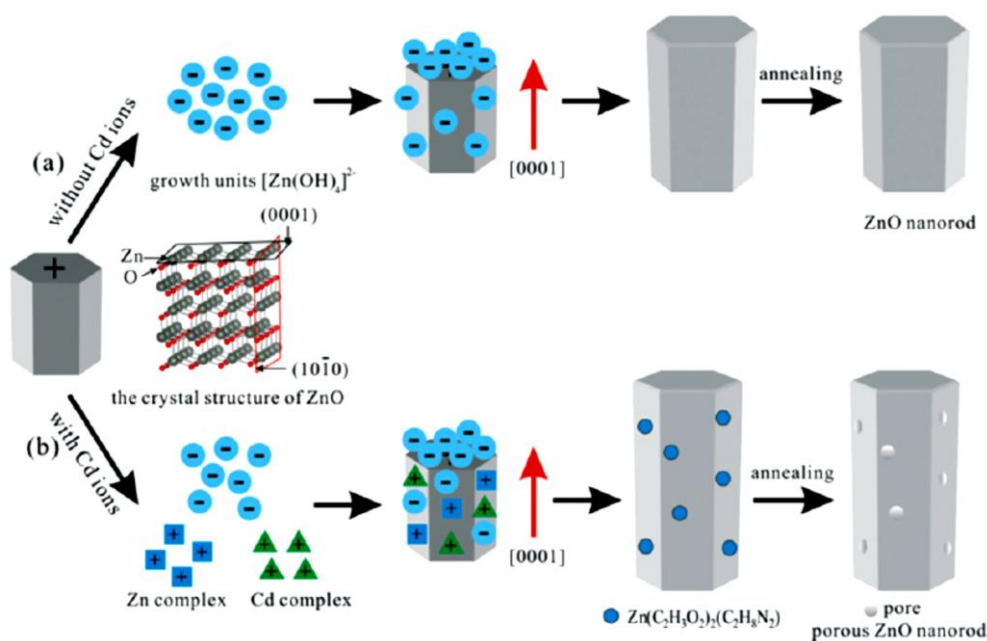
### 2.3.7 Other preparation methods

Competitive adsorption has been employed to prepare porous ZnO single crystal nanorod (NR) arrays with small NPs in the pores.<sup>[77]</sup> In order to obtain oriented ZnO arrays, a seed



layer on the surface of FTO glass is first deposited by dip coating. Then, the seeded FTO is immersed into the growth solution containing zinc acetate, cadmium sulfate and ethylenediamine. Such growth process was repeated three times. Finally, the ZnO film was annealed to obtain a well-aligned and well-crystallized porous ZnO NR array.

Ethylenediamine acts as a pH buffering agent, slowly releasing  $\text{OH}^-$  ions causing the growth of ZnO nanorods. In the nucleation period,  $\text{Zn}(\text{OH})_4^{2-}$  ions are adsorbed preferably on the positive (0001) facet terminated by Zn atoms, promoting the oriented growth of ZnO nanorods along [0001]. Positive Cd complexes are adsorbed on the neutral lateral surface of nanorods rather than on the (0001) facet, due to face-selective electrostatic interactions. When  $\text{OH}^-$  groups are consumed by  $\text{Cd}^{2+}$ ,  $\text{Zn}^{2+}$  near the lateral surface has to combine other ions to form organic Zn complexes. In the following growth, the new Zn complexes stack together to form  $\text{Zn}(\text{C}_2\text{H}_3\text{O}_2)_2(\text{C}_2\text{H}_8\text{N}_2)$ , which is more stable than the Cd complex and, thus, could be kept on the surface of nanorods under subsequent cleaning treatment. After calcination, mesopores are created on the  $\{10\bar{1}0\}$  surface of ZnO NRs, due to the decrease of the particle size and gas generation (**Scheme 14**).

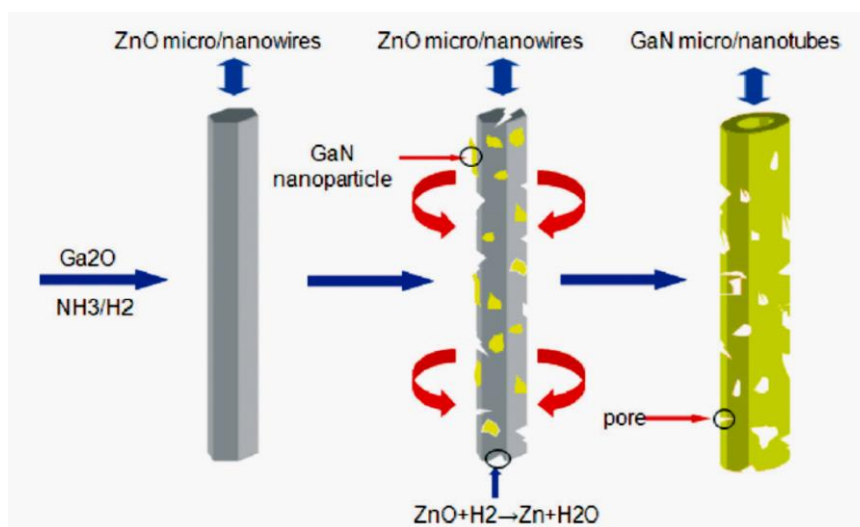


**Scheme 14.** illustration of the growth mechanism of pristine ZnO NR in the absence (a) or in the presence (b) of  $\text{Cd}^{2+}$  ions. In the last case ZnO PSC NRs are formed. Reproduced with permission.<sup>[77]</sup> Copyright (2016) Royal Society of Chemistry.

Chemical vapor deposition (CVD) is a widely used technique to produce thin films. In typical CVD, the substrate is exposed to volatile precursors, which can react and/or decompose on the substrate surface to generate the desired coating, while volatile byproducts are removed by the gas flow of the reaction chamber. The merits of CVD can be utilized to elaborately prepare PSCs. Thus, a two-steps CVD method has been used to prepared large-area gallium nitride PSC micro/nanotube arrays.<sup>[11]</sup> In the preparation, ZnO arrays were first grown on Si wafers by heating Zn powder under a mixture of Ar and  $\text{O}_2$  gases. The diameter of ZnO arrays could be adjusted by changing the distance between the Zn powder and the Si wafer. Then, a mixture of gallium and gallium oxide powder and ZnO micro/nanowire arrays were used as precursors with preservation of some distance between them. This mixture was heated under  $\text{NH}_3$ /argon/hydrogen mixed gas to form GaN PSC arrays. The formation mechanism of GaN tube is as follows.  $\text{Ga}_2\text{O}$  is formed in the second CVD step from the mixture of Ga/ $\text{Ga}_2\text{O}_3$  as the gas precursor of gallium. With the increase of temperature,  $\text{Ga}_2\text{O}$  starts to react with ammonia to generate GaN and hydrogen. Then, the epitaxial growth of GaN occurs on the surface of ZnO nanowires. At the initial stage, a considerable amount of GaN layers become attached onto the surface of ZnO nanowires, assembling into NPs. Meantime, some parts of ZnO nanowire without being covered by GaN molecules are reduced by hydrogen to produce gaseous Zn and  $\text{H}_2\text{O}$  at the reaction temperature of the CVD experiment. In these parts where Zn evaporates the pores are formed. In subsequent stages, the GaN NPs grow, connect and merge into a single crystal tube. When the ZnO nanowires completely disappear, the porous GaN tubes are obtained (**Scheme 15**). The presence of hydrogen is crucial to obtain a porous

tube since this gas must reduce ZnO to Zn metal that sublimates under the CVD conditions.

Without hydrogen a ZnO/GaN core-shell structure is obtained.



**Scheme 15.** Process of the CVD epitaxial growth of GaN PSC micro/nanotubes. Reproduced with permission.<sup>[11]</sup> Copyright (2013) Royal Society of Chemistry.

Ion implantation is another widely used modification technique in materials science.<sup>[78]</sup> In the ion implantation process, ions of one element are electrostatically accelerated and impinge on a solid target, thereby altering the physical properties and chemical composition of the target when the ions stay in the target. Ion implantation can be used in cases where the amount of chemical damage required is small by applying reasonably small dose. Ion implantation is particularly useful when the desired change (for example, structure and chemistry) is just limited to the surface of the target.

A routine using multiple-energy helium ion implantation and subsequent annealing was used to prepare a kind of porous rutile TiO<sub>2</sub> nanorod array.<sup>[17f]</sup> The TiO<sub>2</sub> nanorod arrays were first prepared on FTO substrate via a hydrothermal-calcination method using TBOT as source and hydrochloric acid to promote hydrolysis. Then the helium ion implantation with several different energies and fluences was conducted on the previously obtained TiO<sub>2</sub> arrays to create a relatively uniform helium concentration profile throughout the nanorods. The

implanted helium atoms become trapped by the defects in TiO<sub>2</sub> nanorod arrays and, then, aggregate into gas bubbles, due to the insolubility of helium atoms in TiO<sub>2</sub>. Formation of these helium bubbles can be greatly increased at sufficiently high fluence. Upon thermal annealing, these bubbles can continue growing by merging other dispersed helium atoms. When a high annealing temperature is reached, helium atoms would escape from TiO<sub>2</sub> arrays and then nano cavities are observed. Thus, TiO<sub>2</sub> arrays with numerous nanopores could be produced (Figure 9).

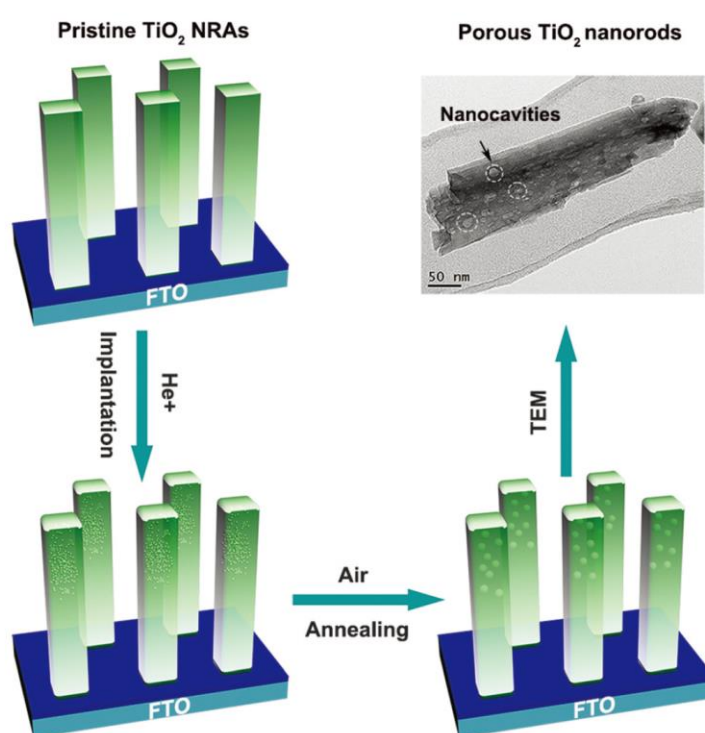


**Figure 9.** Fabrication process of rutile TiO<sub>2</sub> PSC nanorods by helium ion implantation and subsequent annealing Reproduced with permission.<sup>[17f]</sup> Copyright (2015) Royal Society of Chemistry.

Due to the stringent practical requirements, composite technologies (for example, hard-templating plus soft-templating plus self-assembly,<sup>[36]</sup> CVD epitaxial growth plus hard-templating, etc)<sup>[11]</sup> are becoming increasingly used to produce complicated porous structures. As already commented, many procedures of pore formation are often accompanied by other

spontaneous processes, such as merging and self-dissolution of NPs, leading to more than one mechanism for pore generation during the synthesis of PSCs. Consequently, some of the recent studies are becoming increasingly difficult to classify strictly in a single pore forming manner. However, they can be still categorized by the main mechanism, as it is done here, to better grasp the development of this field. Various forming manners of PSCs have their own special characteristics, for example, inverse replica approach can accurately control the shape of the pores. Decomposition of organic groups can be achieved using diverse organic molecules, allowing the large-scale production of PSCs by relatively simple synthetic protocols. Imperfect merging of NPs can form hierarchically porous structure without additives. Self-etching can maintain the initial shape of crystals, when the pore system is generated by partial corrosion of crystals with corrosive reagents, or by surface coarsening resulting from unbalance between growth and dissolution of crystals. Crystal decomposition can be easily achieved in hydrates, carbonates, acetates, etc. that are thermally unstable structures, facily producing PSCs. Ion exchange can serve to produce self-doping when forming PSCs. CVD epitaxial growth and ion implantation can also produce some porous structures in combination with other technique. The wide use of these pore forming technologies can serve to obtain PSCs with opportunities in the field of renewable energy and environment.

In addition to the previous comment, it should be remarked that each approach has still some shortages and drawbacks that have to be overcome by further development. For example, in the inverse replica method, the workup is often onerous, especially regarding the preparation and complete removal of template, leading to a PSCs low yield. In the procedures based on the decomposition of organic groups, the pore structure is not easily controlled. Imperfect merging of NPs cannot achieve simultaneously high crystallinity and the preservation of porosity (because the higher the crystallization temperature, the lesser the preserved voids). Self-corrosion often introduces strong corrosive and toxic reagents, and self-dissolution often

produces incompletely developed pores such as shallow pits. Decomposition of inorganic groups and ion exchange procedures can be only applied to a narrow type of materials. CVD epitaxial growth and ion implantation need expensive equipment, leading to high production costs. Although these issues limit the application range of each method, future developments of current procedures could result in highly efficient preparation procedures of PSCs at low cost and good quality.

#### **2.4. Modification of PSCs**

Porosity can greatly increase surface area and the number of accessible surface active sites of single crystals, allowing diffusion of substrates and reactants to the catalyst sites with the consequent enhancement of activity. In general, porosity only leads to the morphological change of the crystals; the intrinsic energy band structure of PSCs remains mostly unaltered without extension to the visible wavelength absorption onset. Thus, it is generally necessary to further modify PSCs by additional treatments to achieve the wanted visible light absorption to have efficient solar light responsive semiconductors.

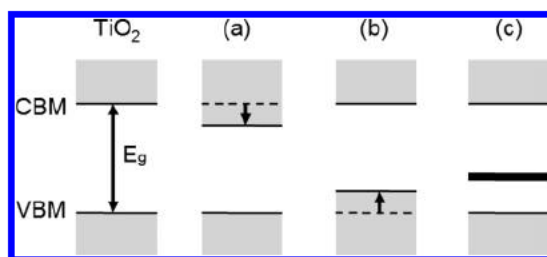
The most common modifications for PSC materials in photoconversion applications include doping, building semiconductor-semiconductor heterojunction, noble metal loading, deposition on carbon materials and surface amorphization. Combination of these treatments with the unique morphology of PSCs can result in a thorough control of the electronic and catalytic properties of the single crystal. That is, not only porosity and morphology, but also the band structure and electron transfer properties can be improved so that the performance of the semiconductors can be maximized especially in applications that required vectorial electron transfer along certain directions respect the crystal.

Most modifications to PSCs belong to post-treatments in which the structure and morphology of PSCs are largely preserved. However, in some cases such as non-metal doping, dopants

may disturb the nucleation and growth of crystals, so the preparation conditions are more stringent than these of metal doping.<sup>[79]</sup> Moreover, sometimes the modification process can be elaborately coupled with PSC preparation, forming novel structures, for example, sandwiched graphene-modified TiO<sub>2</sub> MSCs.<sup>[22b]</sup> This section reviews the reported PSC modification procedures, classifying them according to the prevalent modification strategy, without referring to their applications which will be reviewed in the next section 3.

#### 2.4.1. Doping

Doping is a widely used strategy to tune their electronic structure for visible light photo conversion, by incorporation of heteroatoms into the lattice of targeted PSC materials. The main role of doping is to narrow the bandgap of wide bandgap semiconductors, so that the range of wavelength absorption can be extended towards the red. Taking TiO<sub>2</sub> as an example, **Scheme 16** shows three possibilities of band structure modification. The options include (a) a downward shift of conduction band minimum (CBM), (b) an upward shift of valence band maximum (VBM) and (c) impurity states in the band gap. In doping, the CBM of materials should be higher than the potential level of designated reduction reaction, and/or the VBM should be lower than the potential level of designated oxidation reaction so that the expected photocatalytic reaction can still take place after modification of the PSC electronic properties.<sup>[80]</sup> Moreover, the induced impurity states should be shallow so that photoexcited carriers can transfer to surface reactive sites within their lifetime. In the particular case of PSCs doping, procedures should accomplish both, the modification of the electronic band structure and preservation of the porous single crystalline structure. Both requirements can be difficult to meet simultaneously for many anion doping routines (especially solution reactions) due to the disturbance of dopants on the crystal growth.



**Scheme 16.** Possible strategies for band gap narrowing to achieve visible-light excitation with downward shift of CBM (a), upward shift of VBM (b), and impurity intraband states (c).

Reproduced with permission.<sup>[80]</sup> Copyright (2014) American Chemical Society.

Due to relatively large band gap (3-3.2 eV for various phases), TiO<sub>2</sub> only absorbs ultraviolet light. Several metal elements have been doped in TiO<sub>2</sub> PSCs by simple addition of metal salts, for example of Zn or Nb, to the solution submitted to hydrothermal reactions in TiO<sub>2</sub> synthesis.<sup>[81]</sup> Compared to metal doping, non-metal doping for TiO<sub>2</sub> PSCs is more difficult to be achieved by in-site wet methods, since non-metallic anions employed as dopant elements can influence nucleation and growth of well-faceted crystals in solution synthesis. For this reason, studies regarding non-metal doping for TiO<sub>2</sub> PSCs are scarce, except F<sup>-</sup> doping in which F<sup>-</sup> is acting simultaneously as doping source and morphology controlling reagent. F doping in TiO<sub>2</sub> PSCs can be achieved during the hydrothermal synthesis, without post calcination or alkaline rinsing.<sup>[82]</sup> For example, NH<sub>4</sub>F has been used to dope rutile TiO<sub>2</sub> PSCs by hydrothermal synthesis.<sup>[4c]</sup> In the doping, F<sup>-</sup> ions entered into the surface lattice of TiO<sub>2-x</sub> by substituting oxygen vacancies. For two Ti<sup>3+</sup> ions around an oxygen vacancy, one becomes oxidized to Ti<sup>4+</sup> by binding to F and the other Ti<sup>3+</sup> is still maintained, leading to a local polarization around F-color center. As a result, an upwards bending of the Ti<sup>3+</sup> impurity level occurs, increasing the reduction potential of the electrons.<sup>[83]</sup>

Using TiX (X = N, C, S, or other non-metal elements) as the only precursor, Liu et al have developed a general method to prepare doped-TiO<sub>2</sub> crystals with well-developed facets.<sup>[79]</sup>



The TiX dissolution can be used to achieve the in-site doping of TiO<sub>2</sub> PSCs, since Ti-X linkages are partially preserved in the liquid phase and can participate in the heterogeneous nucleation on templates.<sup>[84]</sup>

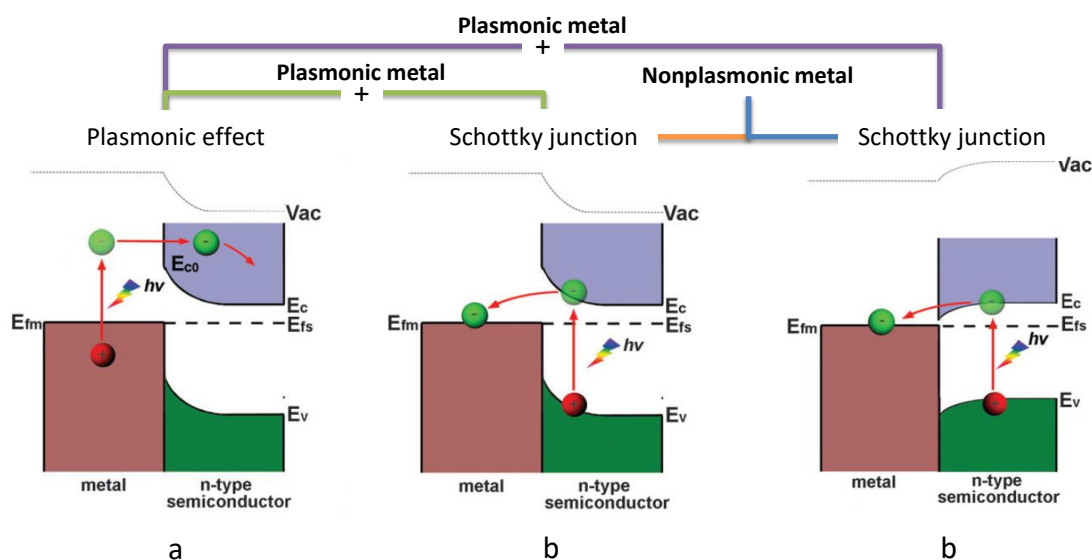
Oxygen vacancy accompanied by the corresponding metal ions with reduced-coordination number is equivalent to doping. This doping strategy is mainly involved in TiO<sub>2</sub> PSC preparation. By high-temperature annealing, oxygen vacancies could be generated in TiO<sub>2</sub> PSCs prepared by the Snaith's method.<sup>[15c]</sup> As the annealing temperature increases, oxygen vacancies are produced, leading to the concomitant reduction of Ti<sup>4+</sup> to Ti<sup>3+</sup> at the vacancy sites. Oxygen vacancies could be enhanced at low oxygen partial pressures.

For other PSC semiconductors, metal doping is also easily achieved by adding metal dopants in the synthesis solution, for example, Er doping in Bi<sub>2</sub>O<sub>3</sub><sup>[16f]</sup> and Zn doping in Fe<sub>2</sub>O<sub>3</sub>.<sup>[85]</sup> In addition, the PSCs prepared by the ion exchange strategy can be doped during their formation process without additional dopants. The percentage of doping can be controlled by adjusting the degree of ion exchange. Theoretically, all the PSCs prepared by ion exchange can be doped during the formation process, as for example Cd-ZnS, Cd-ZnSe, Cr-CeO, N-La<sub>2</sub>Ti<sub>2</sub>O<sub>7</sub>, N-TiO<sub>2</sub>, N-Ta<sub>2</sub>O<sub>5</sub> etc. (see Section 2.3.6). Cation exchange doping carried out at low temperature is generally easier than anion-exchange doping that requires high temperature to occur. Cation doping can generally be performed similarly to the anion doping discussed above during hydrothermal synthesis. The reason is that anion dopants (for example N, C, S etc.) rarely exist as isolated species, but in complex forms (for instance as oxyanions NO<sub>3</sub><sup>-</sup>, CO<sub>3</sub><sup>2-</sup>, SO<sub>4</sub><sup>2-</sup> etc.), which lead to the requirement for extra energy to break the bonds of the complex anions in the doping process.

#### 2.4.2 Loading of noble metal NPs

The positive influence on the photocatalytic activity observed by the presence of noble metal NPs is mainly attributed to a combination of three effects, namely, catalytic activity, plasmonic resonance and Schottky junction (**Scheme 17**). These three effects can function together or separately, depending on the metal used and the excitation wavelength.<sup>[86]</sup> Au and Ag are two noble metals exhibiting strong plasmonic resonance absorption band. When the frequency of photons matches the frequency of free electron oscillation on the metal surface, injection of hot electrons into the semiconductor conduction band can occur. Other possible plasmonic effect is electromagnetic field on the metal NP increasing the electron-hole pair separation on the semiconductor. Also, resonant photon-scattering mediated enhancement of light absorption can contribute to the improvement of the photocatalytic performance of the semiconductor<sup>[86-87]</sup> (Scheme 17 a). Visible or near-infrared light can excite Au and Ag NPs depending on their size and shape to produce the plasmonic effect. However, other noble metals (for example, Pt) have weak or no plasmonic effect in the visible region, so the catalytic activity or the Schottky junction would play in this case also an important role in the enhancement of the photocatalytic activity. When the metal is deposited on the surface of an n-type semiconductor with slightly higher Fermi level, the Fermi level of the semiconductor will equilibrate with that of the metal, and a space charge layer will be generated, leading to the upwards band bending, on the side of the semiconductor, and resulting in the formation of a Schottky barrier.<sup>[88]</sup> The in-built electric field in the interfacial layer will drive photogenerated electrons migration. With continuous irradiation, a large number of photoexcited electrons are accumulated in the CB of semiconductor to form “hot electrons”, which can inject into the metal promoting photocatalytic reduction (Scheme 17 b). When the metal is in contact with an n-type semiconductor with a slightly lower Fermi level, downward band bending occurs. The in-built electric field in space charge layer will drive photogenerated electrons transfer towards the metal to promote the separation of hole-electron pairs in semiconductor (Scheme 17 c). Usually, Schottky junction appears when metal and

semiconductor touch each other, while plasmonic resonance effect can only be observed for some metals, depending on the metal particle size and morphology. The plasma effect is also influenced by incident light wavelength and surrounding media. The catalytic activity refers to the ability of the metal NP to transfer electrons and holes to the substrate, promoting on it chemical transformations.



**Scheme 17.** (a) Charge migration driven by the plasmonic hot carrier effect, (b) Schottky junction between metal and n-type semiconductor. Reproduced with permission.<sup>[86]</sup> Copyright (2015) Royal Society of Chemistry.

Upon solar irradiation that includes some UV light, plasmonic metals loaded on semiconductors can simultaneously play several roles as visible light harvester due to the plasmonic resonance, as promoters of efficient charge separation due to Schottky junction and as co-catalysts promoting charge transfer to substrates. For example, Ag NPs were loaded on ZnO hierarchical microspheres composed of PSC nanosheets by liquid-phase precipitation,<sup>[89]</sup> and on rutile TiO<sub>2</sub> PSC nanorods by photo-reduction,<sup>[90]</sup> observing in both cases on obvious enhancement of the photocatalytic ability. It could happen that one of the roles prevails over the others. Thus, it has been reported that when using visible light irradiation and Au NPs, the

plasmonic resonance plays the major role in the photoconversion enhancement for SrTiO<sub>3</sub> PSCs because only the electrons in Au NPs can be excited under these conditions.<sup>[10]</sup>

In photoreduction reactions (for example H<sub>2</sub> generation and CO<sub>2</sub> reduction), Pt NPs often act as cocatalyst to boost the separation of the photogenerated electron–hole pairs via Schottky junction based on the very downward position of the Fermi energy level in Pt and the ability of this noble metal to split and form H-H bonds.<sup>[91]</sup> Rutile TiO<sub>2</sub> PSCs and TaON PSC microspheres have been modified by photo-deposition with Pt NPs observing an improvement in the photocatalytic H<sub>2</sub> generation and photocatalytic conversion of CO<sub>2</sub>.<sup>[4b, 73]</sup> Note that in the case of Pt/TiO<sub>2</sub> PSCs, most Pt NPs have been found to be located within the pores where reduction of Pt<sup>VI</sup> by photoexcited electrons occurs, suggesting that the photoexcited carriers are mainly consumed by the reactants inside or near the pore walls. It seems that long-range electron migration through the interconnected architecture of PSC is not necessary in photocatalysis with PSC powders and each pore appears to exhibit photocatalytic activity. Accordingly, for photocatalysis charge carriers can migrate shorter distances, just from the inner of particles to the outer surface. We will come back to this issue in the section dealing with applications of semiconductor PSCs.

In other more elaborated example, Bi<sub>20</sub>TiO<sub>32</sub> PSC structures with a high degree of periodicity over large domains have been modified by both Ag and AgCl to form a plasmonic Z-scheme system.<sup>[92]</sup> Upon visible light irradiation, Bi<sub>20</sub>TiO<sub>32</sub> nanosheets are excited to produce photogenerated electrons and holes. Due to plasmonic resonance effect, Ag NPs also absorb visible light to generate electrons and holes. The plasmon-induced electrons in Ag migrate to CB of AgCl to reduce oxygen, while the holes on Ag recombine with photogenerated conduction band electrons of Bi<sub>20</sub>TiO<sub>32</sub>. In this way, so that the holes located at VB of Bi<sub>20</sub>TiO<sub>32</sub> are unbalanced and are capable to oxidize organic substances.

#### 2.4.3. Semiconductor-semiconductor heterojunction

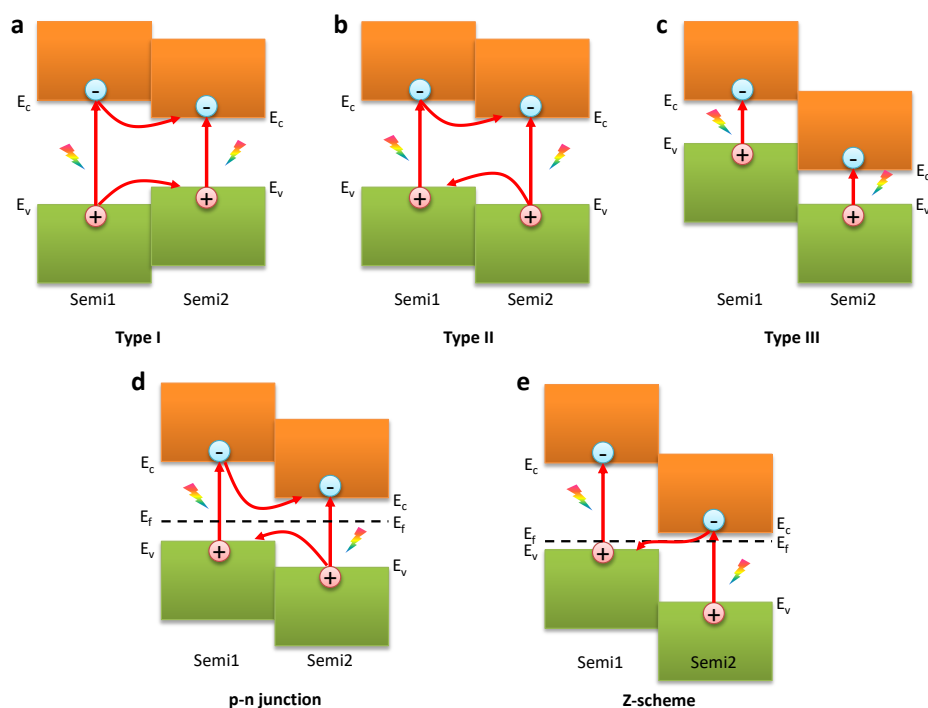
Different semiconductors may have different light absorption ranges and various redox potentials. Appropriate combination of two or more semiconductors in intimate contact (junction) can produce composite materials with optimal photoconversion performance. The relative energy levels of semiconductor1 (semi1) and semiconductor2 (semi2) of the heterojunction can serve to classify it as type I (straddling alignment), type II (staggered alignment), type III (broken alignment) and extended type II Z-scheme (**Scheme 18**). In type I, the electrons on VBM of both semiconductors are excited, and both of them undergo photoinduced charge separation in electrons and holes in semi1 with wide bandgap will transfer to semi2 with narrower gap. Although these electrons and holes can easily recombine in semi2, their transfer rates from semi1 to semi2 are different, resulting in the temporal separation of them (Scheme 18 a). In one example belonging to the type I mechanism, elemental S NPs were used to modify rutile PSCs by precipitation.<sup>[22c]</sup> In the case of type II, both the VBM and CBM of semi1 are higher and in equilibrium with those of semi2. After the electrons in VBM of both semiconductors are excited, the photoexcited electrons in the CBM of semi1 move to the CBM of semi2 and the photogenerated holes in the VBM of semi2 move to the VBM of semi1, resulting in the physical separation of photogenerated  $e^-/h^+$  pairs, each charge carrier in a different semiconductor (Scheme 18 b). In type III, the difference between the Fermi levels of the two semiconductors is so large that their band gaps cannot overlap, and there is no electron transfer occurring between them after photoexcitation (Scheme 18 c). In fact, the type III is not suitable to improve photoconversion.

For type II, when a p-type semiconductor and an n-type semiconductor are connected, a *p-n heterojunction* with a better photocatalytic performance can be obtained due to the larger driving force for charge transfer derived from the difference between the Fermi levels of the two semiconductors (Scheme 18 d). In one example, SnO<sub>2</sub> PSCs have been modified by photodeposition with an n-type conjugated organic polymer, polydiphenylbutadiyne (PDPB)

nanofibers to construct a PDPB/SnO<sub>2</sub> p-n junction.<sup>[93]</sup> Additionally, if the CBM of semi1 is close to the VBM of semi2 in equilibrium, the photoexcited electrons in the CBM of semi1 can be directly transferred to the VBM of semi2, then both the photogenerated holes in the VBM of semi1 and the excited electrons in the CBM of semi2 are physically separated and able to participate in independent complementary redox reactions. This charge carrier transfer is generally referred as the *Z-scheme* mechanism (Scheme 18 e), in which sometimes a conductor is employed as electron mediator between two semiconductors. Moreover, for the type II heterojunction, if incident light can only excite carriers in the semiconductor with the narrower bandgap, the excited electrons or holes could be injected into the CB or the VB of another semiconductor with wider bandgap leading to the effective separation of photogenerated e<sup>-</sup>/h<sup>+</sup> pairs in the first semiconductor. Then, the charge transfer follows a *sensitization* mechanism in photocatalytic reaction. As an example of sensitization mechanism, hexagon shaped ZnO PSC nanodisks with exposed {0001} facets were modified either by CdS quantum dots (QDs) via successive ionic layer adsorption and reaction (SILAR) process, or by CdSe QDs via chemical bath deposition (CBD) method, separately.<sup>[41]</sup> In addition, cobalt oxide was deposited on LaTiO<sub>2</sub>N (LTON) PSC to build a CoO<sub>x</sub>/LTON heterojunction. However, in this case the detailed mechanism for photogenerated carrier transfer has not been clarified possibly due to the complex composition of CoO<sub>x</sub> containing both CoO and Co<sub>3</sub>O<sub>4</sub>.<sup>[94]</sup> On the whole, in type I and type II systems (including p-n junction and sensitization), the redox capability of initial semiconductors is actually decreased; in Z-scheme, the maximum redox potentials of initial semiconductors are maintained, but the photoconversion efficiency is reduced to a half because the other half of energy is lost through the recombination of excited electrons in semi1 and excited holes in semi2 (Scheme 18 e).

All the semi1-semi2 PSC heterojunctions reported so far have been prepared by post-treatments starting with previously prepared PSCs. Thus, the construction of the

heterojunction does not affect the morphology and structure of the semiconductors when appropriate reaction conditions for the loading of the second semiconductors are selected.

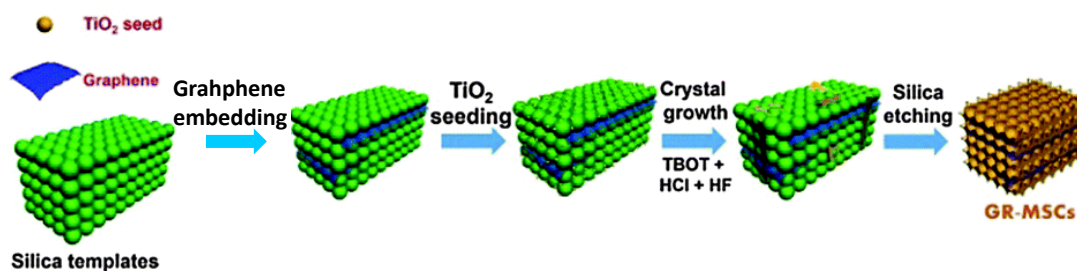


**Scheme 18.** Band diagrams illustrating the various possibilities in the formation of heterojunctions between semiconductor1 (semi1) and semiconductor2 (semi2): (a) Type I, (b) Type II, (c) Type III, (d) p-n junction and (e) Z-scheme.

#### 2.4.4. Other modifications

Carbon materials (such as graphene, carbon nanotubes and carbon fibers etc.) are often combined with semiconductors to improve the transfer of photogenerated electrons in photocatalytic reaction. This is mainly due to the high electrical conductivity of carbon materials together with the Schottky junction effect between carbon and semiconductor, enabling the separation and transfer of photogenerated  $e^-/h^+$  pairs in semiconductor. With graphene-embedded silica spheres as the hard template, a novel sandwiched graphene-modified  $\text{TiO}_2$  mesoporous single crystals (GR-MSCs) could be prepared by a hydrothermal

method (**Scheme 19**).<sup>[22b]</sup> Using TiO<sub>2</sub> mesocrystal/carbon nanotube composites as precursor prepared by low-temperature hydrothermal process, carbon nanotubes modified TiO<sub>2</sub> PSCs were produced by calcination of this composite over 400 °C.<sup>[95]</sup> In addition, carbon fibers modified TiN PSC nanoplates were prepared by an in-site nitridation of TiO<sub>2</sub>-carbon fiber composite;<sup>[72]</sup> reduced graphene oxide modified Zn<sub>0.5</sub>Cd<sub>0.5</sub>S PSC nanosheets have been synthesized by photoreduction of graphene oxide by Zn<sub>0.5</sub>Cd<sub>0.5</sub>S PSC nanosheets under visible light irradiation;<sup>[96]</sup> WO<sub>3</sub> PSC nanoflakes have been modified by carbon QDs via a simple immersion method.<sup>[38]</sup> In these modifications, besides enhancement of the photocatalytic activity due to more efficient migration of photogenerated carriers, it was proposed that carbon materials may also play an important role in improving light absorption due to their “black” color and by absorbing reactants near the active sites due to their large surface area.<sup>[86]</sup>



**Scheme 19.** Illustration of the growth pathways of sandwich structured GR-MSCs.

Reproduced with permission.<sup>[22b]</sup> Copyright (2015) Royal Society of Chemistry.

Similar to semiconductor sensitization, some organic dyes or metal complexes are also used to modify semiconductors. Then, the excited electrons in the lowest unoccupied molecular orbital (LUMO) or holes in the highest occupied molecular orbital (HOMO) of molecules could migrate to the CB or the VB of connected semiconductor promoting the corresponding reduction or oxidization reaction on the semiconductor upon long wavelength irradiation.

[Ru(bpy)<sub>3</sub>]<sup>2+</sup> (bpy: 2,2'-bipyridine) has been used to modify hollow Co<sub>3</sub>O<sub>4</sub> PSC microspheres



consisting of nanosheets by donating photogenerated holes to  $\text{Co}_3\text{O}_4$ , with persulfate acting as the sacrificial electron acceptor.<sup>[54a]</sup>

Surface amorphization (or surface hydrogenation) is another effective modification method applied in photocatalysis. Anatase  $\text{TiO}_2$  microspheres consisting PSC units have been modified by surface hydrogenation treatment.<sup>[9b]</sup> By treating the materials in high-pressure hydrogen gas for a period of time, structural disorder in a shallow thickness of only a few nanometers of the PSC can be obtained. Besides surface disorder, H-doping associated with Ti-OH and Ti-H bonds, and/or oxygen vacancies and  $\text{Ti}^{3+}$  defects are also possibly formed, depending on the detailed preparation conditions. These structural changes lead to an upward shift of VBM and, consequently, smaller band gap resulting in increased light absorption,<sup>[97]</sup> although the detailed mechanism for improving photocatalytic activity is still under discussion.<sup>[98]</sup> Such surface disorder treatment for  $\text{TiO}_2$  PSCs may be further extended to more general reduction routines just like the ones used for common  $\text{TiO}_2$  materials. Examples include chemical reduction,<sup>[99]</sup> electrochemical reduction,<sup>[100]</sup> hydrogen plasma treatment<sup>[97b]</sup> etc. forming defect rich structures similar to “black  $\text{TiO}_2$ ”<sup>[98]</sup> without notably changing in these modifications their initial PSC morphologies.

On the whole, modification of PSCs mainly depends on the development of semiconductor modification technologies. However, two restrictions from common semiconductors exist in PSCs according to the basic features of PSCs (Section 2.2): (1) modification should not deteriorate the single crystalline nature of PSCs, specifically, it should not break nucleation and growth of new crystals, and/or destroy the previously formed crystals; (2) modification should not alter the formation of pores, specifically, it should not interfere the assembly of crystals on templates, and/or destroy the self-assembly and self-etching of crystals in the formation of pores. In current semiconductor modifying procedures, aside from wet-doping, most modifications consist on post-treatments, which only lead to slight change of structure and morphology. Consequently, most post-modifying treatments for common semiconductors

can also be used for PSCs. However, the number of studies focused on modifying PSCs is relatively small, possibly due to the short time elapsed since the first report on PSC synthesis in 2002. Such shortage provides large opportunities to develop new procedures for PSC modification that eventually could lead to highly active semiconductors for efficient utilization of solar energy.

### 3. Applications.

PSCs have been successfully employed in different applications such as photocatalysis, solar cells, gas sensors, Li batteries, among others. The solar cells working principles has many common elementary steps with photocatalysis, including light harvesting, charge separation and charge transport to an interface, being the main difference the substrate transformation upon redox reaction, in the case of photocatalysis, while charge collection at suitable electrodes through interparticle charge migration take place in solar cells. In both cases, the PSCs properties above-mentioned (high surface area, high crystallinity, lattice continuity, tunable pore size and shape, etc.) should provide a higher performance to these materials than that of other polycrystalline non-porous systems. In the following sections some relevant examples will be commented highlighting the performance improvement when PSCs materials are used in photocatalysis and photovoltaics applications.

#### 3.1 Photocatalytic environmental remediation.

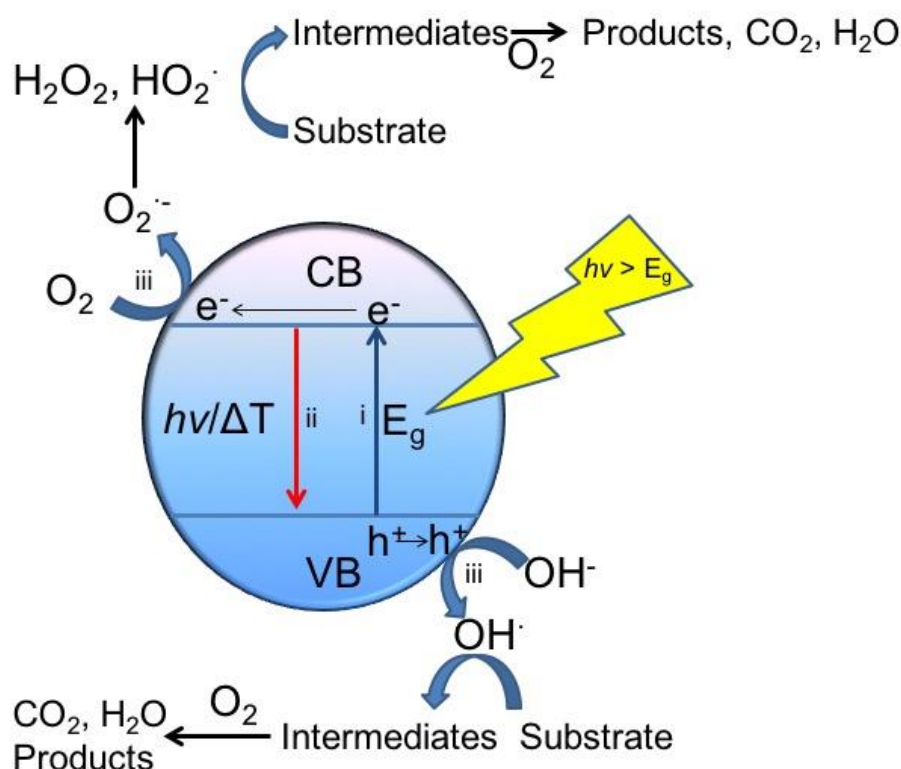
The consumption of fresh water is continuously increasing not only for domestic use, but also, due to the increase of the industrial activities in different sectors such as food, chemicals, microelectronics, pharmaceutical, etc. As consequence, waste water from both domestic consumption and industrial sectors is very frequently contaminated with toxic organic and/or inorganic compounds. In addition, the social concern on emerging contaminants having potent

biological effect at very low concentrations has motivated more restrictive regulations that require the implementation of novel waste water treatment methods. An ideal water treatment process must mineralize all the toxic organic species, being cost-effective and environmentally friendly. \*1

Among the various possible alternative methodologies for waste water treatment, heterogeneous photocatalysis is one that has attracted considerable attention since several decades. In principle, heterogeneous photocatalysis can affect pollutant degradation in aerated water without the need of chemicals such as  $\text{H}_2\text{O}_2$ ,  $\text{O}_3$ , or other oxidizing reagents. Moreover, the photocatalyst is typically a robust material that can be reused and the light source is not limited to UV lamps, but in some cases photocatalysis can be promoted by natural solar light. Photocatalytic pollutant degradation in aqueous media is almost universally based on the generation of hydroxyl radicals ( $\text{OH}\cdot$ ), since  $\text{OH}\cdot$  has a high oxidizing potential (2.80 eV), and can be generated both from oxygen (reduction) and water (oxidation) by photocatalysts activated with UV-Vis light. In a typical semiconductor, the energy gap between the conduction (CB) and the valence band (VB), is in the order of few eV (1.5 - 4 eV). Photons with sufficient energy promote electrons from the VB to the CB. In n-type semiconductors such as  $\text{TiO}_2$ , CB electrons can move through the semiconductor particle. The resulting vacancies, or holes, in the now partially filled VB will also move, although slower. The photogenerated electron-hole pairs can subsequently be involved in two main reactions: (1) undesirable electron/hole recombination, dissipating the photon energy as heat or luminescence, or (2) reaction with different species on the semiconductor interphase giving rise to oxidation and reduction reactions (**Scheme 20**).

For efficient photocatalytic pollutant degradation in water or humid atmosphere, the redox potential of photogenerated VB holes must be sufficiently positive to oxidize water, generating the  $\text{OH}\cdot$  radical, and the redox potential of the photogenerated CB electron must be negative enough to be able to reduce the adsorbed oxygen to superoxide radical anion ( $\text{O}_2^{\cdot-}$ ). Scheme 20

illustrates the step of charge separation (i), the recombination process of the electron-hole pair (ii), and some of the subsequent reactions on the semiconductor surface (iii).



**Scheme 20.** Elementary steps of photocatalytic pollutant degradation: i) Photon absorption and charge separation, ii) charge recombination, and iii) surface oxidation and reduction leading to the generation of reactive oxygen species.

There is a large variety of commercially available semiconducting materials such as  $\text{TiO}_2$ ,  $\text{ZnO}$ ,  $\text{ZnS}$ ,  $\text{CdS}$ ,  $\text{Fe}_2\text{O}_3$ ,  $\text{WO}_3$ , etc. suitable for photocatalytic applications<sup>[101]</sup>. However, only a few of them have been found suitable for environmental remediation, due to thermodynamic and stability issues. While low bandgap energy semiconductors ( $< 2.3$  eV) are preferred for solar light activation, most of this type of semiconductors does not reach the redox potential requirements for the oxidation/reduction pairs involved in the aerobic oxidation in water or humid ambient process. Moreover, low bandgap semiconductors, especially metal chalcogenides as  $\text{CdS}$  and  $\text{CdSe}$ , usually suffer serious stability problems.

Photocatalysts exhibiting large surface area and high crystallinity are the most preferred since, on one hand, they provide numerous active sites, and, on the other hand, the charge transport is faster and charge separation is more efficient in highly crystalline materials, rather than for the amorphous ones, where defects can act as charge trapping/recombination sites. Moreover, although polycrystalline materials may present high charge mobility in the intracrystalline domains, grain boundaries introduce high resistance to charge mobility and the surface sites can act as  $e^-/h^+$  recombination centers. In addition, typical synthetic procedures employed for semiconductor photocatalysts containing large specific surface area generally diminish their crystallinity. For this reason, the use as photocatalysts of PSCs semiconductors exhibiting simultaneously large surface area and high crystallinity is very advantageous to improve the photocatalytic activity in semiconductors. Therefore, as commented in Section 2, many synthetic protocols based on templates, hydrothermal synthesis, sol-gel, etc. have recently been developed in order to prepare photocatalysts with single crystal-like structure and large surface area. Moreover, the different preparation procedures influence other parameters affecting considerably their photocatalytic activity, such as crystal phase and preferential facet exposure. Doping and incorporation of co-catalysts are additional tools to further enhance the photocatalytic activity of some PSC semiconductors.

Typically, colorful organic dyes have been used as model pollutants for evaluation of the photocatalytic activity, since their concentration at any time can be very easily followed by UV-Vis absorption spectroscopy. **Figure 10** presents some of the organic dyes that have been most frequently used as models in photocatalytic degradation experiments to determine PSC activity. Besides dyes, other suitable model molecules are phenols and alcohols, particularly the latter for gas phase photocatalytic studies.

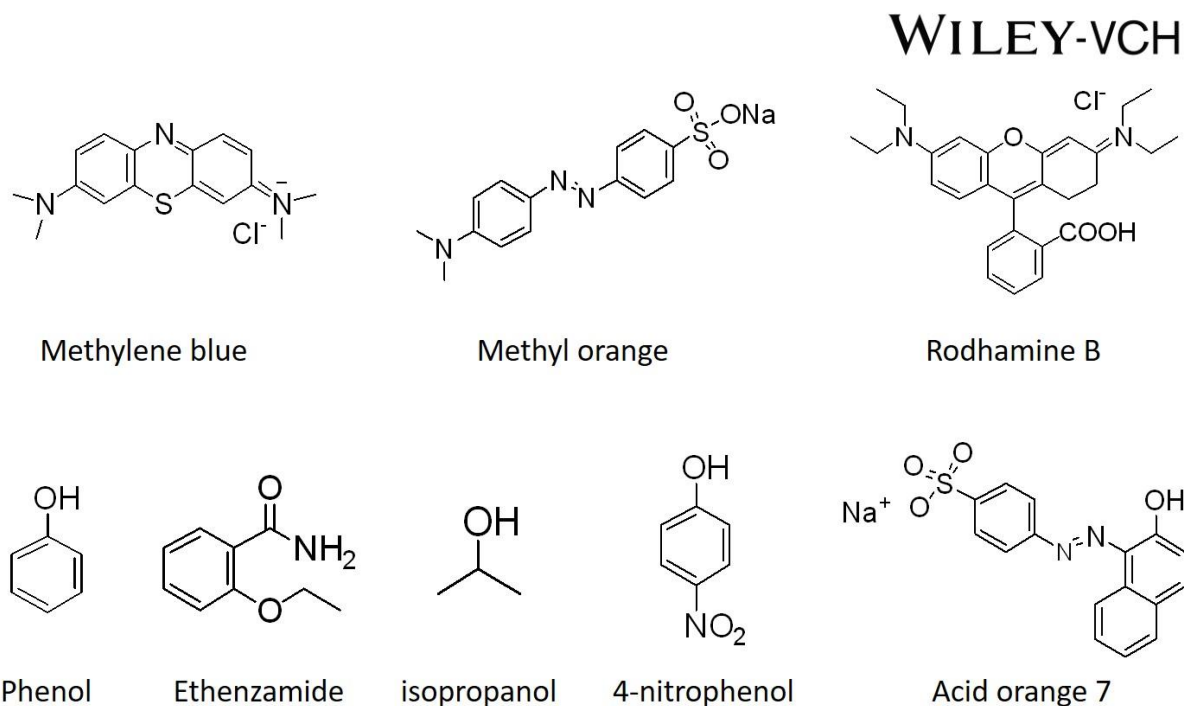


**Figure 10.** Chemical structures of the most frequently used dyes and organic probe molecules to evaluate the photocatalytic activity of PSC semiconductors in pollutant degradation.

### 3.1.1 PSC crystallinity influence on the photocatalytic activity.

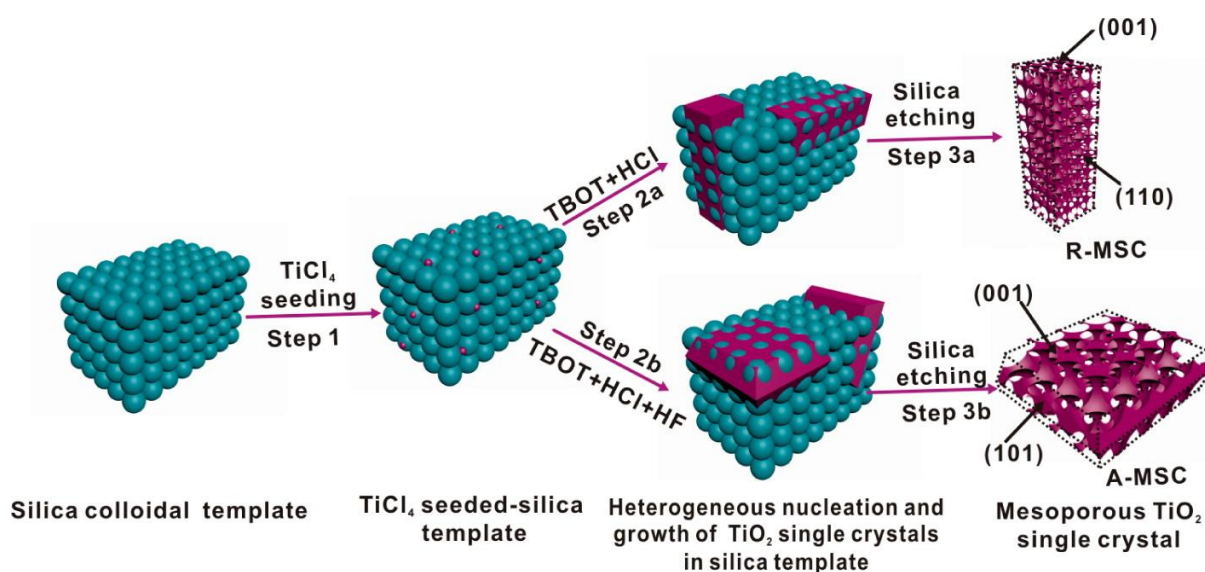
TiO<sub>2</sub> has been the most widely used photocatalyst since the pioneering Fujishima and Honda report.<sup>[102]</sup> The photocatalytic properties of TiO<sub>2</sub> derive from the generation of positive holes and electrons upon irradiation by UV light (anatase bandgap 3.3 eV) and subsequent formation of the primary reactive oxygen species OH· and O<sub>2</sub><sup>·-</sup> followed by the generation of secondary reactive oxygen species upon subsequent protonation and redox processes.

As commented in section 2.3, one of the simplest methods to prepare TiO<sub>2</sub> MSCs is based on the use of either soft or hard templates, such as the polymeric surfactants P123 and F127 or the ordered mesoporous silicas MCM-41, SBA-15, KIT-6 or FDU-12, respectively. Importantly, the template selection can strongly influence the morphological characteristics of the as-prepared TiO<sub>2</sub>, affecting, therefore, their photocatalytic properties. In a similar way, it has been reported that the reaction temperature and the TiO<sub>2</sub> precursors can tune the crystal phases and

structure of mesoporous  $\text{TiO}_2$  using SBA-15 as external hard template of internal  $\text{TiO}_2$  guests.<sup>[103]</sup> Thus, porous monocrystalline rutile  $\text{TiO}_2$  was obtained, even at low temperatures ( $\approx 50\text{ }^\circ\text{C}$ ), when titanium nitrate was used as precursor to form  $\text{TiO}_2$  PSC inside SBA-15. In contrast porous polycrystalline anatase  $\text{TiO}_2$  is obtained inside SBA-15 using titanium chloride as precursor, increasing, however, crystallinity with temperature in the range of 300 to 600  $^\circ\text{C}$ . The authors point out that the presence of  $\text{NO}_3^-$  anions induces crystallization of amorphous  $\text{TiO}_2$  to rutile as opposed to  $\text{Cl}^-$  that renders anatase upon thermal treatment. Moreover, the titanium oxynitrate gives rise to long Ti-O-Ti chains which ensure a high precursor loading inside the SBA-15 template, forming large  $\text{TiO}_2$  crystals. Instead, the hydrolysate of titanium chloride promotes shorter Ti-O-Ti chains, leading to NP formation inside the silica pores. PSC rutile was found more suitable than the nanoparticulate anatase analogue prepared from titanium chloride for  $\text{Li}^+$  insertion in battery applications. One of the missing data in that study was, however, the photocatalytic activity of the single crystal  $\text{TiO}_2$  rutile, in comparison with the high photocatalytic activity towards methylene blue decomposition of polycrystalline anatase  $\text{TiO}_2$ , achieving almost complete bleaching in 3 h. A comparison of the photocatalytic activity between polycrystalline anatase and PSC rutile would have illustrated how easily the photocatalytic performance changes depending on the  $\text{TiO}_2$  precursor, even if the same preparation protocol is used.<sup>[103]</sup>

Continuing with examples of how easily different  $\text{TiO}_2$  phases are obtained even following the same procedure, rutile PSC nanorods of tunable size and single crystal anatase nanosheets with preferential  $\{001\}$  facet were prepared depending on the precursor concentration, seed density and temperature.<sup>[104]</sup> In this example, a silica template was seeded with  $\text{TiCl}_4$  at different concentrations. Then, the different rutile and anatase structures were grown by a hydrothermal method using HCl or HCl/HF solutions at temperatures between 150 and 200  $^\circ\text{C}$  for 12 h. The hydrohalic acid solutions were chosen as the reaction media since they have been previously reported as morphology controlling agents. Thus,  $\text{TiO}_2$  forms  $\{001\}$  oriented tetragonal rutile

nanorods at high HCl concentration, while a small amount of HF in the HCl solution acts as capping agent, evolving the TiO<sub>2</sub> seeds to anatase nanosheets with preferential {0 0 1} facet orientation. In addition to phase control, the size and shape were also tuned with the seed concentration. In general, the size of the TiO<sub>2</sub> structures decreases with seeding concentration increase. **Scheme 21** illustrates the conditions leading PSC rutile nanorods or single-crystal anatase nanosheets.



**Scheme 21.** Illustration of the growth pathways of PSC rutile nanorods or single-crystal

anatase nanosheets. Reproduced with permission.<sup>[104]</sup> Copyright (2013) American Chemical Society.

On the other hand, rutile branched nanorods and a mixture of anatase olive-shaped and mesoporous nanosheets were obtained at low seed concentration, while smaller rutile nanorods and anatase nanosheets were obtained at higher seed concentrations. Finally, as complementary to seed concentration, the hydrothermal reaction temperature was found also able to vary the sizes of the TiO<sub>2</sub> particles.<sup>[104]</sup> These rutile and anatase TiO<sub>2</sub> materials were tested in the photocatalytic methyl orange decolorization. The photocatalytic experiments revealed that the degradation efficiency was 90 % for rutile structures and 97 % for the anatase ones upon irradiation with a 300 W Xe lamp for 3 h. The authors proposed that these results are a

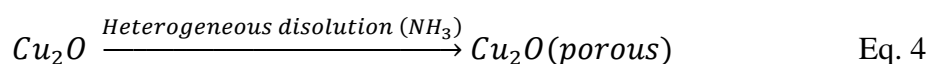
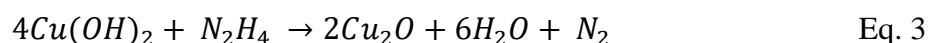
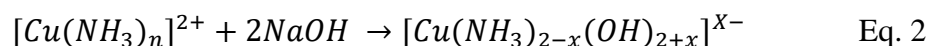
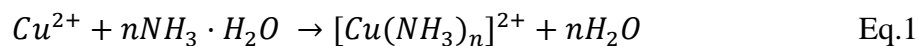


consequence of the combination of several factors including higher Fermi level, longer photoexcited exciton lifetime and higher electron mobility in anatase materials respect to the rutile ones. In general, it was found that rutile crystals were more suitable for reductive photocatalytic applications, such as H<sub>2</sub> evolution, while anatase ones exhibit better oxidative photocatalytic activity. The authors attributed the origin of this different photocatalytic behavior to the different exposed crystal facets of each structure.<sup>[104]</sup>

The search for optimized structures capable to provide superior photocatalytic activity has led to develop sophisticated multi-step synthetic procedures. In one of these reports, the precipitation of radially aligned TiO<sub>2</sub> nanowires on polyester fibers was achieved through: surface roughening, sol-gel TiO<sub>2</sub> seeding, hydrogen titanate nanobelts precipitation and acid treatment with sulfuric acid.<sup>[105]</sup> Following this multi-step synthetic procedure both mesoporous anatase TiO<sub>2</sub> nanowires and single-crystalline rutile TiO<sub>2</sub> nanorods were obtained accompanied by some unreacted nanobelts. This mix of 1D nanostructures and phase junctions were found responsible for an excellent photocatalytic activity for degradation of Rhodamine B in water, toluene vapor in air and also for antibacterial activity against *Escherichia coli* and *Staphylococcus epidermis* under UV light irradiation (365 nm).<sup>[105]</sup> Overall, the general outcome of this area are methodologies to prepare the wanted TiO<sub>2</sub> PSC materials and clear evidence that they are the best option among all possible alternative TiO<sub>2</sub> materials for pollutant degradation. A deeper understanding of the factors that influence this activity and their interplay is still needed.

Similarly, to the abundant examples reporting the excellent photocatalytic activity of monocrystalline TiO<sub>2</sub> towards pollutant degradation, there are also numerous examples showing that the same conclusion is valid for other semiconducting metal oxides. Thus, Xu et al. reported the preparation of single crystal of porous Cu<sub>2</sub>O spheres obtained by heterogeneous dissolution of freshly formed single crystalline Cu<sub>2</sub>O spheres.<sup>[106]</sup> In this way, Cu<sub>2</sub>O PSC spheres of approximately 100 nm were prepared following **Equations 1 - 4**.<sup>[106]</sup> The fine control

of  $\text{Cu}^{2+}:\text{NH}_3$  and  $\text{Cu}^{2+}:\text{OH}^-$  molar ratios in Equation 1 and 2 and the exact amount of  $\text{NH}_3$  employed for the heterogeneous dissolution were found key to achieve the final  $\text{Cu}_2\text{O}$  morphology.



These porous single crystal  $\text{Cu}_2\text{O}$  spheres have demonstrated remarkable photocatalytic activity towards methyl orange photodegradation under visible light irradiation, even better than that of Degussa P25  $\text{TiO}_2$  under identical conditions.<sup>[106]</sup>

The role of organic additives in the synthesis of  $\beta\text{-Ga}_2\text{O}_3$  MSC with different nanostructures and their influence on the photocatalytic degradation of Rhodamine B upon UV light irradiation has been also studied.<sup>[107]</sup> Thus, mesoporous PSC  $\beta\text{-Ga}_2\text{O}_3$  blocks, spindles and rods have been synthesized using a hydrothermal process employing the cationic CTAB, anionic (sodium dodecylsulfate (SDS)) and non-ionic PEG-200 additives, respectively. The different nanostructures obtained in each case not only presented different surface area and pore size, but also different band gap, being 4.36, 4.27 and 4.15 eV for rods, spindles and blocks, respectively. The photocatalytic degradation of Rhodamine B upon UV light revealed that  $\beta\text{-Ga}_2\text{O}_3$  nanorods were the most active material compared with spindles and block nanostructures, and all  $\beta\text{-Ga}_2\text{O}_3$  PSC materials presented better activity than bulk  $\beta\text{-Ga}_2\text{O}_3$  and  $\text{TiO}_2$  Degussa P25. The improved photocatalytic activity of the  $\beta\text{-Ga}_2\text{O}_3$  MSC nanorods has been attributed to their higher surface area and higher band gap. The increased band gap was attributed to both VB and CB shift, becoming more oxidative and reductive, respectively.<sup>[107]</sup> It should be commented, however, that rather than the band gap the important factor is the relative potential of CB and

VB respect to  $O_2$  and  $H_2O$  that are the species assumed to quench CB electrons and VB holes, respectively, forming superoxide anion ( $O_2^{\cdot-}$ ) and hydroxyl ( $\cdot OH$ ) radicals, respectively. The higher ability to generate reactive oxygen species in nanorods respect to other nanostructures should have been proved on firm grounds by direct quantification of these species.

In a different approach, selective photodegradation of positively charged organic molecules was achieved using 2D ZnO MSC nanosheets with exposed (0 0 0 1) polar facets as photocatalysts. This material was prepared by fine control of the infiltration speed of polymeric colloids in EG-capped ZnO NPs.<sup>[15a]</sup> That is, ethanoic solutions of EG-capped ZnO NPs and monodispersed polymeric colloids were mixed and the composite filtered slowly and dried at 40 °C for self-assembling into a layered structure. Finally, the composite layered structure was calcined up to 450 °C in air in order to obtain the final 2D ZnO MSC (see Scheme 8 in section 2.3.1). The EG capped ZnO is used as the 2D PSC ZnO source, while the polymeric colloids presented the dual role of porosity generation and (0 0 0 1) polar facets growth within the mesopores.<sup>[15a]</sup> This structure enhances the selective adsorption of organic molecules as consequence of the mesoporosity and the exposed (0 0 0 1) polar facets. Thus, the 2D ZnO MSCs are highly active and selective for photodegradation of positively charged molecules such as Rhodamine B. On the contrary, lower activity was achieved for negatively charged or neutral molecules, such as methyl orange and phenol, respectively. The authors attributed this improved selectivity towards positively charged organic molecules to the porous structure and the {0 0 0 1} polar facets within the pores present in ZnO MSCs which enhance the selective adsorption of adsorbates depending on their Coulombic charge.<sup>[15a]</sup> This selectivity in photocatalysis is remarkable, since most photocatalytic degradation mechanism are based on the generation of reactive oxygen species that are rather unselective and degrade organics in a general manner. It would have been of interest to address why in the present case the role of reactive oxygen species is secondary.

Other metal oxide that has demonstrated to be photocatalytically very active in pollutant degradation is  $\text{Fe}_2\text{O}_3$ . One of the main advantages of this n-type semiconductor material is its narrow 2.2 eV band gap, which makes it responsive in the visible region. Other advantageous properties of  $\text{Fe}_2\text{O}_3$  are its stability in aqueous media at neutral or basic pH values and its magnetic properties that allow efficient separation and reusability. However, an ideal photocatalyst should also exhibit large specific surface area, porosity and high crystallinity. Overcoming these limitations, the synthesis of 1D  $\text{Fe}_2\text{O}_3$  nanorods and spindle-like nanostructures has been reported.<sup>[108]</sup> Depending on the iron precursor,  $\text{FeCl}_3 \cdot 6\text{H}_2\text{O}$  or  $\text{Fe}(\text{NO}_3)_3 \cdot 9\text{H}_2\text{O}$ , nanorods or spindle-like nanostructures can be obtained, respectively, by hydrolysis of these iron precursors in the presence of urea. The photocatalytic activity towards Rhodamine B degradation of these  $\text{Fe}_2\text{O}_3$  materials towards Rhodamine B degradation was tested upon irradiation of aqueous solutions of the synthesized 1D nanostructures with a 2 mW UV source ( $\lambda = 365 \text{ nm}$ ) for 165 min. The photocatalytic experiments showed higher activity for the nanorods than for the spindle-like nanostructures. The authors attributed the improved photocatalytic activity to the higher pore size distribution and specific surface area that  $\text{Fe}_2\text{O}_3$  nanorods present in comparison to the spindle-like nanostructures.<sup>[108]</sup> It is, however, unclear why if  $\text{Fe}_3\text{O}_4$  is responsive to visible light, irradiations were carried out in the UV region that is suited for broad bandgap semiconductors.

In a similar approach, single crystal  $\alpha\text{-Fe}_2\text{O}_3$  nanorods with void pores were synthesized and their photocatalytic activity towards methyl orange degradation studied as function of the preparation temperature.<sup>[109]</sup>  $\alpha\text{-FeOOH}$  nanorods were successfully obtained by hydrothermal synthesis using  $\text{FeCl}_3 \cdot 6 \text{H}_2\text{O}$ , NaOH and 1-*n*-butyl-3-methylimidazolium chloride ionic liquid as  $\alpha\text{-FeOOH}$  precursors. Porous single crystal  $\alpha\text{-Fe}_2\text{O}_3$  nanorods were subsequently obtained upon calcination at three different temperatures (523, 623 and 673 K). As it would be anticipated, the different calcination temperatures promoted distinctive changes in porosity and crystallinity, retaining the nanorod morphology. It was found that the higher the temperature,

the more crystalline the material is, although the specific surface area becomes lower. The photocatalytic activity for methyl orange degradation was tested upon irradiation with simulated sunlight at 1 sun for 60 min using  $\alpha$ -Fe<sub>2</sub>O<sub>3</sub> PSC nanorods prepared at different temperatures. The different  $\alpha$ -Fe<sub>2</sub>O<sub>3</sub> PSC nanorods presented different activity, being higher for the less crystalline nanorods with higher surface area that were prepared at lower temperatures. Therefore, the photocatalytic activity in this case seems to be exclusively dependent on the specific surface area, regardless the crystallization degree.<sup>[109]</sup> It would be important to understand the reasons why in this case defects do not play a detrimental role in the photocatalytic activity.

In a different example, hierarchical WO<sub>3</sub> flowers comprising PSC nanoplatelets exhibit visible light driven photocatalytic activity towards methylene blue degradation.<sup>[110]</sup> Hydrothermal treatment of the tungsten precursor with oxalic acid and urea in water/acetonitrile solution gave rise after 10 h at 180 °C to an ammonium tungsten peroxo oxalate hydrate compound. This tungsten oxalate was calcined at 500 °C for 2 h in order to obtain the final superstructure of hierarchical flower-like WO<sub>3</sub> consisting in PSC nanoplatelets. The absorption onset of this material was determined at approximately 477 nm. Based on this data, the photocatalytic activity for methylene blue was studied under visible light irradiation ( $\lambda > 420$  nm), the WO<sub>3</sub> superstructure showing better activity than TiO<sub>2</sub> Degussa P25 under visible light irradiation.<sup>[110]</sup> Among the visible light photocatalysts that have emerged recently in the literature, those based on Bi and metal oxides have attracted considerable attention due to their narrow band gap compared to metal oxides and to their longterm stability. Moreover, the number of compounds combining metal oxides and Bi increases considerably. This rise can be understood considering that different synthetic approaches employed for the preparation of Bi compounds generally result in different materials with distinctive properties. In one of the selected studies, bismuth nitrate, the triblock copolymer P123 as soft template, and ammonium metavanadate have been employed as precursors in the hydrothermal synthesis of spherical, octapods and polyhedral

single crystal  $\text{BiVO}_4$ .<sup>[111]</sup> Different structures were obtained by pH and temperature adjustment. Thus, polyhedral  $\text{BiVO}_4$  single crystals were obtained at 189 °C and pH 3, while hydrothermal synthesis at the same temperature, but pH 6 promoted porous spherical structures. Lower temperatures (80 – 100 °C) and pH 3 were used for porous octapods-like  $\text{BiVO}_4$  synthesis. The photocatalytic activity of these materials was evaluated for the removal of phenol and methylene blue under visible light irradiation ( $\lambda > 400$  nm). As commented in previous cases, the morphology of the different  $\text{BiVO}_4$  single crystal influences the surface area and electronic properties including the band gap. Thus, the highest photocatalytic activity was achieved for octapod-like structures compared to that of spheres or polyhedral structures under the same conditions. This fact was justified as derived from the higher specific surface area and lower band gap (2.38 eV) of octapod structures compared with the other two structures (2.43 and 2.42 eV for polyhedral and spherical, respectively). In this case, the smaller band gap promoted extended light harvesting in the visible region.<sup>[111]</sup>

Very different approach has been employed in the multi-step single-crystal to single-crystal transformation of  $\text{Bi}[\text{Fe}(\text{CN})_6] \cdot 4\text{H}_2\text{O}$  coordination polymer into mesoporous  $\text{BiFeO}_3$  single crystals with perovskite structure. The process requires sequential thermal treatments up to temperatures of 800 °C in air. The resulting mesoporous  $\text{BiFeO}_3$  single crystals demonstrated visible-light induced photocatalytic activity towards Rhodamine B degradation.<sup>[112]</sup>

Mixed molten salts have also been employed to obtain mesoporous single crystal  $\text{Bi}_2\text{WO}_6$  with integrated tetragonal architecture. This material exhibited superior photocatalytic activity for Rhodamine B degradation and  $\text{O}_2$  evolution from water under visible light irradiation. The photocatalytic properties of  $\text{Bi}_2\text{WO}_6$  PSC have been attributed to the enhanced charge separation and long lifetime of electron and holes due to its single crystal structure.<sup>[113]</sup>

Finally, crystal phase and morphology have been controlled in solvothermal synthesis by adjusting the pH in the  $\text{Bi}_3\text{NbO}_7$  PSC nanosheets preparation. The pH increase promoted regular porosity and narrower band gap in the  $\text{Bi}_3\text{NbO}_7$  PSC nanosheets. Therefore, the photocatalytic

activity toward Rhodamine B and salicylic acid degradation can be improved using the  $\text{Bi}_3\text{NbO}_7$  PSC nanosheets prepared at the highest pH value (pH=13), which exhibited the highest surface area and narrower band gap. In addition, this photocatalyst could be reused four times with no apparent deactivation or morphological changes.<sup>[39]</sup>

### *3.1.2 PSC surface area effect in the photocatalytic activity.*

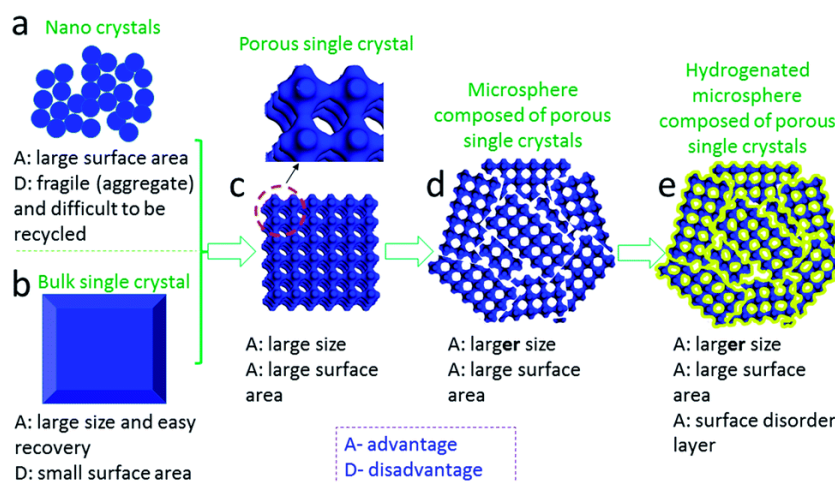
As previously mentioned, the monocrystalline photocatalyst specific surface area is a very relevant property with a strong influence on the photocatalytic activity. As a general rule an increase of semiconductor surface promotes an enhancement on the number of catalytic sites per volume unit, increasing in this way the photocatalytic efficiency of the material. It has been also commented that a general strategy to increase surface area is to generate porosity in a bulk crystal. Section 2 has been organized according to the various strategies for pore generation in single crystal materials and the advantages of these materials with regard the photocatalytic application is by now well established. The aim of some synthetic procedures is to retain the single crystal structure of the bulk material, while increasing surface area by generating porosity.

In one of these examples, anatase PSCs with different pore sizes were obtained by silica-templated hydrothermal method.<sup>[114]</sup> In this study, different silica spheres comprising diameters from 23 to 160 nm were prepared and subsequently utilized as hard templates in the preparation of anatase PSCs. In this way, the smaller the silica spheres, the smaller their pore size and the higher the surface area of the resulting  $\text{TiO}_2$ . Moreover, diminution of pore size was accompanied by an increase in UV absorption, while photoluminescence intensity decreased. These observations indicate that pore size not only affects particle morphology, but also causes changes in the optoelectronic properties of the semiconductor, keeping crystallinity unaffected. Photocatalytic tests confirmed that the ability to generate  $\text{OH}\cdot$  increases upon pore size

decrease. The authors attributed this behavior to the combined effect of increasing number of surface active sites, the higher extent of radical species generated by the exposed electrons and holes and the favorable charge carrier mobility.<sup>[114]</sup>

The use of nanostructures has become of paramount importance in photocatalysis due to the increased surface area that this class of solids presents compared with the same materials in bulk. However, bulk materials are generally easier to recover, and therefore, more suitable for consecutive reuses. In order to combine these properties, Niu et al. proposed the preparation of anatase microspheres built from PSC units through a silica template-based synthesis using  $(\text{NH}_4)_2\text{TiF}_6$  and water as precursors, see **Scheme 22**.<sup>[115]</sup> The combination of the large size of the micrometric spheres, which benefits their recovery, together with the large surface area and high electron mobility of the PSCs promoted good photocatalytic activity towards methyl orange degradation, while good recyclability was demonstrated. Moreover, post-synthetic hydrogenation process further enhanced the photocatalytic activity due to a favorable surface amorphization. While this post-synthetic treatment does not produce any morphological change, UV-Vis diffuse reflectance measurements revealed that hydrogenated samples presented higher and broader light absorption range than the parent samples. Raman spectroscopy revealed that hydrogenation causes a disorder of the original symmetry of the  $\text{TiO}_2$  lattice due to the generation of oxygen vacancy.<sup>[115]</sup> Altogether, the treated PSC microspheres provided 4-fold higher photocatalytic activity over the anatase microspheres not submitted to hydrogenation. Filtration tests demonstrated that these microspheres are recovered in 10 s, while  $\text{TiO}_2$  Degussa P25 NPs needed 320 s. In addition, the recovery ratio for anatase microspheres was of 95 %, while the recovery in P25 was of 72 %, showing that due to their large size and mass, anatase microspheres present better recyclability.<sup>[115]</sup>

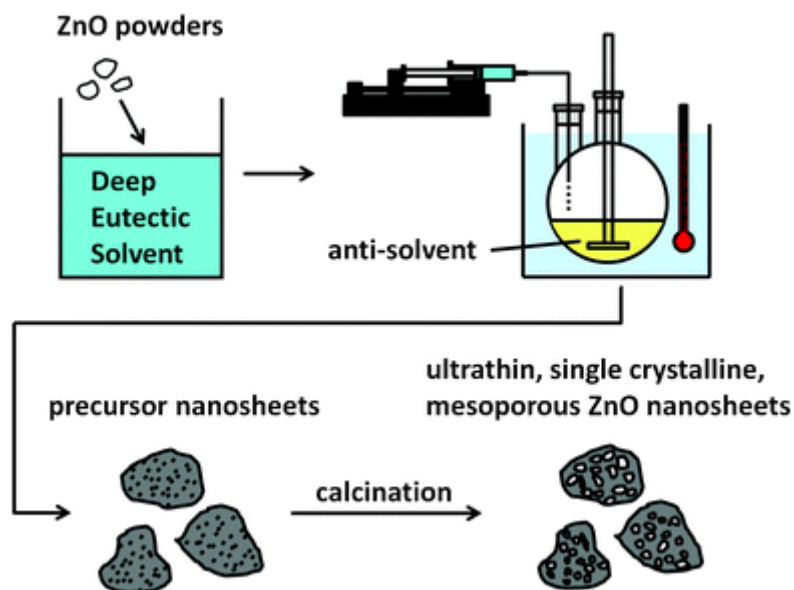




**Scheme 22.** Preparation method of anatase  $\text{TiO}_2$  microspheres composed of porous single crystals. Reproduced with permission.<sup>[115]</sup> Copyright (2015) Royal Society of Chemistry.

As commented in the previous section, although the photocatalytic pollutant degradation has been mainly dominated by  $\text{TiO}_2$ , other semiconductors have also been tested in order to improve their photocatalytic efficiency. For these other photocatalysts, different strategies have been reported to increase the surface area, achieving also notable improvements in their photocatalytic activity respect to the bulk crystals.

In one of these examples, single crystal mesoporous  $\text{ZnO}$  nanosheets were synthesized by a deep eutectic solvent (DES)-based antisolvent process followed by calcination.<sup>[47]</sup> DES are a class of room temperature ionic liquids obtained by mixing two solids of high melting point. DES have advantageous solvent properties, such as high polarity, negligible vapour pressure and thermal stability, among others. These solvents based on ionic liquids can be prepared by mixing quaternary ammonium salts with hydrogen-bond donors at low temperatures (100 °C). It has been reported that DES can dissolve metal oxides, however, they become insoluble when the solution is mixed with an “antisolvent” that shows no solvation ability toward the metal oxides, causing the precipitation of the metal oxide<sup>[47]</sup>. This preparation procedure is presented as **Scheme 23**.



**Scheme 23.** Preparation procedure of ZnO MSC nanosheets with antisolvent-based process.

Reproduced with permission.<sup>[47]</sup> Copyright (2012) Royal Society of Chemistry.

In the present case, ZnO powder and a DES prepared from urea and choline chloride were mixed and the obtained solution injected in water. A precipitate composed by nanosheets of 10 nm thick was formed, and the obtained nanostructures were calcinated at temperatures between 300 and 400 °C, achieving different pore size from less than 10 nm to several tens of nm when calcination temperature was increased. The obtained material was randomly-stacked, single crystal, mesoporous ZnO nanosheets. The mesoporous ZnO nanosheets demonstrated a good photocatalytic activity towards methylene blue and Rhodamine B degradation. The authors attribute this good performance to the higher concentration of -OH groups present on the surface of these samples.<sup>[47]</sup> While the photocatalytic activity for methylene blue degradation was almost independent of the nanosheet pore size, faster Rhodamine B degradation was found in ZnO nanosheets containing larger pores. These observations could be related to the internal vs. external location of the photodegradation process.

In a different approach, high porosity was induced in single crystal ZnO nanoplatelets through a low temperature hydrothermal synthesis followed by thermal annealing.<sup>[116]</sup> The as-prepared

ZnO nanoplatelets were 12 nm thick and contained pores from 10 to 100 nm size. This porous structure caused large amount of surface defects which worked as hole trapping sites, increasing the recombination lifetime between electron and holes and thus, increasing the photocatalytic activity towards the simultaneous photoreduction of Cr(VI) and photooxidation of phenol under UV light. What is more, independent measurements of the photocatalytic activity towards Cr(VI) photoreduction or phenol photooxidation revealed that the photocatalytic activity of the ZnO PSC nanoplatelets in the individual reactions is lower than for the simultaneous photoredox process, indicating a synergic effect in the simultaneous photocatalytic Cr(VI) photoreduction and phenol degradation, a fact that can be probably rationalized by the cooperative effect of simultaneous hole (phenol) and electron (Cr<sup>VI</sup>) quenching.<sup>[116]</sup>

A different synthetic strategy was used in the Cd<sup>2+</sup> cation introduction in the ZnO nanorod arrays through chemical bath deposition and final calcination.<sup>[77]</sup> The pore concentration and ZnO nanorod aspect ratio were adjusted by the Cd<sup>2+</sup> concentration and reaction temperature. Considering the toxicity of Cd<sup>2+</sup> salts, it would have been convenient to test alternative metal cations for the same process. In any case, the as-prepared mesoporous ZnO nanorod arrays exhibited improved photocatalytic activity towards methylene blue degradation respect to the non-porous ZnO nanorod arrays upon UV light irradiation with a 300 W Hg lamp, being degraded over 90 % of the methylene blue with the porous ZnO nanorods array, while less than 70 % was degraded with non-porous ZnO nanorod arrays under exactly the same conditions.<sup>[77]</sup> Generation of pores in the single crystal materials is not the only way to increase the porosity, and therefore, the specific surface area. In a very different approach Lou et al. reported the preparation of hollow single crystal CoSn(OH)<sub>6</sub> nanostructures.<sup>[117]</sup> This material was obtained through a one-pot “*pumpkin-carving*” protocol. In this method, MSC hollow structures with multilevel interior are obtained from simultaneous fast growth of CoSn(OH)<sub>6</sub> nanocube single crystals and kinetically-controlled etching in alkaline medium. The obtained CoSn(OH)<sub>6</sub> hollow nanostructures can be converted in Sn-based ternary metal oxides under thermal

treatment at 700 °C in nitrogen atmosphere. The mixed  $\text{Co}_2\text{SnO}_4$  and  $\text{SnO}_2$  compounds in the MSI hollow structure presented excellent photocatalytic activity towards methylene blue degradation under UV irradiation ( $\lambda = 254 \text{ nm}$ ).<sup>[117]</sup>

Besides  $\text{TiO}_2$  and  $\text{ZnO}$ , other metal oxide semiconductors have also been prepared with PSC structure, exhibiting improved photocatalytic efficiency. Dong and coworkers reported the preparation of NiO PSC nanosheets using a surfactant-free template-based solvothermal process and subsequent thermal treatment.<sup>[118]</sup>  $\beta\text{-Ni}(\text{OH})_2$  nanosheets of 400 nm length and 20 nm thick were obtained after the solvothermal synthesis. Thermal decomposition of the  $\beta\text{-Ni}(\text{OH})_2$  nanosheets at temperatures between 350 and 550 °C forms NiO nanosheets with different pore size from meso to macropore. Thus, smaller pores were found in NiO nanosheets thermally treated at 350 °C, while the largest pores were found in samples treated at 550 °C. The photocatalytic activity towards NO degradation (deNO<sub>x</sub>) was tested with porous NiO nanosheets prepared at 350, 450 and 550 °C. It was found that the photocatalytic deNO<sub>x</sub> ability of NiO nanosheets with the smallest pores (350 °C) was higher than the NiO nanosheets prepared at higher temperatures (450 and 550 °C) with bigger pores, even under visible light irradiation ( $\lambda > 400 \text{ nm}$ ). This is due to the higher specific surface area of the material with the smallest pores compared to values with bigger pores. The NiO PSC nanosheets presented photocatalytic activity at wavelengths longer than 510 nm, exhibiting up to 40 % NO<sub>x</sub> degradation and, therefore, they exhibit an interesting visible light photoresponse.<sup>[118]</sup>

### *3.1.3 Doped PSCs in environmental remediation.*

Metal doping is a general strategy to improve the photocatalytic activity of bulk semiconductors and, particularly to introduce visible light photoresponse. Photocatalyst doping with transition metals has been found a convenient approach to alter its electronic and catalytic properties as consequence of Fermi level tuning, decrease in CB position and/or the formation of defects

such as oxygen vacancies. The changes in the optoelectronic properties of the photocatalyst caused by doping can either enhance the visible light harvesting through band gap tuning or increase the activity of the sites, respect to the undoped material.

In one selected example, highly porous single crystal (001) face Zn-doped TiO<sub>2</sub> nanowalls were vertically grown on ITO substrate via a liquid-phase deposition method.<sup>[119]</sup> In this process, [(NH<sub>4</sub>)<sub>2</sub>TiF<sub>6</sub>], Zn(NO<sub>3</sub>)<sub>2</sub>·xH<sub>2</sub>O and hexamethylenetetramine were employed as TiO<sub>2</sub> source, doping agent and surfactant, respectively. The nanowalls were grown on ITO at temperatures between 50 and 90 °C, and typically presented 2 μm length and 60 nm thick, approximately. The presence of Zn in the anatase structure was confirmed by X-ray energy dispersive (EDX) and X-ray photoelectron spectroscopy (XPS) analysis. The photocatalytic methylene blue degradation using the single crystal Zn-doped TiO<sub>2</sub> nanowalls was explored under UV light (365 nm). The Zn-doped TiO<sub>2</sub> nanowalls resulted about 10 % more efficient photocatalyst for methylene blue degradation than undoped TiO<sub>2</sub> nanowalls.<sup>[119]</sup> This activity enhancement is, however, not too large and could be due to other factors besides doping.

Zn has been one of the most preferred doping metals, and besides doping TiO<sub>2</sub>, Zn has also been used to dope another semiconductor photocatalysts. For instance, Zn(II)-doped γ-Fe<sub>2</sub>O<sub>3</sub> single crystal nanoplatelets were obtained by low temperature (180 °C) thermal decomposition of solvothermal precursors (Zn(OAc)<sub>2</sub>), FeCl<sub>3</sub> and urea, and subsequent calcination process.<sup>[120]</sup> It has been previously reported that the superparamagnetic γ-Fe<sub>2</sub>O<sub>3</sub> suffers from phase transformation to the antiferromagnetic α-Fe<sub>2</sub>O<sub>3</sub> at temperatures higher than 300 °C.<sup>[121]</sup> Zn doping arrests the phase transformation from γ-Fe<sub>2</sub>O<sub>3</sub> to α-Fe<sub>2</sub>O<sub>3</sub> up to 600 °C approximately. Even more, it was observed that the phase transition temperature increased along the Zn loading. Thus, due to the effect of Zn, superparamagnetic properties in γ-Fe<sub>2</sub>O<sub>3</sub> could be maintained, while well-developed single crystalline structures were achieved, even at calcination temperatures higher than 450 °C. In addition, the Zn(II)-doped γ-Fe<sub>2</sub>O<sub>3</sub> single crystal nanoplatelets showed good photocatalytic activity towards Rhodamine B degradation

under visible light irradiation. It was observed that about 80 % of the Rhodamine B was degraded using the Zn(II)-doped  $\gamma$ -Fe<sub>2</sub>O<sub>3</sub> single crystal, while only 60 % was degraded using TiO<sub>2</sub> P25 as bench mark photocatalyst in the same conditions <sup>[120]</sup>.

The use of dopants is not limited to metal elements different from the photocatalyst composition. Different oxidation states of the same metal can be simultaneously present in the crystalline structure, this resulting in self-doping of the semiconductor. In one of these examples, anatase TiO<sub>2</sub> single crystals were self-doped with Ti<sup>3+</sup> to enhance the visible light photocatalytic activity for deNO<sub>x</sub>.<sup>[122]</sup> In this report, spindle-like TiO<sub>2</sub> anatase single crystals were prepared by one-step hydrolysis in PEG-400. The mesoporous anatase single crystals were formed during reaction through oriented aggregation of pre-formed nanocrystals, which can be easily fused in situ into PSC by air annealing. It was shown that if the thermal process is carried out under vacuum, Ti<sup>3+</sup> sites are spontaneously generated, resulting in the formation of Ti<sup>+3</sup> self-doped anatase single crystals. The as-prepared Ti<sup>+3</sup> self-doped anatase single crystals exhibited visible light photocatalytic activity towards deNO<sub>x</sub>. The authors attributed this expanded visible-light photoresponse to Ti<sup>+3</sup> self-doping that results in electronic band structure modification and slowed down electron-hole pair recombination kinetics. As consequence, in contrast to undoped anatase samples, an additional visible absorption band appeared from 400 to 800 nm, which is indicative of a band gap decrease. Moreover, the emission intensity in Ti<sup>+3</sup> self-doped anatase single crystals was significantly weaker indicating that the recombination of the photogenerated electron-hole pairs was efficiently slowed down. These observations serve to justify the enhanced visible light activity of Ti<sup>+3</sup> self-doped anatase PSCs towards photocatalytic NO removal.<sup>[122]</sup>

In a different approach to achieve visible light photoresponse, Er<sup>+3</sup>-doped  $\beta$ -Bi<sub>2</sub>O<sub>3</sub> nanosheets with preferentially exposed (0 0 1) facets were prepared through a template-free hydrothermal synthesis. In this preparation procedure, the use of acetic acid and ethanol as co-solvents was found crucial for the nanosheet formation with preferential (0 0 1) facet orientation. The

$\beta$ -Bi<sub>2</sub>O<sub>3</sub> nanosheets exhibited a large concentration of pores, which increase the density of defects acting as sites for the photocatalytic degradation under UV irradiation. The authors claim Er<sup>+3</sup>-doped  $\beta$ -Bi<sub>2</sub>O<sub>3</sub> exhibits upconversion, meaning that two visible photons are converted into a UV photon. However, it is unclear the contribution of up-converted UV photons in the photocatalytic activity. Although the experiments were light-driven by a 300 W Xe lamp, high-power light source (laser) must be employed in order to obtain significant up-conversion into UV. Er<sup>+3</sup>- $\beta$ -Bi<sub>2</sub>O<sub>3</sub> was tested as photocatalyst for Rhodamine B degradation.<sup>[123]</sup> An optimal Er<sup>+3</sup> loading of 0.8 wt% was determined in order to maximize the conversion of visible light into UV, this resulting in an enhancement of the photocatalytic activity towards Rhodamine B degradation with respect to undoped  $\beta$ -Bi<sub>2</sub>O<sub>3</sub> nanosheets. The authors attributed this improved photocatalytic activity to the visible light harvesting ability of Er<sup>+3</sup>-doped  $\beta$ -Bi<sub>2</sub>O<sub>3</sub> nanosheets combined with the upconversion process increasing the number of UV photons that would lead to e<sup>-</sup>/h<sup>+</sup> separation in  $\beta$ -Bi<sub>2</sub>O<sub>3</sub> semiconductor.<sup>[123]</sup>

#### 3.1.4 Pollutant degradation by PSC photocatalysts containing co-catalysts

It is well established in photocatalysis that the presence of certain components on the semiconducting photocatalyst surface can influence positively the efficiency of the photocatalytic process<sup>[124]</sup>. These components are generally named co-catalysts and it is assumed that these components can improve charge separation or are involved in an enhanced light absorption or they catalyze dark steps in the mechanism. The way in which co-catalysts are deposited on the photocatalyst surface and their composition determine frequently their ability to enhance the photocatalytic processes.

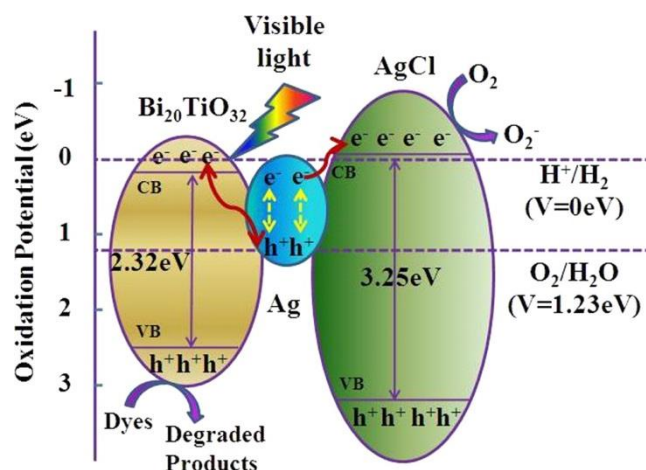
One of the most frequently claimed role of co-catalysts is accumulation of CB electrons or VB holes from the semiconductor to promote locally on them photoreduction or photooxidation reactions, respectively. The most preferred co-catalysts for reductive processes are noble metal

NPs that due to their noble character do not undergo oxidation upon exposing the photocatalyst to the ambient or during the photocatalytic reaction.<sup>[125]</sup> These noble metal NPs can buffer electrons from the semiconductor. Besides noble metal NPs, other types of co-catalysts are also well-established, including metal oxides that appear to be more convenient co-catalysts for oxidative processes.<sup>[126]</sup> Furthermore, co-catalysts are not limited to metals or metals oxides, and organic molecules and enzymes have recently attracted attention also as co-catalysts.<sup>[127]</sup> So far, metal Au NPs (NPs) are among the most widely used cocatalysts. In one of these reports, the photocatalytic degradation of isopropanol has been reported by nanoporous single crystal SrTiO<sub>3</sub> photocatalyst prepared at low temperature through sol-gel process and loaded with Au NPs as co-catalyst.<sup>[128]</sup> Depending on their size Au NPs exhibit a well-known strong plasmon resonance band in the visible region.<sup>[129]</sup> The combination of the single crystal nature of the SrTiO<sub>3</sub> and the space confinement effect in its nanopores of photoelectrons generated by Au NP excitation are the main factors proposed to explain the enhanced photocatalytic activity. In this example, the nanoporous single crystal SrTiO<sub>3</sub> synthesis was crucial since the pore size determines the space confinement of the Au NPs. To prepare the material, Ti and Sr precursor solutions were mixed, allowing slow solvent evaporation for a week to age the SrTiO<sub>3</sub> solution. Then, basic dissolution affords the nanoporous single crystal SrTiO<sub>3</sub>, achieving a porosity maximum when the etching is carried out to 60 °C. This procedure gives rise to shallow cavities rather than a fully developed channel network typical for most mesoporous materials. Au NPs grow in these cavities with diameters ranging from 3 to 6 nm. Au NPs-supported single crystal SrTiO<sub>3</sub> was tested as photocatalyst for isopropanol degradation, exhibiting 45-fold higher photocatalytic activity than commercial SrTiO<sub>3</sub> NPs with similar Au NPs loading. The authors attributed this enhanced activity to the especial morphology of the synthesized SrTiO<sub>3</sub> particles. An optimal Au loading of 4.8 wt% maximized the photocatalytic isopropanol degradation. Au overloading was detrimental for this photocatalytic application.<sup>[128]</sup>



Apart from Au, Ag is another plasmonic metal that has been widely reported in photocatalytic applications. However, due to the higher tendency of Ag to undergo oxidation to  $\text{Ag}^+$ , photocatalyst stability of materials containing Ag NPs has to be firmly demonstrated by elemental analysis and exhaustive characterization after its use as photocatalyst of the morphology and particle size distribution of Ag NPs. In a typical example, Ag NPs as cocatalysts were deposited in rutile  $\text{TiO}_2$  MSC rods, studying its photocatalytic activity towards Rhodamine B degradation.<sup>[130]</sup> Characterization showed that the Ag NPs are homogeneously dispersed within the channels of the mesoporous single crystal  $\text{TiO}_2$  rods. The photocatalytic activity of single crystal  $\text{TiO}_2$  rods with Ag NPs was higher than that of the bare  $\text{TiO}_2$  rods. The degradation of Rhodamine B under sun-simulated light and visible light increased with the Ag loading. However, Ag overloading resulted in too large Ag NPs and a decrease of the photocatalytic activity due to the lower Ag specific surface area is observed for high Ag loadings.<sup>[130]</sup>

The Ag plasmon band was also used to enhance the visible light harvesting of single crystal  $\text{Bi}_{20}\text{TiO}_{32}$  PSC. In this example, single crystal  $\text{Bi}_{20}\text{TiO}_{32}$  nanosheets were prepared by hydrothermal synthesis and subsequent thermal treatment. Later, Ag-AgCl nanocrystals were supported on  $\text{Bi}_{20}\text{TiO}_{32}$  by the deposition-precipitation method, being finally photoreduced in order to obtain the desired photocatalyst. The Ag-AgCl/ $\text{Bi}_{20}\text{TiO}_{32}$  photocatalyst demonstrated excellent visible-light activity for Rhodamine B and acid orange 7 dyes degradation. It was proposed that the Ag-AgCl/ $\text{Bi}_{20}\text{TiO}_{32}$  photocatalyst operates according to a Z-scheme, one of the semiconductors being  $\text{Bi}_{20}\text{TiO}_{32}$  and the other AgCl (see **Scheme 24**). The composite material based on single crystal  $\text{Bi}_{20}\text{TiO}_{32}$  exhibits higher photocatalytic activity than Ag-AgCl nanocrystals or mesoporous  $\text{Bi}_{20}\text{TiO}_{32}$  nanosheets separately. This enhanced photocatalytic activity has been attributed to the efficient charge transfer from plasmon-excited Ag nanocrystal to  $\text{Bi}_{20}\text{TiO}_{32}$  semiconductor in the Z-scheme.<sup>[131]</sup>



**Scheme 24.** Z-Scheme Ag-AgCl/Bi<sub>20</sub>TiO<sub>32</sub> photocatalyst and photoinduced charge transfer processes. Reproduced with permission.<sup>[131]</sup> Copyright (2013) American Chemical Society.

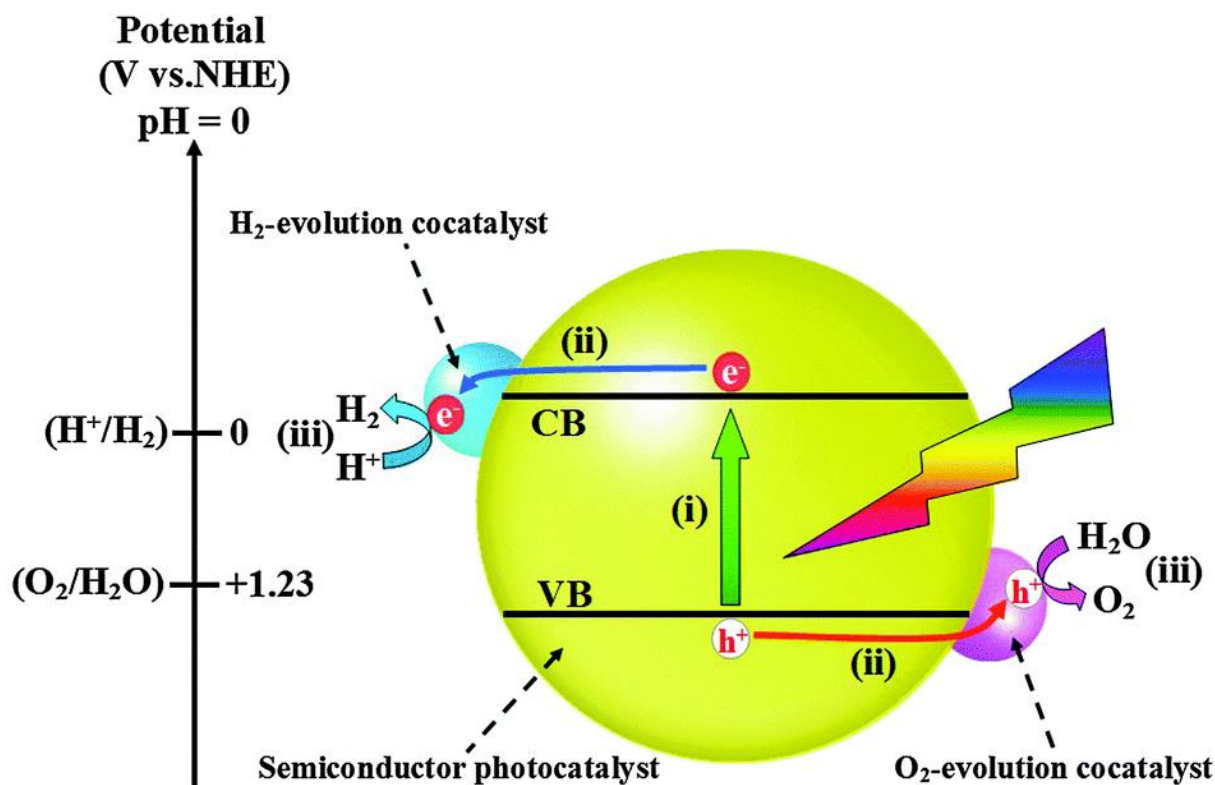
Similarly, carbon nanotubes (CNT) have been used as support of anatase TiO<sub>2</sub> PSC prepared by a one-pot chemical route and subsequent annealing at temperatures between 200 and 600 °C. The composite material was evaluated for the photocatalytic decomposition of methylene blue. It was found that annealing at 200 °C produces spindle-like anatase TiO<sub>2</sub> mesocrystals, while further temperature increases up to 400 °C promotes morphological changes from mesoporous to porous single crystals and stronger chemical bonding between the CNT and the TiO<sub>2</sub>. At 600 °C the TiO<sub>2</sub> and CNT were separated due to the different thermal expansion coefficients. The photocatalytic activity of the TiO<sub>2</sub>/CNT composite was maximum upon annealing at a temperature of 400 °C due to the combination of the single crystal nature of the TiO<sub>2</sub> and the strengthened Ti-O-C bonds appearing when the annealing is carried out at this temperature giving rise to an efficient charge separation.<sup>[95]</sup>

### 3.2 Photocatalytic water splitting.

Single crystal materials have been used as photocatalysts in applications different from pollutant degradation. This is the case of fuels production using solar light as primary energy

source. This area is generally denoted as photocatalytic “solar fuels” production. Aimed at the shift from fossil fuels to renewable energy sources, considerable attention is being paid since the last decade in the generation and use of H<sub>2</sub> as a potential energy vector. In this context, photocatalytic water splitting can be a viable clean technology for the production of H<sub>2</sub> directly from H<sub>2</sub>O using sunlight. H<sub>2</sub> has been typically obtained from oil and natural gas through steam reforming, while only 4 % is currently produced through H<sub>2</sub>O electrolysis. However, new methods to generate H<sub>2</sub> from water, particularly salted water, based on renewable and sustainable resources are highly wanted. Photocatalytic water splitting using solar light could be a suitable method to directly convert solar energy into hydrogen.

Generation of H<sub>2</sub> and O<sub>2</sub> from H<sub>2</sub>O by UV irradiation was first reported in 1972 by Fujishima and Honda using TiO<sub>2</sub> photoelectrodes.<sup>[102]</sup> In photocatalytic water splitting, oxidation and reduction reactions should take place simultaneously at the same rate upon irradiation of a semiconductor material as depicted in **Scheme 25**. The mechanism consists in four main steps similar to the ones described in the photocatalytic pollutant degradation. The first step consists in the photogeneration of electron-hole pairs upon photon absorption. As described in the previous section, the photon energy should be high enough to promote electrons from the semiconductor VB into the CB. The second step involves electron and hole migration through the semiconductor to the particle surface. Finally, the last step corresponds to the oxidation and reduction semireactions on the semiconductor surface, where, in the present case, water is oxidized to produce O<sub>2</sub> and H<sup>+</sup>, and simultaneously H<sup>+</sup> are reduced to H<sub>2</sub> (see Scheme 25).



**Scheme 25.** Fundamental steps in photocatalytic water splitting. Reproduced with permission.<sup>[132]</sup> Copyright (2014) Royal Society of Chemistry.

For the sake of fulfilling the electroneutrality principle, reduction process has to occur at the same reaction rate as the oxidation reaction. This requirement of simultaneous oxidation and reduction on the surface of each particle makes necessary that in the photocatalytic process besides the targeted  $\text{H}_2$ , stoichiometric amounts of  $\text{O}_2$  have to be simultaneously formed.

It happens that frequently oxidation is kinetically slower than reduction. In order to decouple oxidation and reduction semireactions, achieving the maximum possible efficiency of the photocatalytic reduction process, it is very common that evaluation studies use a sacrificial agent, whose role is to quench efficiently at high rate photogenerated holes, allowing to study separately the reduction process under conditions in which this semireaction becomes presumably the rate limiting step. Preferred hole quenchers in  $\text{H}_2$  evolution studies are tertiary amines, particularly triethanolamine and triethylamine, alcohols, specially methanol and ethanol, but also inorganic anions such as sulfide, sulfite and nitrate. Analogous strategy using

electron quenchers can be used to study separately  $O_2$  evolution from  $H_2O$ . Typical electron quenchers for  $O_2$  evolution reaction are  $Ag^+$  or  $Ce^{+4}$  salts.

Among the most studied photocatalysts for water splitting,  $TiO_2$  is again the preferred one due to its adequate CB and VB potentials for water reduction and oxidation reactions, respectively, high photochemical stability, low cost, lack of toxicity and abundance. Different samples of this semiconductor have been tested for  $H_2$  generation, including, for instance, rutile  $TiO_2$  MSC nanorods of different size or anatase nanosheets. Both types of  $TiO_2$  materials have been prepared by a silica template hydrothermal synthetic method.<sup>[104]</sup> As commented in the previous section, the single crystal anatase nanosheets with preferential {001} facets were found most suitable for pollutant degradation, while, on the other hand, the rutile nanorods exhibited higher  $H_2$  evolution rates in water:methanol mixtures (70:30, v:v) in the presence of  $H_2PtCl_6$  upon 300 W Xe lamp irradiation. Pt NPs were photodeposited in situ, while photocatalytic  $H_2$  evolution was taking place, obtaining a maximum of 37 mmol of  $H_2/g$  of photocatalyst for 4 h reaction.<sup>[104]</sup> It should be commented that under these conditions the photocatalytic activity of rutile nanorods should be constantly changing as consequence of photodeposition of Pt that is known to act as co-catalyst in this process.

In a different approach,  $TiO_2$  MSC nanofibers were prepared from  $K_2Ti_2O_9$  precursor by hydration, cation exchange in the presence of HCl, and final calcination at 500 °C in air for 2 h.<sup>[133]</sup> The  $H_2$  evolution was evaluated in  $H_2O:MeOH$  mixtures (90:10, v:v) in the presence of 0.5 wt% Pt NPs upon 300 W high-pressure Hg lamp irradiation. After 5 h irradiation, 100 mmol/g of  $H_2$  were approximately produced and the photocatalysts was reused 3 times, demonstrating no degradation.<sup>[133]</sup>

In a seminal paper, Kondo et al. reported the preparation of  $Ta_2O_5$  PSCs and their photocatalytic activity towards overall water splitting was compared with that of amorphous  $Ta_2O_5$ .<sup>[134]</sup> In this work, it is demonstrated that although some amorphous mesoporous materials present a notable photocatalytic activity, such as  $Ta_2O_5$ , crystallization at high temperatures, keeping the porous

structure, give rise to an improved photocatalytic activity. Different methodologies have been developed to maintain the original mesoporous structure after crystallization.<sup>[135]</sup> In the present case, 2D-hex mesoporous Ta<sub>2</sub>O<sub>5</sub>, as amorphous precursor, was calcinated at high temperature (1133 K) for crystallization, while reinforcing the pore walls was carried out by [CH<sub>3</sub>]<sub>3</sub>SiO]<sub>2</sub>-SiHCH<sub>3</sub>, which evolved to SiO<sub>2</sub> upon calcination. The SiO<sub>2</sub> restricted mass transfer during crystallization, and thus, preventing the pore collapse. The photocatalytic activity for overall water splitting under UV irradiation was evaluated using NiO<sub>x</sub>-loaded amorphous and crystallized Ta<sub>2</sub>O<sub>5</sub>, obtaining nearly 1 order of magnitude higher activity with the crystallized sample.<sup>[134]</sup> This example clearly shows the photocatalytic activity improvement of mesoporous materials upon crystallization.

In different example, Ta<sub>2</sub>O<sub>5</sub> microcubic single crystals were prepared by thermal treatment at 650 °C for 6 h under a moist Ar flow of the TaO<sub>2.18</sub>Cl<sub>0.64</sub> microcubes precursor.<sup>[136]</sup> In spite of the thermal treatment, the resulting Ta<sub>2</sub>O<sub>5</sub> microcubes preserved the structure from the precursor due to the strong 180° Ta-O-Ta bonds, but exhibiting preferential {001} facet orientation in the single crystals. The authors attributed the enhanced photocatalytic activity of the Ta<sub>2</sub>O<sub>5</sub> microcubes compared with commercial Ta<sub>2</sub>O<sub>5</sub> to the enlargement of the percentage of {001} facet, which promoted enhanced photocatalytic activity towards H<sub>2</sub> evolution.<sup>[136]</sup> Theoretical calculations indicate that the {001} facets contain larger active sites density for H<sub>2</sub> evolution. Thus, 0.9 mmol of H<sub>2</sub>/m<sup>2</sup> was obtained in H<sub>2</sub>O:lactic acid mixtures (70:30, v:v) for a Ta<sub>2</sub>O<sub>5</sub> PSC containing 5 wt% Pt NPs upon 300 W Xe lamp irradiation for 8 h.<sup>[136]</sup>

3D single crystal-like porous SrTiO<sub>3</sub> was synthesized by hydrothermal reaction at 150 °C for 10 h using flower-like layered protonated titanate hierarchical spheres as precursor.<sup>[137]</sup> The dimensions of the protonated titanate spheres were submicrometric. The architecture of the resulting porous SrTiO<sub>3</sub> was composed by assembly of nanocubes (approximately 60-80 nm length) exhibiting {100} facets and explain single crystal structure (**Figure 11**). The obtained porous SrTiO<sub>3</sub> exhibited a 3.25 eV band gap and in the presence of 1 wt% Pt NPs was very

efficient photocatalyst for  $H_2$  evolution from  $H_2O:MeOH$  mixtures (80:20 v:v %) under UV irradiation ( $< 386$  nm).<sup>[137]</sup>

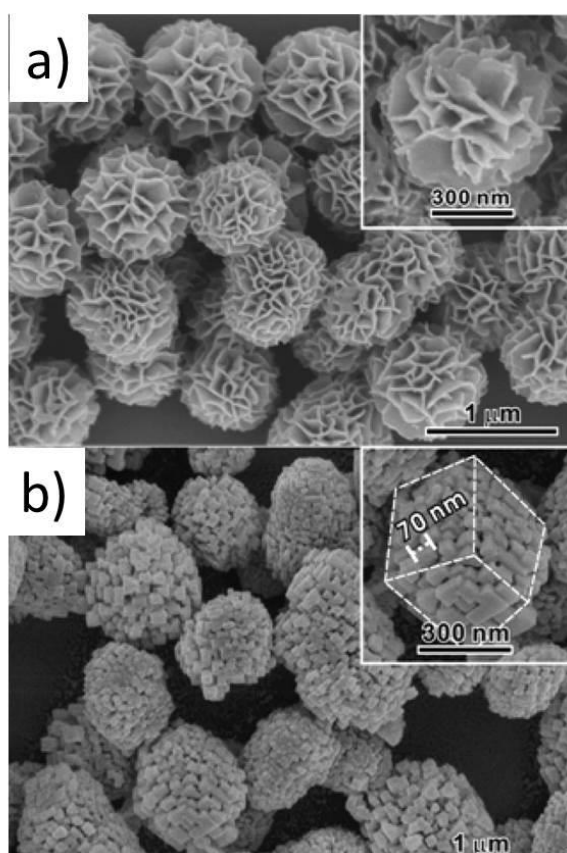


**Figure 11.** SEM images of (a) the flower-like precursor and (b) of the 3D single crystal-like porous  $SrTiO_3$ . Reproduced with permission.<sup>[137]</sup> Copyright (2013) American Chemical Society.

Very different approach was employed by Li et al. in the synthesis of  $SrTiO_3$  PSCs.<sup>[138]</sup> In this case, a molten salt route using alkaline hydroxides was employed, where  $SrCl_2$  and  $TiO_2$  were mixed with  $NaOH/KOH$  at  $205$  °C for 1 to 7 days. The  $NaOH/KOH$  molten salt route promoted the formation of  $SrTiO_3$  cubic perovskite suitable for  $H_2$  evolution. The best production was obtained from the  $SrTiO_3$  sample obtained upon heating for 7 days, measuring  $12$  mmol of  $H_2/g$  employing  $H_2O:MeOH$  mixtures (80:20 v:v %) upon 300 W Xe lamp irradiation in 9 h.<sup>[138]</sup> The  $SrTiO_3$  contained 1 wt% Pt NPs as co-catalyst.

Most of the previous examples use as irradiation source a Xe lamp that emits photons in the UV range from 300 to 400 nm as well as the visible range from 400 till 800 nm. The photocatalytic activity of the previous samples derives exclusively from the UV region. Considerable efforts have been carried out in order to prepare photocatalysts capable to promote H<sub>2</sub> evolution under visible light irradiation. The interest derives from the large percentage of visible light in natural sunlight reaching the Earth crust (about 42 % in energy) in comparison to the UV radiation (about 4 % energy). To achieve visible light photoresponse, nanoporous single crystal Cd<sub>x</sub>Zn<sub>1-x</sub>S nanosheets were synthesized using hybrid organic-inorganic DETA-ZnS sheets as starting material. Subsequent Zn to Cd cation exchange at 160 °C for 6 h forms single crystal Cd<sub>x</sub>Zn<sub>1-x</sub>S nanosheets (Zn:Cd molar ratio of 1:1).<sup>[14a]</sup> Further increase in Cd concentration up to a Zn:Cd molar ratio of 1:2 promoted complete cation exchange and thus, CdS porous nanosheets could also be obtained. However, the photocatalytic activity towards H<sub>2</sub> evolution was higher when Cd<sub>x</sub>Zn<sub>1-x</sub>S nanosheets were used as photocatalyst in comparison with CdS nanosheets. For sulfide photocatalysts, the use of soluble sulfide salts as sacrificial electron donors is recommended to increase photocatalyst stability and minimize photocorrosion. Thus, under favorable conditions 8.3 mmol of H<sub>2</sub>/g was obtained in 5 h from H<sub>2</sub>O containing 0.5 M Na<sub>2</sub>S and 0.5 M Na<sub>2</sub>SO<sub>3</sub> as sacrificial reagents upon 300 W Xe lamp illumination of the single crystal Cd<sub>x</sub>Zn<sub>1-x</sub>S nanosheets. In contrast, only 3.3 mmol of H<sub>2</sub>/g was achieved when CdS nanosheets were used under identical conditions.<sup>[14a]</sup> The authors attributed this improvement to the narrower band gap and stronger photon absorption that exhibit single crystal Cd<sub>x</sub>Zn<sub>1-x</sub>S nanosheets compared to CdS nanosheets.<sup>[14a]</sup>

It is worth noticing that although H<sub>2</sub> is typically the most wanted product in the photocatalytic water splitting reaction due to the possibility to use it directly as fuel or as reagent in hydrogenation reactions, the oxidation semireaction is simultaneously taking place. In any industrially viable H<sub>2</sub> generation, no sacrificial chemicals can be probably used and the two processes H<sub>2</sub> generation and useful oxidation must occur simultaneously. In this regard, the



study of the photocatalytic reduction and oxidation semireactions separately are interesting only to provide a better understanding of the rate limiting step. Thus, for instance, Liu et al. prepared rutile TiO<sub>2</sub> MSC through a seeded template method. In this study hydrothermal treatment of TiCl<sub>4</sub> in HCl and NaF was carried out.<sup>[139]</sup> The F<sup>-</sup> ions were found to play a key role stabilizing the high energy facet (111) of the rutile single crystals. The as-prepared TiO<sub>2</sub> rutile PSCs were submitted to irradiation with 300 W Xe lamp in H<sub>2</sub>O:MeOH mixtures (90:10 v:v %). The mesoporous rutile single crystals both exhibited 6 times higher H<sub>2</sub> production (1000 μmol/g) than the non-mesoporous bulk single crystals both containing 1 wt% of Pt NPs formed by the photodeposition method. On the other hand, the mesoporous rutile single crystals were also irradiated for 5 h in aqueous solutions using AgNO<sub>3</sub> (16.7 mM) as electron acceptor, obtaining 900 μmol of O<sub>2</sub>/g, 2.6 times higher O<sub>2</sub> production than the non-mesoporous bulk single crystals.<sup>[139]</sup> Thus, the authors demonstrated that the mesoporous rutile single crystals are suitable material for photocatalytic overall water splitting, since both reactions H<sub>2</sub> and O<sub>2</sub> evolution can take place, although no direct information of the photoactivity for overall water splitting was provided. It should be commented that typically the rate determining step in the overall water splitting is the O<sub>2</sub> evolution reaction since according to the reaction stoichiometry the O<sub>2</sub> production should consume twice the electrons required for H<sub>2</sub> evolution.

In a different approach, hollow Co<sub>3</sub>O<sub>4</sub> microspheres composed by porous (< 5 nm) single-crystal nanosheets were fabricated through a self-template synthetic route.<sup>[140]</sup> In this method, solid cobalt alkoxide microspheres were firstly synthesized. Then, self-template conversion into hollow cobalt hydroxide microspheres composed by ultrathin nanosheets was carried out in a Teflon-lined stainless- steel autoclave at 160 °C. Finally, thermal treatment of the hollow cobalt hydroxides into the wanted hollow Co<sub>3</sub>O<sub>4</sub> single crystal microspheres was performed in air at temperatures between 200 and 400 °C.<sup>[140]</sup> Photocatalytic O<sub>2</sub> evolution reaction was studied placing the hollow Co<sub>3</sub>O<sub>4</sub> single crystal microspheres in Na<sub>2</sub>SiF<sub>6</sub>-NaHCO<sub>3</sub> buffer solution (pH = 5.8) in the presence of Ru(bpy)<sub>3</sub>Cl<sub>2</sub> · 6 H<sub>2</sub>O as photosensitizer and Na<sub>2</sub>S<sub>2</sub>O<sub>8</sub> and Na<sub>2</sub>SO<sub>4</sub> as

sacrificial electron acceptor upon 500 W Xe lamp irradiation using a cut-off filter to ensure exclusive visible light irradiation ( $\lambda > 450$  nm). It is worth noticing that in the present case,  $\text{Co}_3\text{O}_4$  PSCs act as oxygen evolution reaction catalyst, while the  $\text{Ru}(\text{bpy})_3\text{Cl}_2$  complex is the light absorber. It was found that the most active photocatalytic system was obtained when the thermal decomposition of cobalt hydroxide was performed at 200 °C, reaching 2.34 mmol of  $\text{O}_2/\text{g}$  in 20 min under visible light irradiation.<sup>[140]</sup>

Similarly,  $\text{BiVO}_4$  MSCs were prepared by one-step hydrothermal method using acidified  $\text{BiVO}_4$  precursors impregnated on silica template.<sup>[141]</sup> The photocatalytic  $\text{O}_2$  evolution was performed under 300 W Xe lamp with a cut-off filter ( $\lambda > 420$  nm) using  $\text{NaIO}_3$  aqueous solutions as sacrificial electron acceptor. The  $\text{BiVO}_4$  MSC demonstrated 10 times improved photocatalytic activity towards  $\text{O}_2$  production under visible light than the nanoporous bulk  $\text{BiVO}_4$ . The authors attributed this behavior to the enhanced surface area and light absorption of MSC compared to the bulk  $\text{BiVO}_4$  due to the inner pores that increase the specific surface area and can act as light scattering centers to localize and trap the incident light.<sup>[141]</sup>

As it has been already commented in the previous section, the use of co-catalysts to enhance the photocatalytic activity has been widely documented.<sup>[124]</sup> In this sense,  $\text{CoO}_x$  is a common co-catalyst to promote the photocatalytic  $\text{O}_2$  evolution reaction. As an example, increasing amounts of  $\text{CoO}_x$  (0.01 – 2 wt%) were deposited on semiconductor single crystal  $\text{LaTiO}_2\text{N}$  photocatalyst to determine its influence in the water oxidation reaction under visible light irradiation.<sup>[142]</sup> The single crystal  $\text{LaTiO}_2\text{N}$  photocatalyst with 2.1 eV bandgap was dispersed in  $\text{AgNO}_3$  aqueous solution and irradiated with a 300 W Xe lamp with a UV cut-off filter ( $\lambda > 420$  nm). In the absence of  $\text{CoO}_x$ , a  $\text{O}_2$  production rate of 125  $\mu\text{mol}/\text{g}\cdot\text{h}$  was obtained, while an optimal 2 wt% of  $\text{CoO}_x$  deposited on  $\text{LaTiO}_2\text{N}$  PSC provided 3.68 mmol/g·h. The activity of  $\text{CoO}_x$  co-catalyst was compared with that of  $\text{IrO}_x$ , which is a benchmark co-catalyst for  $\text{O}_2$  evolution reaction. However,  $\text{IrO}_x$  supported on  $\text{LaTiO}_2\text{N}$  affords under the same conditions only 0.85 mmol of  $\text{O}_2/\text{g}\cdot\text{h}$ .<sup>[142]</sup> In a very similar way, 2 wt%  $\text{CoO}_x$  co-catalyst was deposited

on a series of doped single crystal Ta<sub>3</sub>N<sub>5</sub> photocatalysts. Thus, Ta<sub>3</sub>N<sub>5</sub> as well as Na-doped, Cd-doped and Na-Cd-doped Ta<sub>3</sub>N<sub>5</sub> single crystals were prepared and their activity for the photocatalytic O<sub>2</sub> evolution tested in 10 mM aqueous AgNO<sub>3</sub> solution upon 300 w Xe lamp irradiation with a UV cut-off filter ( $\lambda > 420$  nm). It was found that Na-doped Ta<sub>3</sub>N<sub>5</sub> single crystals containing 2 wt% CoO<sub>x</sub> as co-catalyst exhibits under visible light the best photocatalytic activity towards O<sub>2</sub> evolution, obtaining 6.5 mmol of O<sub>2</sub>/g in 5 h.<sup>[143]</sup>

It is worth noticing that although most of the production rates presented in this manuscript are expressed as gas evolution rate by the mass of photocatalysts used, this could be inappropriate since the photocatalytic reaction rate is not proportional to the photocatalyst mass as reported elsewhere.<sup>[144]</sup>

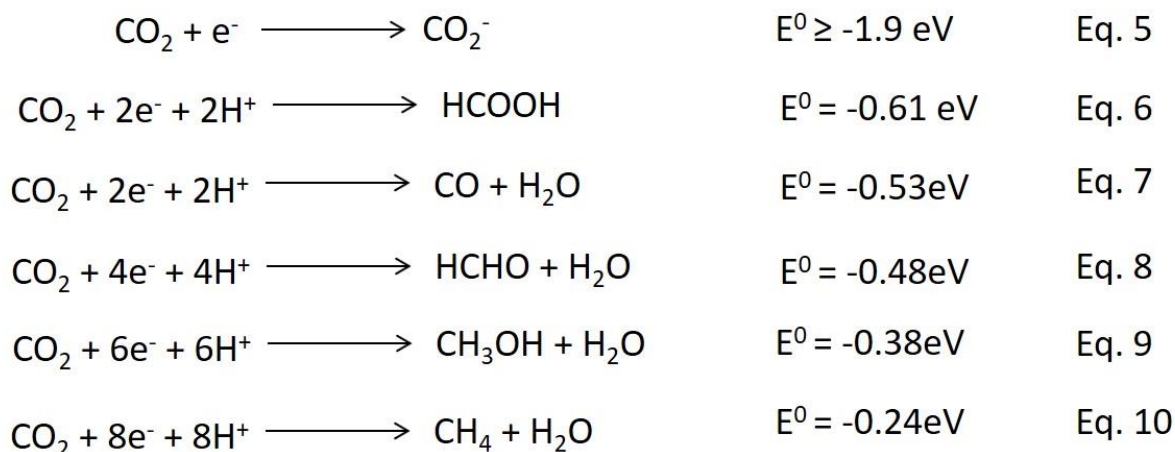
### 3.3 Photocatalytic CO<sub>2</sub> reduction.

Other photocatalytic transformation related to the production of solar fuels that is increasing in interest now-a-days, as consequence of the need to decrease its atmospheric emission, is the photocatalytic CO<sub>2</sub> reduction. Although different technologies, such as photovoltaics or wind power, have emerged in the last decades as clean and renewable procedures to obtain electricity, they have limitations derived from the mismatch between consumption and production due to circadian cycles and random weather conditions. Therefore, this renewable electricity requires the development of suitable energy storage systems. In addition, transportation is based on the use of chemical fuels. For all that reasons, photocatalytic CO<sub>2</sub> reduction to fuels has been proposed as a possible approach to store renewable energy into chemical bonds of organic molecules. Thus, one strategy to decrease CO<sub>2</sub> emissions and store energy is the production of fuels from CO<sub>2</sub>, using solar light irradiation by means of a photocatalyst. One characteristic of these solar fuels derived from CO<sub>2</sub> is that they are in principle CO<sub>2</sub> neutral.

Photocatalytic CO<sub>2</sub> reduction has been typically carried out employing wide band gap semiconductors, forming CO and different products, such as CH<sub>4</sub>, CH<sub>3</sub>OH, HCOOH, HCHO, CH<sub>3</sub>CH<sub>3</sub>, etc. The reaction mechanism of the photocatalytic CO<sub>2</sub> reduction should be similar to the general photocatalytic mechanism indicated in previous sections including light absorption and subsequent photogeneration of electrons and holes in the CB and VB, respectively. The photogenerated electron-hole pair can decay through different recombination pathways or by transferring photogenerated electrons to CO<sub>2</sub>. CO<sub>2</sub> reduction has to occur at the same rate as the oxidation semireaction by holes. In the so-called “artificial photosynthesis”, water is the reagent being oxidized to molecular oxygen. Since it has been already commented that photocatalytic O<sub>2</sub> evolution is a demanding reaction from the kinetic and thermodynamic points of view, it is also very common in photocatalytic CO<sub>2</sub> reduction that evaluation tests use a sacrificial agent better than H<sub>2</sub>O to quench at high rate photogenerated holes, allowing the study of the photocatalytic CO<sub>2</sub> reduction process as the rate determining step.

One important difference between H<sub>2</sub> generation and photocatalytic CO<sub>2</sub> reduction is that the last process can afford different products, the formation of each of them being characterized by a specific reduction potential. The most difficult process is the elementary single-electron CO<sub>2</sub> reduction that requires a very high negative potential. Coupling electron reduction with simultaneous proton transfer makes the process less unfavorable thermodynamically, the higher the number of electrons and protons simultaneously transferred, the lower the thermodynamic potential needed. However, multiple proton-coupled electron transfer (MPCET) has been also determined as rate determining step to CO<sub>2</sub> photoreduction, as consequence of the kinetic competition between the multiple electron and proton transfer and recombination events.

**Equations 5-10** summarize some of the reduction process that are possible from CO<sub>2</sub>.



Therefore, photocatalytic  $\text{CO}_2$  reduction have been found very challenging, and the reported efficiencies are still far from industrial requirements. Very different strategies have been developed in order to enhance the photocatalytic activity towards  $\text{CO}_2$  reduction. Among them, the crystallinity and high surface area of PSC can contribute to improve the photocatalytic activity. In spite of PSCs have been barely explored in this field, very recent examples can be found.<sup>[145]</sup> One of the first examples in the field reports the preparation of  $\text{TiO}_2$  PSC doped with O vacancies,  $\text{Ti}^{+3}$  and OH groups and its efficiency in the photocatalytic  $\text{CH}_4$  production from  $\text{CO}_2$  tested.<sup>[146]</sup> The  $\text{TiO}_2$  PSC was prepared through a hydrothermal method from aqueous mixed solutions containing  $\text{Ti}(\text{C}_4\text{H}_9\text{O})_4$ , HCl and  $(\text{NH}_4)_2\text{TiF}_6$ . These precursors were reacted in autoclave at  $110^\circ\text{C}$  and the resulting solid annealed at temperatures between  $450 - 550^\circ\text{C}$  in air. The obtained  $\text{TiO}_2$  PSC samples presented high  $-\text{OH}$  concentration as well as O vacancies and  $\text{Ti}^{+3}$  defects. Photocatalytic  $\text{CO}_2$  reduction was carried out upon irradiation with a 300 W Xe lamp using  $\text{H}_2\text{O}$  as reducing agent, obtaining  $4 \mu\text{mol}$  of  $\text{CH}_4$  after 6 h reaction. The authors attribute the high photocatalytic activity to the  $\text{CO}_2$  adsorption capacity of the material derived from the O vacancies. In addition, it was proposed that O vacancies and  $\text{Ti}^{3+}$  defects are key to disfavor the recombination of photogenerated charge carriers. It was also claimed that the  $-\text{OH}$  groups on the surface are easier to be reduced than  $\text{H}_2\text{O}$  and, therefore, their presence enhances  $\text{CH}_4$  production. Since the annealing time is a parameter that can optimize the density of surface

–OH groups as well as the O vacancies and  $\text{Ti}^{+3}$  defects, this parameter has to be controlled to maximize  $\text{CH}_4$  production.<sup>[146]</sup>

In another study, TaON PSC microspheres were found suitable photocatalysts for  $\text{CO}_2$  reduction to liquid hydrocarbons upon visible light irradiation.<sup>[147]</sup> Amorphous  $\text{Ta}_2\text{O}_5$  spheres obtained through hydrothermal synthesis were nitrated at high temperature by ammonia vapor to render the porous TaON microspheres. The porous structures played a key role in the photocatalytic  $\text{CO}_2$  conversion to ethanal and ethanol upon visible light irradiation ( $\lambda > 420$  nm). Pt NPs were used as co-catalysts in order to improve the photocatalytic  $\text{CO}_2$  reduction efficiency, increasing ethanol formation rate from 2 to 2.3  $\mu\text{mol/g}\cdot\text{h}$ , while ethanal production rate decreased from 0.5 to 0.4  $\mu\text{mol/g}\cdot\text{h}$ .<sup>[147]</sup>

### 3.4 Use of PSC photocatalysts in selective oxidation reactions.

Photocatalysis has demonstrated to be a useful technology for environmental remediation using sunlight to decompose organic pollutants and a promising strategy for solar fuels production. Other emerging applications in the recent years are aimed at the application of photocatalysis for the synthesis of organic compounds.

One case of these emerging applications is the photocatalytic selective oxidation of organic compounds to form synthetically important organic intermediates. Photocatalysis appears more convenient than conventional oxidation using reagents, since the photocatalytic approach is based on  $\text{O}_2$  activation, avoiding the use of stoichiometric amounts of transition metals ( $\text{Cr}^{\text{VI}}$  salts or  $\text{Mn}^{\text{V}}$  based compounds in strong acidic conditions). In classical oxidation reactions in organic chemistry, the oxidizing reagents are toxic compounds, such as chromates ( $\text{Cr}^{\text{VI}}$ ), which have to be separated from the reaction products and form stoichiometric amounts of by products resulting in a poor atom efficiency. Instead, most of photocatalytic oxidations employ light and

O<sub>2</sub> to promote the oxidation of organic substrates, leaving no residues after removal of the photocatalyst.

The mechanism of photocatalytic oxidations follows again the general pathway commented for environmental remediation, and the reactive oxygen species promote the selective oxidation. Therefore, the general oxidation mechanism starts with CB electrons trapping by molecular oxygen. O<sub>2</sub> is the best electron acceptor when a photocatalyst is operating in ambient conditions. The holes photogenerated are generally consumed by water or can directly oxidize the organic substrate, depending on their relative oxidation potential. The trapping of electrons by oxygen generates superoxide radical (O<sub>2</sub><sup>·-</sup>) as the first reactive oxygen species. Due to its negative charge and basicity, superoxide becomes easily protonated, especially in water at acid or neutral pH values, being rapidly converted into hydroperoxyl (·OOH) radicals. These radicals together with other reactive oxygen radicals derived from them are the key intermediates in selective aerobic oxidations (see **Scheme 20**).

As the previous sections, also in the selective photocatalytic oxidation of organic compounds the activity of TiO<sub>2</sub> PSC exhibiting large surface area and exposing the most active facet has been tested. In this regard, TiO<sub>2</sub> MSC mesocages with preferential {0 0 1} facet have been prepared and its photocatalytic activity towards toluene and cinnamyl alcohol oxidation to their respective aldehydes determined.<sup>[148]</sup> In this study, TiO<sub>2</sub> crystals with SO<sub>4</sub><sup>2-</sup> anions adsorbed preferentially on the {0 0 1} facets were prepared by solvothermal synthesis using TiOSO<sub>4</sub> as precursor in tert-butyl alcohol as solvent. In this synthesis, crystal clusters with the protected {0 0 1} planes were grown. Further growth in autoclave at 110 °C led to TiO<sub>2</sub> PSCs with preferential {0 0 1} facet exposure and disordered mesoporous network. In order to obtain ordered mesoporous TiO<sub>2</sub> single crystals, the TiOSO<sub>4</sub> precursor was confined within SBA-15 or KIT-16 as hard inverse templates for 2D or 3D ordered mesopores, respectively. Finally, template removal resulted in TiO<sub>2</sub> crystals with 2D or 3D ordered network structures. The photocatalytic activity upon UV irradiation (310 nm) towards toluene oxidation (see **Figure**

12) of a series of TiO<sub>2</sub> photocatalysts including commercial Degussa P25, polycrystalline TiO<sub>2</sub>, disordered, 2D ordered and 3D ordered TiO<sub>2</sub> MSC was tested. It was found that the use of MSC photocatalysts enhanced the conversion of toluene to benzaldehyde from near 10 % up to 40 %, approximately. Negligible differences were found for single crystal TiO<sub>2</sub> samples having disordered or 2D or 3D ordered mesoporous structures. However, for larger substrates such as cinnamyl alcohol, the conversion to cinnamaldehyde (see Figure 12) using disordered structures ( $\approx 40\%$ ) was lower than that of 2D ordered mesoporous structures (60%), while the highest conversion was achieved using 3D ordered single crystal TiO<sub>2</sub> mesocages with conversion close to 100%.<sup>[148]</sup>



**Figure 12.** (Top) Synthesis of mesoporous single-crystal-like TiO<sub>2</sub>. 1) Formation TiO<sub>2</sub> crystal clusters with preferential exposure of the (001) planes from component crystals of which (001)

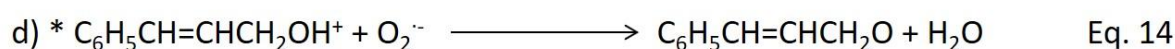
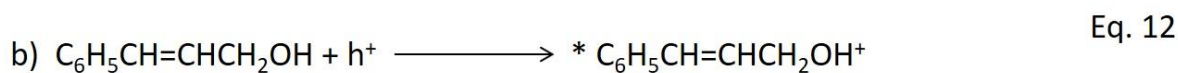


planes were preferably adsorbed with  $\text{SO}_4^{2-}$ . 2) Further attached growth of crystals leading to the formation of single crystals with preferential (001) planes and disordered mesoporous structure. Crystals with ordered mesoporous structure were prepared by a confined growth of the crystals within 3) SBA-15 (mesoporous silica with 2D pore channels) and 4) KIT-6 (mesoporous silica with ordered 3D pore channels) followed by scaffold removal. Reproduced with permission.<sup>[148]</sup> Copyright (2011) American Chemical Society.

(Bottom) Photocatalytic toluene oxidation to benzaldehyde (1) and cinnamyl alcohol to cinnamaldehyde (2) upon UV light irradiation at room temperature. Reaction conditions 100 mg  $\text{TiO}_2$ , 10 mL  $\text{H}_2\text{O}$  and 10  $\mu\text{L}$  of toluene or cinnamyl alcohol.

In a subsequent study, the performance of 2D and 3D nanostructured  $\text{TiO}_2$  single crystal materials was compared with that of polycrystalline  $\text{TiO}_2$  samples prepared using P123 and F127 surfactants as soft-templates for the photocatalytic cinnamyl alcohol oxidation to its respective aldehyde under UV light irradiation.<sup>[149]</sup> Photocurrent experiments demonstrated that nanostructured single crystal  $\text{TiO}_2$  samples prepared with hard templates produced higher photocurrent than those of polycrystalline samples prepared with soft templates. The authors attributed this behavior to differences in the energy levels between the single crystal structures and the polycrystalline samples as consequence of the differences in the crystal phases. Specifically the authors propose that the enhanced percentage of exposed (0 0 1) facets in the single crystal nanostructures having slightly lower band gap energy (3.18 eV) than other facets, such as (1 0 1) (3.22 eV), plays a role in the improved photocurrent generation. In addition, single crystal  $\text{TiO}_2$  exhibiting 3D nanostructure showed higher photocurrent than that of 2D or disordered nanostructures. The higher photocurrent obtained in single crystal  $\text{TiO}_2$  3D nanostructures was attributed to intensified light absorption due to the multiple light reflections present in the 3D nanostructures in comparison with the other single crystal mesoporous structures. The photocatalytic selective oxidation of cinnamyl alcohol to cinnamaldehyde upon

UV light irradiation was also carried out using the single crystal and polycrystalline samples, observing that cinnamyl alcohol conversion using these photocatalysts follows the same trend of the photocurrent intensity. Control experiments based on the addition of reaction quenchers points out to photogenerated electrons and holes as well as  $O_2^{\cdot-}$  radicals as the active species involved in the oxidation reaction. The proposed reaction mechanism is presented in **Equation 11 -14**.<sup>[149]</sup>



In another example of the use of PSC semiconductors as photocatalysts for selective oxidation reactions, CdS PSC nanosheets were used for the photocatalytic aerobic oxidative coupling of amines to imines under visible light irradiation. In this report, diethylenetriamine capped ZnS nanosheets were first synthesized by amine-assisted hydrothermal method. The obtained ZnS nanosheets presented dual role both as precursors and templates for the preparation of the CdS PSC nanosheets through cation exchange treating the ZnS nanosheets with an excess of  $\text{Cd}^{+2}$  cations, obtaining the final nanoporous single crystal CdS nanosheets.<sup>[150]</sup>

The aerobic oxidation of benzylamine to *N*-benzylidene benzylamine was selected as model oxidation to evaluate the photocatalytic activity of single crystal CdS nanosheets (see **Figure 13**). The reaction was carried out in different solvents, being *N,N*-dimethylformamide (DMF) the best, obtaining 99 % conversion and 99 % selectivity under 1 atm of  $O_2$  at room temperature

upon visible light irradiation ( $\lambda > 420$  nm). In comparison, when the catalyst was replaced by CdS NPs the reaction yield decreased to 43 %, demonstrating the superior photocatalytic activity of the CdS PSC nanosheets.<sup>[150]</sup>

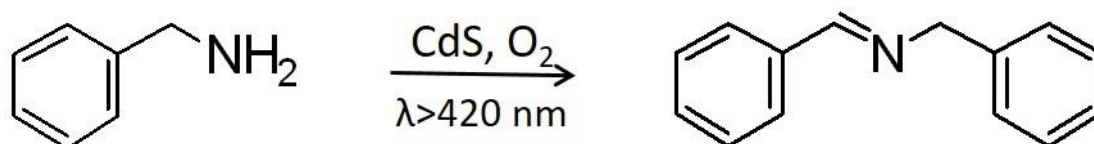


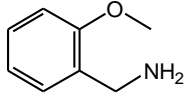
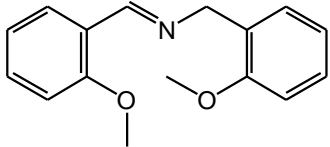
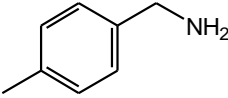
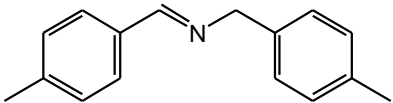
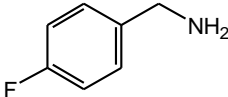
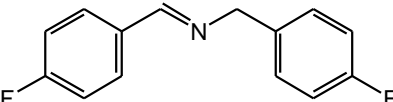
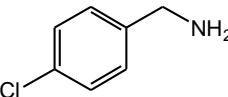
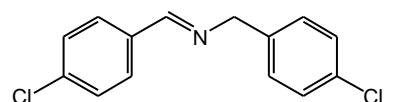
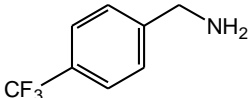
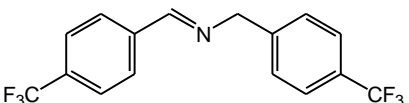
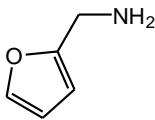
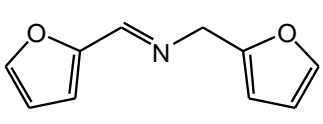
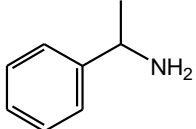
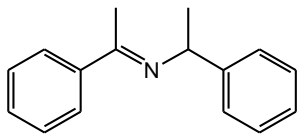
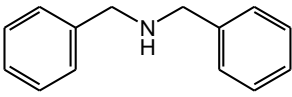
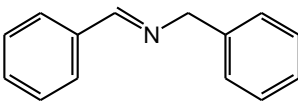
**Figure 13.** Photocatalytic oxidation of benzylamine to N-benzylidene benzylamine using nanoporous single crystal CdS nanosheets as photocatalysts.

The scope of the reaction was screened for different benzylamines using identical conditions, obtaining in most of the cases the expected imine. **Table 1** summarizes the conversion and selectivity obtained for different products using nanoporous single crystal CdS nanosheets as photocatalyst.

**Table 1.** Activity and selectivity data for the photocatalytic aerobic oxidative coupling of benzylamines and the structure of the main product, using CdS PSC nanosheets as photocatalysts under visible light irradiation ( $\lambda > 420$  nm) at room temperature under 1 atm O<sub>2</sub>.

| Substrate | Product | Conversion (%) | Selectivity (%) |
|-----------|---------|----------------|-----------------|
|           |         | 99             | 99              |
|           |         | 78             | 99              |

---

|   |   |    |    |
|---|---|----|----|
|    |    | 48 | 99 |
|    |    | 99 | 99 |
|    |    | 99 | 86 |
|    |    | 99 | 99 |
|    |    | 99 | 99 |
|   |   | 99 | 99 |
|  |  | 35 | 18 |
|  |  | 15 | 99 |

---

The results show that nanoporous single crystal CdS nanosheets are general photocatalysts for the aerobic oxidative coupling of primary benzylamines to imines under visible light irradiation with a wide substrate scope including electron donating as well as electron withdrawing substituents. Moreover, it was found that satisfactory conversion could be obtained under air atmosphere.<sup>[150]</sup> However, as expected in view of the larger steric hindrance,  $\alpha$ -substituted and secondary benzylamines undergo the photocatalytic oxidative coupling to the corresponding imine in much lower yields and selectivity.

Overall the results obtained so far show the general higher photocatalytic activity of PSC semiconductors compared to their polycrystalline analogues, particularly when ordered mesoporosity is also present.

### 3.4. Photovoltaic application

#### 3.4.1 Semiconductor oxides in dye-sensitized solar cells

In the context of a rising energy demand and the on-going shift to renewable energies, the direct transformation of sunlight energy into electricity by means of solar cells is a mature technology. Solar cell production has grown continuously during the last years, the conventional solar cells still being mostly based on silicon. However, due to the drawbacks of silicon metallurgy, there is still much room for improvement in the field of solar cells. For this reason, a very intense research field is focused on the development of new alternative technologies that avoids the use of silicon, such as those based on quantum dots, organic polymers, hybrid organic-inorganic and dye-sensitized solar cells (DSSC). These last types of cells have experienced considerable advances due to the remarkable properties of hybrid lead perovskites <sup>[151]</sup> since these materials have reached certified efficiencies over 23 % <sup>[152]</sup>, although only for a very short period of time. Even though, hybrid organic halide perovskites are widely considered as a potentially commercial technology, two essential points still remain to be satisfactorily solved, i.e., the stability and the use of toxic heavy metals. DSSCs are photoelectrochemical cells composed of a porous layer of a semiconducting metal oxide, adsorbing a molecular dye that acts as light harvester and photosensitizer, immersed in electrolyte solution. The device should have a transparent electrode and a back counter electrode that typically is a thin layer of platinum acting as cathode.

An intense effort during the last decades has been focused on the development of efficient mesoporous semiconductors for their use in DSSC. Again, TiO<sub>2</sub> is by far the most common

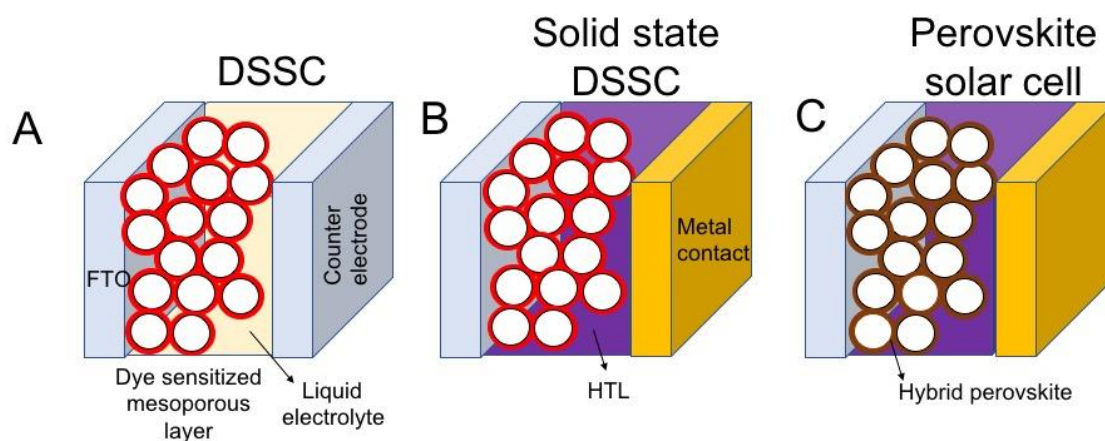
metal oxide used in this type of devices as consequence of its stability, electronic properties or UV photoresponse, besides a being considered as a non-toxic and abundant material.

Nanocrystalline TiO<sub>2</sub> in anatase phase still remains among the best candidate, although many others semiconductors, such as ZnO or SnO<sub>2</sub>, have been also investigated with the aim of increasing the photovoltaic efficiency. One of the main advantages of ZnO and SnO<sub>2</sub> is their superior carrier mobility compared to TiO<sub>2</sub>.

Besides optoelectronic properties, the metal oxide must provide a mesoporous structure necessary not only for a large dye adsorption, but the internal porous network is also crucial to achieve high charge collection efficiency by the electrolyte and suitable electron transport to the electrode. To achieve the goal of an efficient charge transport and collection, an extensive variety of structures have been screened with the aim of obtaining an optimal photocurrent.

The different morphologies that have been evaluated include nanorods,<sup>[153]</sup> nanotubes<sup>[154]</sup>, wires<sup>[155]</sup> or inverse opals.<sup>[156]</sup> Frequently an enhancement of the efficiency of the photovoltaic device with respect to the anatase nanocrystalline particles is observed.<sup>[157]</sup>

Conventional DSSC configurations use a liquid electrolyte with a redox couple to regenerate the dye <sup>[158]</sup>, (see **Scheme 26**). However, due to the drawbacks related to the use of liquid electrolytes related to leakage and evaporation, a new approach has replaced this liquid phase by a solid hole transporting layer (HTL) material (see Scheme 26 B) <sup>[159]</sup>. Spiro-OMeTAD (see structure in **Figure 14**) has been the most commonly used HTL material, although other semiconducting polymers have been employed as well.<sup>[160]</sup> In 2009, Miyasaka et al. first reported the incorporation of hybrid perovskites as sensitizers in DSSCs, but the use of liquid electrolytes restricted the efficiencies of these devices below 5 %.<sup>[161]</sup> Snaith et al. replaced the liquid electrolytes with a solid HTL<sup>[162]</sup>, giving a very promising efficiency of about 10 %<sup>[151, 163]</sup> which currently is over 23 %.<sup>[152]</sup>



**Scheme 26.** Conventional liquid DSSC (A) solid-state DSSC based on the use of HTL (B) and hybrid perovskite solar cell (C) configuration and components.

In the field of photovoltaic cells, the use of single crystals has attracted considerable interest due to the advantages that this structure offer, meeting the photophysical requirements of DSSC in terms of charge transport, electrical conductivity as well as trapping sites density.<sup>[35]</sup> As highlighted previously, MSC structures possess high porosity and a more favorable charge migration compared with films of conventional NPs film.<sup>[164]</sup> In addition, single crystals are also interesting from the point of view of their commercial production since several of the synthesis procedures for PSC are carried out at low temperature, they require one-step only and it is frequently possible to use in a wide range of substrates including flexible supports.

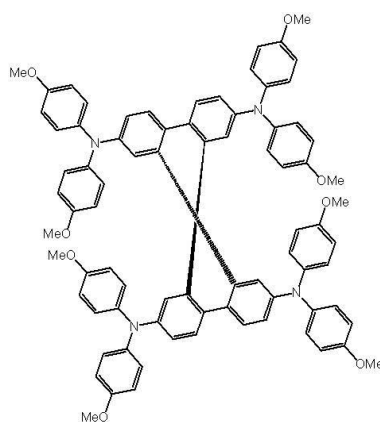


**Figure 14.** Chemical structure of spiro-OMeTAD.

### 3.4.2 Mesoporous TiO<sub>2</sub> single crystals

As an example illustrating the potential advantages of PSC structures over conventional nanocrystals in DSSCs, Snaith et al reported in 2013 a method for the preparation of mesoporous single-crystal TiO<sub>2</sub> anatase as electrode in DSSC.<sup>[165]</sup> This method consists in an initial seed nucleation, followed by a hydrothermal growth, obtaining single crystal TiO<sub>2</sub> at low temperature. In essence, the synthesis was based on the procedure previously reported by Yang et al<sup>[166]</sup> consisting in the use of a packed array of silica beads as hard template. Then, this template is seeded with a solution of TiCl<sub>4</sub>, followed by a hydrothermal treatment with TiF<sub>4</sub> and HF, removing finally the silica template selectively by using a concentrated NaOH solution. It seems that this is a general protocol applicable to the preparation as thin films of a broad range of semiconducting metal oxides with different morphologies of interest in the field of photovoltaics. In addition, the specific surface area of these single crystal materials is very similar to that of commercial TiO<sub>2</sub> NPs (70 m<sup>2</sup>·g<sup>-1</sup>), being this parameter very important to achieve the maximum dye adsorption, thus, high efficiency in the photoresponse of the device.

Moreover, by selecting the diameter of the silica beads used as hard templates, it is possible to control the mesopore size. The dimensions of the pore structure are important in order to optimize, the contact with the liquid electrolyte and, particularly, the easy infiltration of the solid HTL material. As expected, comparison of the electronic mobility shows a superior conductivity of about two or three orders of magnitude of the MSC films with respect mesoporous films prepared from sintered NPs. In addition, all-solid-state DSSCs prepared at 150 °C using the TiO<sub>2</sub> MSC structure deliver a photon-to-current efficiency (PCE) of 3 %, close to the high temperature sintered polycrystalline NPs (PCE of 4.1%) and notably higher than the previous low-temperature all-solid-state DSSC (PCE of 1.30 %).<sup>[167]</sup> It is pertinent to comment here that the use of spiro-OMeTAD as HTL material limits the temperature range in the device preparation and the low temperature values are generally considered among the



main reasons responsible for the lower PCE value of all-solid-state DSSCs due to the poor electrical conductivity among the NPs. Also, the use of flexible transparent electrodes is only possible for low temperature processing methods.

Using the previous single crystal structure and maintaining the silica template, Snaith et al. studied the influence of the annealing temperature (500 to 800 °C) over the electronic properties of TiO<sub>2</sub> PSC.<sup>[15c]</sup> The study revealed that these TiO<sub>2</sub> MSC materials still retain the anatase crystal phase in this range of temperature, in contrast with the behavior of nanocrystalline TiO<sub>2</sub> NPs that undergo a phase transition to rutile. A red shift and a broadening in the absorption spectrum of the TiO<sub>2</sub> were also observed, which was attributed to an increase of oxygen vacancies in the TiO<sub>2</sub> material annealed at high temperatures. These oxygen vacancy defects lead to an increase of electron doping density in the TiO<sub>2</sub>, as indicated in previous studies.<sup>[168]</sup> As a result, an increase of the annealing temperature increases the electrical conductivity and the effective charge carrier mobility of the TiO<sub>2</sub> samples. These beneficial effects are probably due to the oxygen vacancy generation which act as n-doping in the TiO<sub>2</sub>. However, regarding the behaviour of TiO<sub>2</sub> PSC films in a solid-state DSSC, although there is a clear improvement in the performance of the devices increasing the temperature up to 500 °C, further increase of the sintering temperature does not appear to be beneficial and similar efficiencies were observed in the mesoporous layers annealed in the range from 500 to 800 °C. This can be explained since high temperature annealing of TiO<sub>2</sub> increases crystallinity, promotes water desorption and neck growth, which only contribute to electronic transport improvement and, therefore, it is not reflected in the overall device efficiency, affected by the charge transport and other charge transfer processes.<sup>[15c]</sup>

In a different approach, preparation of mesoporous anatase TiO<sub>2</sub> with submicrometer size crystals and nanopores was achieved using a hydrothermal method and combining different carboxylic acids as solvents and additives. This method aims at the control over the

morphology and the inner pores by using carboxylic acids with different chain length (formic acid, acetic acid, octanoic acid and oleic acid).<sup>[169]</sup> Depending on the number of carbon atoms of the carboxylic acids used, mesoporous crystals with different morphologies, size and crystallinity were produced (**Figure 15**). Thus, carboxylic acids of small chain favoured the formation of single crystals with geometries such as octahedra and spindles with oriented subunits. In the case of using carboxylic acid with long carbon chains, formation of spheres with smaller subunit size, increased surface area and reduced crystallinity was observed. A comparative study using these mesoporous crystals as photoelectrodes in DSSCs shows that the single crystal material prepared with acetic acid gives enhanced performance compared to commercial P25. This improved activity was explained considering the adequate pore volume for dye loading and also the favorable electron transport, since single crystal structures provide continuous electron path without boundaries and also with less structural defects which are known to act negatively as charge recombination centres.

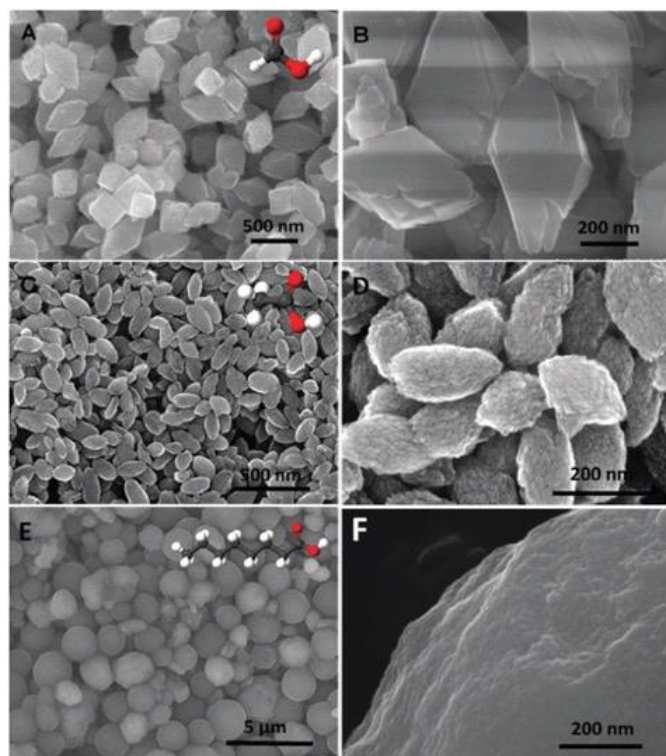


**Figure 15.** SEM images of the different mesoporous anatase  $\text{TiO}_2$  crystals obtained by employing in their synthesis different carboxylic acids: (A, B) formic acid, (C, D) acetic acid

and (E, F) octanoic acid. The insets show the corresponding carboxylic acid employed.

Reproduced with permission.<sup>[169]</sup> Copyright (2014) Royal Society of Chemistry.

Another positive effect related to the use of mesoporous TiO<sub>2</sub> single crystals in the photoanode of DSSCs as light-scattering layer has been proposed. The role of the scattering layer is minimization of light reflexion by the DSSC surface, thus, favoring photon absorption by the photoactive layer. For instance, Xu et al. presented a new TiO<sub>2</sub> structure formed for mesoporous microspheres with mesoporous TiO<sub>2</sub> polyhedra on the outer shell.<sup>[170]</sup> In addition, this MSC structure has preferential crystallographic {101} orientation for the facets, due to the use of fluoride ions during the hydrothermal synthesis. It was observed that, this new layer improved the conversion efficiency in a 27 % with respect to the DSSC containing P-25 alone, and this efficiency improvement was explained by the enhanced light trapping caused by the scattering effect of the mesoporous TiO<sub>2</sub> single crystal layer.

### 3.4.3 TiO<sub>2</sub> mesocrystals

Other type of ordered superstructures called mesocrystals was proposed by Colfèn and Antonietti.<sup>[171]</sup> Mesocrystals are characterized by highly parallel crystallization and controlled alignment of independent NP building blocks. As an example of mesocrystals, a new mesoporous TiO<sub>2</sub> mesocrystals with olive-shaped morphology has been applied in DSSC.<sup>[35]</sup> The preparation method is based on selective evaporation of a solvent, causing reorganization and self-assembly of a lyotropic polymer. Thus, PEO–PPO–PEO triblock copolymers were used in combination of two cosolvents with different boiling point, followed by preferential slow evaporation at low temperature. The mesoporous 3D mesocrystals of TiO<sub>2</sub> obtained termed as FDU-19 have anisotropy, very uniform size and preferential facet orientation. After calcination at 350 °C, the samples contained high concentration of oxygen

vacancies ( $\text{Ti}^{+3}$  sites) and reached surface area values up to  $189 \text{ m}^2/\text{g}$ . Moreover, transformation of these oxygen vacancies in defect-free mesoporous anatase single crystal having opened mesopore channels through the whole particles was possible to be achieved by thermal annealing in air. In addition, annealing the FDU-19 sample in vacuum at  $400 \text{ }^\circ\text{C}$  promoted the transformation of the 3D olive-shaped structure into ultrathin anatase single crystal nanosheets with 90 % exposed reactive (001) facets and large amount of oxygen vacancies.

DSSCs prepared with the mesoporous  $\text{TiO}_2$  mesocrystals without and with air annealing exhibit much high current densities compared with P25. All the mesoporous  $\text{TiO}_2$  mesocrystals yielded high power conversion efficiencies up to 11.6 % that is about the record for this type of DSSC devices. This high efficiency was attributed to the single crystal nature and high porosity of the materials. Thus, the dye loading capacity, one of the key features to reach high efficiency, was 5 times higher than that of commercial P25 and impedance spectroscopy studies confirmed the lower recombination rate and fast electron transfer through the mesoporous  $\text{TiO}_2$  mesocrystals.

Other approach for the preparation of mesoporous anatase single crystal with ellipsoidal shape and polyhedral pores was based on a one-step hydrothermal route without the use of additives or templates.<sup>[172]</sup> Basically, the process consists in a hydrothermal treatment of a solution of titanium butoxide in acetic acid and their subsequent calcination at  $500 \text{ }^\circ\text{C}$ . The precipitate formed during the hydrothermal step shows ellipsoid-shaped particles with 190 nm long and 100 nm wide dimensions. Formation of anatase  $\text{TiO}_2$  crystals was confirmed using electron diffraction (ED) and X-ray diffraction (XRD).

The mesoporous anatase single crystals prepared by hydrothermal route in the absence of additives were used to build photovoltaic devices whose activity was compared with that of analogous DSSC prepared using commercial Dyesol  $\text{TiO}_2$  paste, and employing the redox couple  $\text{Co}^{(2+/3+)}$  as electrolyte and MK-2 organic dye as sensitizer. Under these conditions the

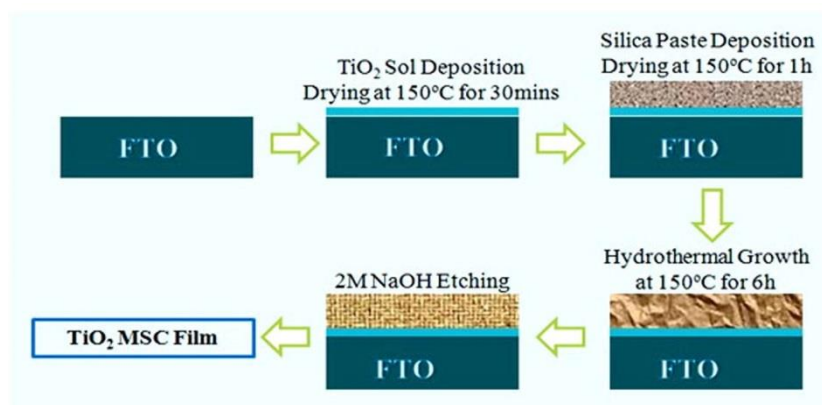
crystalline mesoporous structure shows better light harvesting properties, even though dye loading was 20 % lower. The higher light harvesting property was justified proposing the operation of a scattering effect in the case of the mesoporous structure. In addition, the photovoltaic devices prepared with the mesoporous anatase single crystals exhibited a clear improvement in the photovoltaic efficiency showing photon-to-electron conversion efficiencies up to 8.7 %, due also to the good electronic connectivity throughout the whole single crystal material.

In a different approach, the use of single-crystalline TiO<sub>2</sub> as electron transporting layer (ETL) in planar perovskite solar cells has been reported.<sup>[13]</sup> Considering the limitations of defective TiO<sub>2</sub> commonly prepared by spin-coating as ETL material, Choi et al. proposed other alternative procedure to prepare this ETL that forms single crystal structure, removing the defects and improving light transmittance as well as the contact area between the perovskite and the TiO<sub>2</sub> layer.<sup>[13]</sup> The method proposed consists in the preparation of a thin layer of metallic titanium by sputtering and their posterior oxidation by electrochemical anodization. Finally, in order to reach good crystallinity, the film was thermally annealed at 500 °C. Using this procedure, the authors demonstrate that the power conversion efficiency can increase up to 22 %.

On the other hand, anatase PSC can be prepared directly on arbitrary substrates. This strategy can have the advantage that can be used on substrates that physically have a better structural coherence for a given phase of TiO<sub>2</sub>, allowing an enhanced connectivity between the substrate and the semiconductor due to the match between the facets of the two materials in contact. This better connectivity between TiO<sub>2</sub> and the substrate results in a high electrical conductivity and favours the electron mobility across the junction compared with conventional deposited films. In one example of this approach, Yu et al. demonstrated the direct growth of TiO<sub>2</sub> on FTO substrates at low temperature (150 °C) with an immediate application in DSSC.<sup>[164]</sup> The method consists in an initial seeded nucleation, followed by

silica paste template deposition by screen printing. Subsequent hydrothermal growth of  $\text{TiO}_2$  was carried out in autoclave, and finally the silica template was removed by selective etching.

**Scheme 27** illustrates the preparation procedure.



**Scheme 27.** Preparation procedure of  $\text{TiO}_2$  MSC nanosheets on FTO electrodes. Reproduced with permission.<sup>[164]</sup> Copyright (2016) Elsevier.

A proof of the enhanced electronic properties of the resulting single crystal  $\text{TiO}_2$  nanosheets is their use in DSSC, where the authors claimed a record efficiency for sub-150 °C processing of about 6 %.<sup>[164]</sup>

Even though it is well demonstrated that single crystal  $\text{TiO}_2$  films enhance the electrical conductivity and charge transport properties, some limitations derived from the random crystalline orientation and the grain boundary interactions still remain. Recently, Li et al. addressed this limitation preparing uniaxially oriented mesoporous anatase  $\text{TiO}_2$  films on FTO substrates.<sup>[173]</sup> To obtain oriented single crystal  $\text{TiO}_2$ , the authors used the typical hydrothermal method employing titanium butoxide as  $\text{TiO}_2$  precursor, but controlling the concentration of  $\text{SO}_4^{2-}$  and  $\text{Cl}^-$  during the growth. It has been well documented that depending on the  $\text{SO}_4^{2-}$  or  $\text{Cl}^-$  concentration formation of anatase or rutile phase  $\text{TiO}_2$  can be favoured, respectively.<sup>[174]</sup> As a result, as-prepared mesoporous anatase film showed an intense (004) diffraction peak which is indicative of the high degree of crystallinity, together with the uniaxially oriented anatase  $\text{TiO}_2$  film along the (001) direction (**Figure 16**). Moreover, the

mesoporous structures show uniformly distributed mesopores of 5-10 nm. Finally, the superior charge transport properties (100 fold enhancement) were demonstrated using intensity-modulated photocurrent/photovoltage spectroscopy. This uniaxial oriented mesoporous TiO<sub>2</sub> film with such remarkable electronic properties has an immediate application in photovoltaics and other related fields.

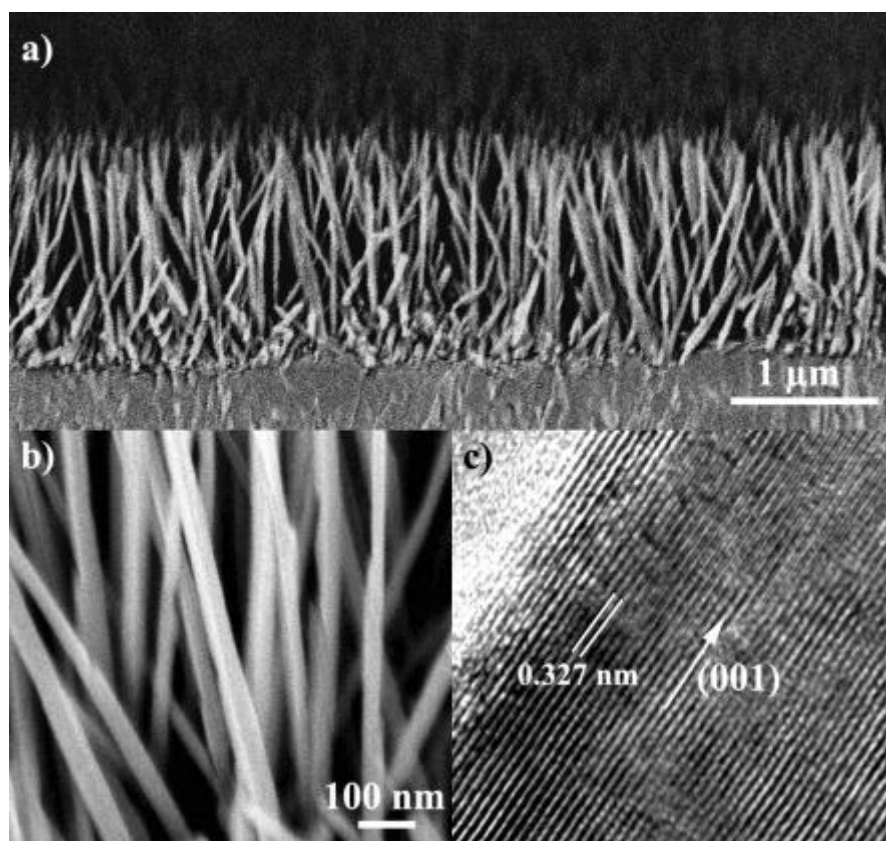


**Figure 16.** FESEM images (a and b) uniaxially oriented anatase TiO<sub>2</sub> film of nanowires along the (001) direction. (c) HRTEM of a single nanowire. Reproduced with permission.<sup>[174b]</sup>

Copyright (2012) John Wiley and Sons.

Considering that the optimal thickness required in mesoscopic perovskite solar cells is only several hundred nanometers, the use of mesoporous single crystal anatase which normally exhibits a relatively large size is not suitable. In addition, those preparation methods based on hard templated-assisted synthesis<sup>[165-166]</sup> are not appropriate for common large area manufacturing procedures such as screen printing and coating techniques. Therefore, in the

case of perovskite solar cells it is necessary to use single crystal anatase particles with nanometric size in combination with compatible fabrication methods. To solve these issues, Xiong et al.<sup>[16d]</sup> develop a simple evaporation method<sup>[35]</sup>, consisting in mixing in different steps THF, Pluronic 127, H<sub>2</sub>O, HCl, acetic acid and titanium tetrabutoxide and finally drying and sintering. The obtained mesoporous anatase single crystals have a large surface area of 169 m<sup>2</sup>/g, olive shape with about 120 nm length, 60 nm width and a pore size about 8 nm. In addition, XRD characterization shows that the material exhibits a highly crystalline anatase phase. This particle morphology favours the incorporation of the perovskite material in the matrix. The use of this perovskite-anatase single crystal as electron transport material in mesoscopic perovskite solar cells result in a 25 % improvement of PCE compared with P25 solar cells. Photoluminescence and impedance spectroscopy demonstrate that this improvement derives from a fast electron extraction and a slower recombination. Therefore, the influence of MSC anatase is other example of the potential of the use of small sized single crystals in the field of photovoltaics.

#### *3. 4. 4 Other MSC materials*

Following the strategy of Snaith et al.<sup>[165]</sup> using silica-templated hydrothermal method to grow TiO<sub>2</sub>, mesoporous SnO<sub>2</sub> single crystals have also been prepared for their application in perovskite photovoltaic cells.<sup>[175]</sup> Considering the good charge mobility and the lower trap density characteristic of SnO<sub>2</sub>, this type of semiconductor is a promising candidate for charge collection. However preliminary results using SnO<sub>2</sub> single crystal showed that the efficiency of the device was low, due to the occurrence of charge recombination which limits the device photovoltage and photocurrent. A typical strategy generally used to reduce charge recombination is to cover the mesoporous structure with a thin compact layer of TiO<sub>2</sub>.<sup>[176]</sup> Following this strategy, it was possible to increase the efficiency of the devices from 3 to 7 %,



a value much higher than previous results using mesoporous TiO<sub>2</sub> single crystals<sup>[165]</sup> and hybrid perovskites as light harvester. Electrochemical impedance spectroscopy was used to investigate the interfacial charge transfer at the SnO<sub>2</sub>/CH<sub>3</sub>NH<sub>3</sub>PbI<sub>3</sub>/spiro-OMeTAD interfaces, showing that the recombination rate follows the trend SnO<sub>2</sub> > TiO<sub>2</sub>-coated SnO<sub>2</sub> > TiO<sub>2</sub> nanocrystals. Therefore, SnO<sub>2</sub> is a promising semiconductor due to the better electron transport properties, although it is necessary to suppress the interfacial charge recombination to achieve the optimal performance.

Similarly, ZnO based photoelectrodes have also been widely studied in photovoltaic applications. The interest in this semiconductor arises from the similarity of ZnO band gap with that of the TiO<sub>2</sub> and the easier electron migration in ZnO compared to TiO<sub>2</sub> (more than one order of magnitude larger than anatase).<sup>[177]</sup>

In this context, nanostructured ZnO with different morphologies have been investigated as photoanodes in DSSC.<sup>[177a]</sup> However, the efficiency of these devices has not yet achieved that of the corresponding TiO<sub>2</sub> photoanodes. Similarly to the SnO<sub>2</sub> case, the faster charge recombination kinetics in ZnO compared to TiO<sub>2</sub> has been found responsible for the lower performance of these photoelectrodes. Different approaches have been developed trying to overcome this limitation. Thus, Qiu et al. reported the preparation by hydrothermal synthesis of ZnO PSC nanoplatelets for their use in DSSCs.<sup>[45]</sup> The synthesis of single crystal ZnO nanoplatelets includes the formation and decomposition of the nanoscale plate-like Zn<sub>5</sub>(CO<sub>3</sub>)<sub>2</sub>(OH)<sub>6</sub> precursor. The formation step is based on the conglomeration of oriented precursor building blocks, while the decomposition results in ZnO nanoplatelets with abundant porosity. Photoanodes of as-prepared ZnO PSC nanoplatelets for DSSC reached a power conversion efficiency of 5 %, which was found higher than those of nanoparticulate based ZnO DSSC studied so far. The efficiency improvement was attributed to the increase in dye loading, enhanced light scattering and, specially, increased electron lifetime. These ZnO PSC nanoplatelets have been proposed as good candidates for the development of efficient

DSSCs. It was suggested that further control of the nanoplatelet pore size could give rise to more efficient devices, but this proposal still has to be proved.

Chem et al. reported the synthesis of ZnO microflowers exhibiting hierarchical structures.<sup>[58]</sup>

These structures presented interlaced PSC nanosheets. Similarly to conventional preparation methods, these hierarchical structures can be conveniently synthesized at room temperature by direct precipitation of a soluble zinc salt in alkaline solution. The obtained microflowers presented uniform spherical morphology with diameters between 1 to 3  $\mu\text{m}$  (**Figure 17**).

Quasi-solid state DSSCs were fabricated using the ZnO microflower hierarchical structures, reaching power conversion efficiencies of 4.1 %. These efficiency values were found much higher than those obtained with nanoparticulated ZnO photoelectrodes. Experimental evidence supports that this performance improvement of these single crystal ZnO structures derives from enhanced surface area, better light scattering and higher charge transport than in the case of the ZnO NPs as photoactive components in photoanodes.

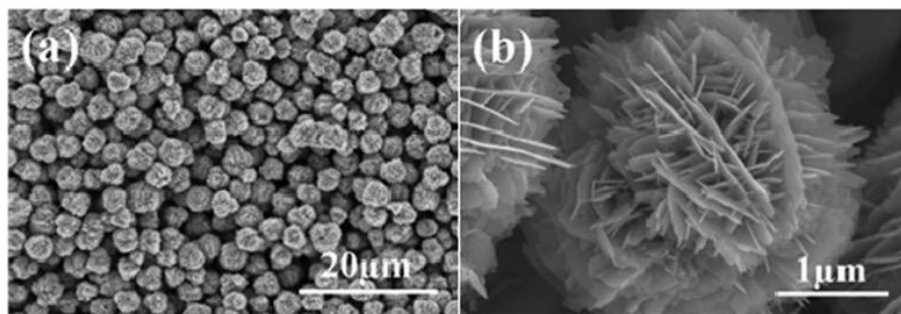


**Figure 17.** SEM image of ZnO microflowers exhibiting hierarchical structure (a) and a magnified image of an individual microflower (b). Reproduced with permission.<sup>[58]</sup> Copyright (2011) Royal Society of Chemistry.

The search for hierarchical structures able to improve the performance of ZnO based photoanodes in DSSCs lead to the hydrothermal synthesis of porous nanosheet assembled ZnO microspheres.<sup>[44]</sup> After calcination of these single crystal ZnO, photoanodes for DSSC were built. The authors found that these single crystal ZnO microspheres presented a superior

performance (5 %) than nanosheet-assembled ZnO microflowers (4 %), porous dispersed ZnO nanosheets (3 %) and other previously reported ZnO nanostructures. Among the reasons for this improved performance of PSC nanosheet assembled ZnO microspheres, the two major ones were proposed to be efficient light scattering of the hierarchical ZnO microspheres and the higher surface area which optimizes dye adsorption. Besides, the single crystal nature of the ZnO nanosheets enhances charge transport along the microspheres and the interfacial contact among adjacent spheres increasing the electron transport, reducing the series resistance in the photoanode. Finally, the spherical assemblies form large interstitial pores providing efficient electrolyte diffusion through the ZnO layer.

One of the weakest points found in the use of ZnO in photoanodes for DSSC is the chemical instability of ZnO in the presence of acidic dyes required for sensitization that results in the chemical degradation of the ZnO substrate to  $Zn^{2+}$  and dye desorption under some conditions. Another issue to be avoided is dye aggregation that typically requires short adsorption times and the use of reasonably diluted solutions. In one example addressing these issues, De Marco et al.<sup>[178]</sup> reported the synthesis of  $ZnS \cdot (ethylenediamine)_{0.5}$  nanosheets by solvothermal method and subsequent calcination to obtain single crystal ZnO platelets with pore size distribution between 10 to 30 nm. The as-prepared ZnO platelets presented enhanced surface area with large interstitial voids, whose coarse porosity allowed fast and efficient dye loading as well as reduced interfacial charge recombination. Optimization of the size of single crystal ZnO platelets gave rise to power conversion efficiencies of up to 5.6 %.

In summary, there is abundant experimental evidence showing that the use of single crystal metal oxides in the preparation of photoanodes, both in DSSCs and hybrid perovskite solar cells, **could** improve the efficiency of these devices compared to the use typical polycrystalline NP metal oxides. The origin of this improvement seems to derive from the combination of several factors including larger charge carrier mobility and charge diffusion length, better light scattering properties and higher surface area allowing higher dye loadings. **However, it is worth**

noticing that the overall efficiencies of devices containing PSCs layers have not reach that of nanocrystalline based devices. Among the different reasons for this mismatch, it should be commented that the improvement in some factors such as charge transport or dye loading could, alternatively, have detrimental effects in other parameters, such as the charge recombination, among others, affecting negatively the devices overall efficiency. For that reason, further optimization of device components (dye loading, electrolyte composition, PSC layer thickness, etc.) must be carried out when PSCs are used instead of the traditional nanocrystalline layers in order to keep balanced all parameters while charge transport and dye loading are improved, and thus, obtaining larger efficiencies.

As in other related areas  $\text{TiO}_2$  has been the most preferred semiconductor for the construction of photoanodes for photovoltaics. In every example reported, the use of PSC structures has demonstrated a superior conductivity with respect to mesoporous films composed by polycrystalline NPs. The objective of the synthetic strategies carried out to develop complex PSC hierarchical structures is to favor electron migration minimizing charge recombination, maximization of light scattering and the increase of the specific surface area and therefore dye loading, The combination of all these favorable properties found in PSC make advisable further research in this area directed to the simultaneous optimization of every parameter playing a role on the performance of the device to reach the highest possible efficiency, overcoming, if possible, the actual limit in DSSC about 12 %.

#### **4. Conclusions**

The present review has shown the various possible strategies that have been developed for the reliable synthesis of PSCs with different morphologies and controlled pore dimensions. Particularly in the case of metal oxides, it has been shown that these synthetic protocols can be applied with minor adjustments to a wide range of materials and even to the preparation of some

semiconducting salts. Thus, metal sulfides can also be prepared as PSCs. Further research in this area should focus on the development of analogous procedures for other semiconductors and on increasing the compatibility of PSC preparation with the use of reactive and flexible substrates, improving interfacial contact with substrates.

It has been shown that the combination of single crystal structuring allowing fast charge migration, long free migration path and high electrical conductivity, together with porosity increasing surface area, density of available sites and adsorption capacity are all favorable effects for the optoelectronic response. As result, PSC materials exhibit an improved performance respect to nanoparticulate materials for every application in photocatalysis from environmental remediation to the production of solar fuels or chemical and in photovoltaics. This is a remarkable result, since small NPs have been considered in some cases as the most efficient photoactive materials and, therefore, the present review has shown ways to surpass their activity.

Since most of the studies have dealt with TiO<sub>2</sub>, further research is needed to apply the PSC benefits to novel visible light semiconductors such metal organic frameworks, hybrid organic lead perovskites and even metal-free semiconductors. The preparation as PSC of hybrid organic lead perovskites should be particularly important in the field of photovoltaics, since the most recent progress on perovskite solar cells have decreased the interest for DSSCs. In this area, there is a clear gap in applying the PSC approach to hybrid perovskites trying to further increase their conversion efficiency and, hopefully, the durability of these devices.

Thus, it can be anticipated that the field of PSCs that has only recently started will grow and expand in the near future, becoming a routine methodology in the area of photocatalysis and photovoltaics. This methodology could eventually serve to develop more efficient solar light photocatalysts reaching the required specifications for a commercial photocatalytic water splitting or CO<sub>2</sub> reduction process. PSC should also have impact in development of commercial silicon-free solar cells.

**Acknowledgements**

Financial support by the Spanish Ministry of Economy and Competitiveness (Severo Ochoa SEV2016-0683, and RTI2018-89023-CO2-R1) and by the Generalitat Valenciana (Prometeo 2017-083) is gratefully acknowledged.

Received: ((will be filled in by the editorial staff))

Revised: ((will be filled in by the editorial staff))

Published online: ((will be filled in by the editorial staff))

**References**

- [1] B. Lee, T. Yamashita, D. Lu, J. N. Kondo, K. Domen, *Chemistry of Materials* **2002**, 14, 867.
- [2] E. J. W. Crossland, N. Noel, V. Sivaram, T. Leijtens, J. A. Alexander-Webber, H. J. Snaith, *Nature* **2013**, 495, 215.
- [3] G. Liu, H. G. Yang, J. Pan, Y. Q. Yang, G. Q. Lu, H. M. Cheng, *Chemical Reviews* **2014**, 114, 9559.
- [4] a) X. Zheng, Y. Lv, Q. Kuang, Z. Zhu, X. Long, S. Yang, *Chemistry of Materials* **2014**, 26, 5700; b) W. Jiao, Y. P. Xie, R. Z. Chen, C. Zhen, G. Liu, X. L. Ma, H. M. Cheng, *Chemical Communications* **2013**, 49, 11770; c) W. Q. Fang, Z. Huo, P. Liu, X. L. Wang, M. Zhang, Y. Jia, H. Zhang, H. Zhao, H. G. Yang, X. Yao, *Chemistry - A European Journal* **2014**, 20, 11439.
- [5] a) Z. Bian, J. Zhu, J. Wen, F. Cao, Y. Huo, X. Qian, Y. Cao, M. Shen, H. Li, Y. Lu, *Angew Chem Int Ed Engl* **2011**, 50, 1105; b) S. Cho, S. Kim, D. W. Jung, K. H. Lee, *Nanoscale* **2011**, 3, 3841; c) G. Xu, S. Deng, Y. Zhang, X. Wei, X. Yang, Y. Liu, G. Shen, G. Han, *CrystEngComm* **2014**, 16, 2025.
- [6] a) X. Wei, G. Xu, Z. H. Ren, C. X. Xu, W. J. Weng, G. Shen, G. R. Han, *Journal of the American Ceramic Society* **2010**, 93, 1297; b) Z. Hong, K. Zhou, Z. Huang, M. Wei, *Scientific Reports* **2015**, 5, 11960.
- [7] R.-Q. Song, H. Cölfen, *Advanced Materials* **2010**, 22, 1301.
- [8] a) B. M. Weckhuysen, J. Yu, *Chemical Society Reviews* **2015**, 44, 7022; b) N. Rangnekar, N. Mittal, B. Elyassi, J. Caro, M. Tsapatsis, *Chem. Soc. Rev.* **2015**, 44, 7128.
- [9] a) Q. Wu, S. Bao, B. Tian, Y. Xiao, J. Zhang, *Chemical Communications* **2016**, 52, 7478; b) J. Niu, S. Shen, L. Zhou, Z. Liu, P. Feng, X. Ou, Y. Qiang, *RSC Advances* **2016**, 6, 62907.
- [10] D. Lu, S. Ouyang, H. Xu, D. Li, X. Zhang, Y. Li, J. Ye, *ACS Applied Materials and Interfaces* **2016**, 8, 9506.
- [11] S. Jiang, J. Zhang, X. Qi, M. He, J. Li, *CrystEngComm* **2013**, 15, 9837.
- [12] a) H. Liu, X. L. Chen, S. C. Yan, Z. S. Li, Z. G. Zou, *Eur. J. Inorg. Chem.* **2014**, 23, 3731; b) C. Li, G. Chen, J. Sun, J. Rao, Z. Han, Y. Hu, Y. Zhou, *ACS Appl Mater Interfaces* **2015**, 7, 25716.
- [13] J. Choi, S. Song, M. T. Hörantner, H. J. Snaith, T. Park, *ACS Nano* **2016**, 10, 6029.
- [14] a) Y. Yu, J. Zhang, X. Wu, W. Zhao, B. Zhang, *Angewandte Chemie - International Edition* **2012**, 51, 897; b) W. W. Zhao, C. B. Liu, L. M. Cao, X. G. Yin, H. Xu, B. Zhang, *Rsc Advances* **2013**, 3, 22944.
- [15] a) J. Liu, Z.-Y. Hu, Y. Peng, H.-W. Huang, Y. Li, M. Wu, X.-X. Ke, G. V. Tendeloo, B.-L. Su, *Applied Catalysis B: Environmental* **2016**, 181, 138; b) J. Niu, S. Shen, S.

- He, Z. Liu, P. Feng, S. Zhang, X. Ou, Y. Qiang, Z. Zhu, *Ceramics International* **2015**, 41, 11936; c) V. Sivaram, E. J. W. Crossland, T. Leijtens, N. K. Noel, J. Alexander-Webber, P. Docampo, H. J. Snaith, *The Journal of Physical Chemistry C* **2014**, 118, 1821.
- [16] a) J. N. Kondo, Y. Takahara, B. Lee, D. L. Lu, K. Domen, *Topics in Catalysis* **2002**, 19, 171; b) H. Jiang, X. Meng, H. Dai, J. Deng, Y. Liu, L. Zhang, Z. Zhao, R. Zhang, *Journal of Hazardous Materials* **2012**, 217-218, 92; c) Y. Liu, Y. Luo, A. A. Elzatahry, W. Luo, R. Che, J. Fan, K. Lan, A. M. Al-Enizi, Z. Sun, B. Li, Z. Liu, D. Shen, Y. Ling, C. Wang, J. Wang, W. Gao, C. Yao, K. Yuan, H. Peng, Y. Tang, Y. Deng, G. Zheng, G. Zhou, D. Zhao, *ACS Cent Sci* **2015**, 1, 400; d) Y. Xiong, Y. Liu, K. Lan, A. Mei, Y. Sheng, D. Zhao, H. Han, *New Journal of Chemistry* **2018**, 42, 2669; e) K. Girija, S. Thirumalairajan, A. K. Patra, D. Mangalaraj, N. Ponpandian, C. Viswanathan, *Semicond. Sci. and Technol.* **2013**, 28, 035015; f) H. Liu, M. Luo, J. Hu, T. Zhou, R. Chen, J. Li, *Applied Catalysis B: Environmental* **2013**, 140-141, 141; g) Y. Qiu, G. L. Xu, Q. Kuang, S. G. Sun, S. Yang, *Nano Research* **2012**, 5, 826; h) H. G. Cha, S. J. Kim, K. J. Lee, M. H. Jung, Y. S. Kang, *Journal of Physical Chemistry C* **2011**, 115, 19129.
- [17] a) S. Bharathi, D. Nataraj, D. Mangalaraj, Y. Masuda, K. Senthil, K. Yong, *Journal of Physics D: Applied Physics* **2010**, 43, 015501; b) A. Liao, H. He, L. Tang, Y. Li, J. Zhang, J. Chen, L. Chen, C. Zhang, Y. Zhou, Z. Zou, *ACS Applied Materials and Interfaces* **2018**, 10, 10141; c) L. Li, Y. Yu, F. Meng, Y. Tan, R. J. Hamers, S. Jin, *Nano Letters* **2012**, 12, 724; d) T. Xu, H. Zheng, P. Zhang, W. Lin, Y. Sekiguchi, *Journal of Materials Chemistry A* **2015**, 3, 19115; e) T. Xu, H. Zheng, P. Zhang, W. Lin, *RSC Adv.* **2016**, 6, 95818; f) Y. C. Liu, S. H. Shen, F. Ren, J. N. Chen, Y. M. Fu, X. D. Zheng, G. X. Cai, Z. Xing, H. Y. Wu, C. Z. Jiang, *Nanoscale* **2016**, 8, 10642.
- [18] X.-Y. Yang, L.-H. Chen, Y. Li, J. C. Rooke, C. Sanchez, B.-L. Su, *Chem. Soc. Rev.* **2017**, 46, 481.
- [19] A. Stein, F. Li, N. R. Denny, *Chem. Mat.* **2008**, 20, 649.
- [20] E. Yamamoto, K. Kuroda, *Bul. Chem. Soc. Jap.* **2016**, 89, 501.
- [21] a) J. Li, H. Chang, L. Ma, J. Hao, R. T. Yang, *Catalysis Today* **2011**, 175, 147; b) B. Ilić, S. G. Wettstein, *Micropor. Mesopor. Mat.* **2017**, 239, 221.
- [22] a) X. Zheng, Q. Kuang, K. Yan, Y. Qiu, J. Qiu, S. Yang, *ACS Appl Mater Interfaces* **2013**, 5, 11249; b) Y. Zhou, Q. Yi, M. Xing, L. Shang, T. Zhang, J. Zhang, *Chemical Communications* **2016**, 52, 1689; c) C. Dong, H. Song, Y. Zhou, C. Dong, B. Shen, H. Yang, M. Matsuoka, M. Xing, J. Zhang, *RSC Adv.* **2016**, 6, 77863; d) M. Xing, Y. Zhou, C. Dong, L. Cai, L. Zeng, B. Shen, L. Pan, C. Dong, Y. Chai, J. Zhang, Y. Yin, *Nano Letters* **2018**, 18, 3384.
- [23] a) Z. L. Zhu, X. L. Zheng, Y. Bai, T. Zhang, Z. L. Wang, S. Xiao, S. H. Yang, *Physical Chemistry Chemical Physics* **2015**, 17, 18265; b) Y. Wang, Y. Deng, L. Fan, Y. Zhao, B. Shen, D. Wu, Y. Zhou, C. Dong, M. Xing, J. Zhang, *RSC Advances* **2017**, 7, 24064.
- [24] C. W. Wang, S. Yang, W. Q. Fang, P. Liu, H. Zhao, H. G. Yang, *Nano Letters* **2016**, 16, 427.
- [25] G. Liu, J. C. Yu, G. Q. Lu, H. M. Cheng, **2011**, 47, 6763.
- [26] X. Chen, S. S. Mao, *Chem. Rev.* **2007**, 107, 2891.
- [27] W.-J. Ong, L.-L. Tan, S.-P. Chai, S.-T. Yong, A. R. Mohamed, *Nanoscale* **2014**, 6, 1946.
- [28] H. G. Yang, C. H. Sun, S. Z. Qiao, J. Zou, G. Liu, S. C. Smith, H. M. Cheng, G. Q. Lu, *Nature* **2008**, 453, 638.
- [29] T. Wu, X. Kang, M. W. Kadi, I. Ismail, G. Liu, H. M. Cheng, *Cuihua Xuebao/Chinese Journal of Catalysis* **2015**, 36, 2103.

- [30] H. Yu, L. Wang, M. Dargusch, *Solar Energy* **2016**, 123, 17.
- [31] C. Zhen, T. Wu, M. W. Kadi, I. Ismail, G. Liu, H. M. Cheng, *Cuihua Xuebao/Chinese Journal of Catalysis* **2015**, 36, 2171.
- [32] J. Wang, Z. Bian, J. Zhu, H. Li, *J. Mater. Chem. A* **2013**, 1, 1296.
- [33] W. Yue, C. Randorn, P. S. Attidekou, Z. Su, J. T. S. Irvine, W. Zhou, *Advanced Functional Materials* **2009**, 19, 2826.
- [34] V. Malgras, Q. Ji, Y. Kamachi, T. Mori, F. K. Shieh, K. C. W. Wu, K. Ariga, Y. Yamauchi, *Bul. Chem. Soc. Jap.* **2015**, 88, 1171.
- [35] Y. Liu, Y. Luo, A. A. Elzatahry, W. Luo, R. Che, J. Fan, K. Lan, A. M. Al-Enizi, Z. Sun, B. Li, Z. Liu, D. Shen, Y. Ling, C. Wang, J. Wang, W. Gao, C. Yao, K. Yuan, H. Peng, Y. Tang, Y. Deng, G. Zheng, G. Zhou, D. Zhao, *ACS Central Science* **2015**, 1, 400.
- [36] Y. Liu, K. Lan, S. Li, Y. Liu, B. Kong, G. Wang, P. Zhang, R. Wang, H. He, Y. Ling, A. M. Al-Enizi, A. A. Elzatahry, Y. Cao, G. Chen, D. Zhao, *Journal of the American Chemical Society* **2017**, 139, 517.
- [37] J. J. Lin, L. Zhao, Y. U. Heo, L. Z. Wang, F. H. Bijarbooneh, A. J. Mozer, A. Nattestad, Y. Yamauchi, S. X. Dou, J. H. Kim, *Nano Energy* **2015**, 11, 557.
- [38] W. Shi, X. Zhang, J. Brillet, D. Huang, M. Li, M. Wang, Y. Shen, *Carbon* **2016**, 105, 387.
- [39] Q. Wang, L. Yuan, M. Dun, X. Yang, H. Chen, J. Li, J. Hu, *Applied Catalysis B: Environmental* **2016**, 196, 127.
- [40] B. Tan, X. Zhang, Y. Li, H. Chen, X. Ye, Y. Wang, J. Ye, *Chemistry* **2017**, 23, 5478.
- [41] T. R. Chetia, M. S. Ansari, M. Qureshi, *ACS Applied Materials & Interfaces* **2015**, 7, 13266.
- [42] Y. Zhao, Y. Zhang, H. Liu, H. Ji, W. Ma, C. Chen, H. Zhu, J. Zhao, *Chemistry of Materials* **2014**, 26, 1014.
- [43] Z. Jin, Y. X. Zhang, F. L. Meng, Y. Jia, T. Luo, X. Y. Yu, J. Wang, J. H. Liu, X. J. Huang, *Journal of Hazardous Materials* **2014**, 276, 400.
- [44] Z. Li, Y. Zhou, G. Xue, T. Yu, J. Liu, Z. Zou, *Journal of Materials Chemistry* **2012**, 22, 14341.
- [45] Y. Qiu, W. Chen, S. Yang, *Journal of Materials Chemistry* **2010**, 20, 1001.
- [46] E. Hosono, T. Tokunaga, S. Ueno, Y. Oaki, H. Imai, H. Zhou, S. Fujihara, *Crystal Growth and Design* **2012**, 12, 2923.
- [47] J. Y. Dong, C. H. Lin, Y. J. Hsu, S. Y. Lu, D. S. H. Wong, *CrystEngComm* **2012**, 14, 4732.
- [48] Q. P. Luo, B. Wang, Y. Cao, *Journal of Alloys and Compounds* **2017**, 695, 3324.
- [49] Y. Xu, W. Wen, J. M. Wu, *J Hazard Mater* **2018**, 343, 285.
- [50] Q. Dong, S. Yin, C. Guo, X. Wu, N. Kumada, T. Takei, A. Miura, Y. Yonesaki, T. Sato, *Applied Catalysis B: Environmental* **2014**, 147, 741.
- [51] S. Ghosh, M. Roy, M. K. Naskar, *Materials Letters* **2014**, 132, 98.
- [52] H. Tu, L. Xu, F. Mou, J. Guan, *J. Mater. Chem. A* **2016**, 4, 16562.
- [53] a) W. Wang, M. Dahl, Y. Yin, DOI: 10.1021/cm3030928, 2013; b) Y. Yin, R. M. Rioux, C. K. Erdonmez, S. Hughes, G. A. Somorjal, A. P. Alivisatos, *Science* **2004**, 304, 711.
- [54] a) J. Zhao, Y. Zou, X. Zou, T. Bai, Y. Liu, R. Gao, D. Wang, G. D. Li, *Nanoscale* **2014**, 6, 7255; b) H. Tu, L. Xu, F. Mou, J. Guan, *Chemical Communications* **2015**, 51, 12455.
- [55] L. Xu, F. X. Bu, M. Hu, C. Y. Jin, D. M. Jiang, Z. J. Zhao, Q. H. Zhang, J. S. Jiang, *Chem Commun (Camb)* **2014**, 50, 13849.



- [56] a) M. Valant, A. K. Axelsson, N. Alford, *Chem. Mater.* **2007**, 19, 5431; b) M. Thrall, R. Freer, C. Martin, F. Azough, B. Patterson, R. J. Cernik, *Journal of the European Ceramic Society* **2008**, DOI: 10.1016/j.jeurceramsoc.2008.03.029.
- [57] Q. Kuang, S. Yang, *ACS applied materials & interfaces* **2013**, 5, 3683.
- [58] C. Cheng, Y. Shi, C. Zhu, W. Li, L. Wang, K. K. Fung, N. Wang, *Physical Chemistry Chemical Physics* **2011**, 13, 10631.
- [59] K. Li, J. Liu, X. Sheng, L. Chen, T. Xu, K. Zhu, X. Feng, *Chemistry - A European Journal* **2018**, 24, 89.
- [60] H. Yu, S. Yan, P. Zhou, Z. Zou, *Applied Surface Science* **2018**, 427, 603.
- [61] M. Xu, P. Ruan, H. Xie, A. Yu, X. Zhou, *ACS Sustainable Chemistry and Engineering* **2014**, 2, 621.
- [62] Y. Dong, X. Fei, Y. Zhou, *Applied Surface Science* **2017**, 403, 662.
- [63] H. Xu, W. Wang, W. Zhu, *Microporous and Mesoporous Materials* **2006**, 95, 321.
- [64] Z. Wang, Z. Wang, H. Wu, X. W. Lou, *Sci Rep* **2013**, 3, 1391.
- [65] D. H. Son, S. M. Hughes, Y. Yin, a. Paul Alivisatos, *Science (New York, N.Y.)* **2004**, 306, 1009.
- [66] C. Bothe, A. Kornowski, H. Tornatzky, C. Schmidtke, H. Lange, J. Maultzsch, H. Weller, *Angew. Chem. Int. Ed.* **2015**, 54, 14183.
- [67] a) B. Zhang, Y. Jung, H. S. Chung, L. Van Vugt, R. Agarwar, *Nano Letters* **2010**, 10, 149; b) J. Y. Lee, D. S. Kim, J. Park, *Chemistry of Materials* **2007**, 19, 4663.
- [68] Z. Guo, Y. Su, Y.-X. Li, G. Li, X.-J. Huang, *Chemistry – A European Journal* **2018**, 24, 9877.
- [69] T. Butburee, Y. Bai, H. Wang, H. Chen, Z. Wang, G. Liu, J. Zou, P. Khemthong, G. Q. M. Lu, L. Wang, *Advanced Materials* **2018**, 30, 1.
- [70] F. Zhang, A. Yamakata, K. Maeda, Y. Moriya, T. Takata, J. Kubota, K. Teshima, S. Oishi, K. Domen, *J. Am. Chem. Soc.* **2012**, 134, 8348.
- [71] a) H. Wagata, N. Zettsu, A. Yamaguchi, H. Nishikiori, K. Yubuta, S. Oishi, K. Teshima, *Crystal Growth & Design* **2015**, 15, 124; b) S. Pokrant, S. Dilger, S. Landsmann, *Journal Of Materials Research* **2016**, 31, 1574.
- [72] L. Chen, H. Dai, Y. Zhou, Y. Hu, T. Yu, J. Liu, Z. Zou, *Chemical Communications* **2014**, 50, 14321.
- [73] Q. Han, Y. Zhou, L. Tang, P. Li, W. Tu, L. Li, H. Li, Z. Zou, *RSC Adv.* **2016**, 6, 90792.
- [74] L. Nasi, D. Calestani, F. Fabbri, P. Ferro, T. Besagni, P. Fedeli, F. Licci, R. Mosca, *Nanoscale* **2013**, 5, 1060.
- [75] L. De Marco, D. Calestani, A. Qualtieri, R. Giannuzzi, M. Manca, P. Ferro, G. Gigli, A. Listorti, R. Mosca, *Solar Energy Materials and Solar Cells* **2017**, 168, 227.
- [76] X. B. Jin, Y. X. Li, Y. Su, Z. Guo, C. P. Gu, J. R. Huang, F. L. Meng, X. J. Huang, M. Q. Li, J. H. Liu, *Nanotechnology* **2016**, 27, 1.
- [77] J. Sun, S. Tian, X. Cai, D. Xiong, S. K. Verma, Q. Zhang, W. Chen, M. Zhu, X. Zhao, *CrystEngComm* **2016**, 18, 8277.
- [78] R. G. Elliman, J. S. Williams, *Current Op. Sol. State Mat. Sci.* **2015**, 19, 49.
- [79] G. Liu, H. G. Yang, X. Wang, L. Cheng, J. Pan, G. Q. Lu, H.-M. Cheng, *J. Am. Chem. Soc.* **2009**, 131, 12868.
- [80] R. Asahi, T. Morikawa, H. Irie, T. Ohwaki, *Chemical Reviews* **2014**, 114, 9824.
- [81] a) S. K. Md Saad, A. Ali Umar, H. Quan Nguyen, C. Fu Dee, M. Mat Salleh, M. Oyama, *RSC Advances* **2014**, 4, 57054; b) M. Kitahara, Y. Shimasaki, T. Matsuno, Y. Kuroda, A. Shimojima, H. Wada, K. Kuroda, *Chemistry-a European Journal* **2015**, 21, 13073.
- [82] S. Liu, J. Yu, M. Jaroniec, *J. Am. Chem. Soc.* **2010**, 132, 11914.

- [83] M. Xing, Y. Zhou, C. Dong, L. Cai, L. Zeng, B. Shen, L. Pan, C. Dong, Y. Chai, J. Zhang, Y. Yin, *Nano Letters* **2018**, 18, 3384.
- [84] S. S. Shen, J. N. Niu, S. T. Shen, L. Zhou, H. Chen, S. H. Zhang, Y. H. Ling, Z. S. Liu, P. Z. Feng, X. M. Ou, Y. H. Qiang, *Journal Of Physics And Chemistry Of Solids* **2017**, 107, 75.
- [85] S. Yang, Y. Xu, Y. Cao, G. Zhang, Y. Sun, D. Gao, *RSC Advances* **2013**, 3, 21994.
- [86] S. Bai, J. Jiang, Q. Zhang, Y. Xiong, *Chemical Society Reviews* **2015**, 44, 2893.
- [87] S. Linic, P. Christopher, D. B. Ingram, *Nat. Mater.* **2011**, 10, 911.
- [88] A. L. Linsebigler, G. Lu, J. T. Yates, *Chem. Rev.* **1995**, 95, 735.
- [89] H. Mou, C. Song, Y. Zhou, B. Zhang, D. Wang, *Applied Catalysis B: Environmental* **2018**, 221, 565.
- [90] D. Chen, Z. Huang, H. Quan, S. Chen, J. Lin, X. Luo, L. Guo, *Science of Advanced Materials* **2016**, 8, 760.
- [91] M. Grundmann, *The physics of semiconductors: An introduction including devices and nanophysics*, Springer-Verlag Berlin Heidelberg, Germany **2006**.
- [92] J. Hou, Z. Wang, C. Yang, W. Zhou, S. Jiao, H. Zhu, *The Journal of Physical Chemistry C* **2013**, 117, 5132.
- [93] Y. Wang, Y. Deng, L. Fan, Y. Zhao, B. Shen, D. Wu, Y. Zhou, C. Dong, M. Xing, J. Zhang, *RSC Adv.* **2017**, 7, 24064.
- [94] F. Zhang, A. Yamakata, K. Maeda, Y. Moriya, T. Takata, J. Kubota, K. Teshima, S. Oishi, K. Domen, *J Am Chem Soc* **2012**, 134, 8348.
- [95] C. H. Park, C. M. Lee, J. W. Choi, G. C. Park, J. Joo, *Ceramics International* **2018**, 44, 1641.
- [96] J. Zhang, W. Zhao, Y. Xu, H. Xu, B. Zhang, *International Journal of Hydrogen Energy* **2014**, 39, 702.
- [97] a) J. N. Schrauben, R. Hayoun, C. N. Valdez, M. Braten, L. Fridley, J. M. Mayer, *Science (New York, N.Y.)* **2012**, 336, 1298; b) Z. Wang, C. Yang, T. Lin, H. Yin, P. Chen, D. Wan, F. Xu, F. Huang, J. Lin, X. Xie, M. Jiang, *Advanced Functional Materials* **2013**, 23, 5444.
- [98] X. Chen, L. Liu, F. Huang, *Chem. Soc. Rev.* **2015**, 44, 1861.
- [99] a) Z. Zhao, H. Tan, H. Zhao, Y. Lv, L.-J. Zhou, Y. Song, Z. Sun, *Chem. Commun.* **2014**, 50, 2755; b) A. Sinhamahapatra, J. P. Jeon, J. S. Yu, *Energy and Environmental Science* **2015**, 8, 3539.
- [100] H. Li, Z. Chen, C. K. Tsang, Z. Li, X. Ran, C. Lee, B. Nie, L. Zheng, T. Hung, J. Lu, B. Pan, Y. Y. Li, *J. Mater. Chem. A* **2014**, 2, 229.
- [101] S. H. S. Chan, T. Yeong Wu, J. C. Juan, C. Y. Teh, *Journal of Chemical Technology & Biotechnology* **2011**, 86, 1130.
- [102] A. Fujishima, K. Honda, *Nature* **1972**, 238, 37.
- [103] Y. Wenbo, R. Chamnan, A. P. S., S. Zixue, I. J. T. S., Z. Wuzong, *Advanced Functional Materials* **2009**, 19, 2826.
- [104] X. Zheng, Q. Kuang, K. Yan, Y. Qiu, J. Qiu, S. Yang, *ACS Applied Materials & Interfaces* **2013**, 5, 11249.
- [105] Y. Xu, W. Wen, J.-M. Wu, *Journal of Hazardous Materials* **2018**, 343, 285.
- [106] H. Xu, W. Wang, W. Zhu, *Microporous and Mesoporous Materials* **2006**, 95, 321.
- [107] K. Girija, S. Thirumalairajan, K. P. Astam, D. Mangalaraj, N. Ponpandian, C. Viswanathan, *Semicond. Sci. and Technol.* **2013**, 28, 035015.
- [108] S. Bharathi, D. Nataraj, D. Mangalaraj, Y. Masuda, K. Senthil, K. Yong, *Journal of Physics D: Applied Physics* **2010**, 43, 015501.
- [109] H. G. Cha, S. J. Kim, K. J. Lee, M. H. Jung, Y. S. Kang, *The Journal of Physical Chemistry C* **2011**, 115, 19129.
- [110] Y. Qiu, G.-L. Xu, Q. Kuang, S.-G. Sun, S. Yang, *Nano Research* **2012**, 5, 826.

- [111] H. Jiang, X. Meng, H. Dai, J. Deng, Y. Liu, L. Zhang, Z. Zhao, R. Zhang, *Journal of Hazardous Materials* **2012**, 217-218, 92.
- [112] L. Xu, F.-X. Bu, M. Hu, C.-Y. Jin, D.-M. Jiang, Z.-J. Zhao, Q.-H. Zhang, J.-S. Jiang, *Chemical Communications* **2014**, 50, 13849.
- [113] C. Li, G. Chen, J. Sun, J. Rao, Z. Han, Y. Hu, Y. Zhou, *ACS Applied Materials & Interfaces* **2015**, 7, 25716.
- [114] J. Niu, S. Shen, S. He, Z. Liu, P. Feng, S. Zhang, X. Ou, Y. Qiang, Z. Zhu, *Ceramics International* **2015**, 41, 11936.
- [115] J. Niu, S. Shen, L. Zhou, Z. Liu, P. Feng, X. Ou, Y. Qiang, *RSC Advances* **2016**, 6, 62907.
- [116] Z. Jin, Y.-X. Zhang, F.-L. Meng, Y. Jia, T. Luo, X.-Y. Yu, J. Wang, J.-H. Liu, X.-J. Huang, *Journal of Hazardous Materials* **2014**, 276, 400.
- [117] Z. Wang, Z. Wang, H. Wu, X. W. Lou, *Scientific Reports* **2013**, 3, 1391.
- [118] Q. Dong, S. Yin, C. Guo, X. Wu, N. Kumada, T. Takei, A. Miura, Y. Yonesaki, T. Sato, *Applied Catalysis B: Environmental* **2014**, 147, 741.
- [119] S. K. Md Saad, A. A. Umar, H. Q. Nguyen, C. F. Dee, M. M. Salleh, M. Oyama, *RSC Advances* **2014**, 4, 57054.
- [120] S. Yang, Y. Xu, Y. Cao, G. Zhang, Y. Sun, D. Gao, *RSC Advances* **2013**, 3, 21994.
- [121] J. Lai, K. V. P. M. Shafi, K. Loos, A. Ulman, Y. Lee, T. Vogt, C. Estournès, *Journal of the American Chemical Society* **2003**, 125, 11470.
- [122] T. Biying, Z. Xuehao, L. Yongjun, C. Hao, Y. Xiaozhou, W. Yun, Y. Jianfeng, *Chemistry – A European Journal* **2017**, 23, 5478.
- [123] H. Liu, M. Luo, J. Hu, T. Zhou, R. Chen, J. Li, *Applied Catalysis B: Environmental* **2013**, 140-141, 141.
- [124] J. Yang, D. Wang, H. Han, C. Li, *Accounts of Chemical Research* **2013**, 46, 1900.
- [125] K.-i. Katsumata, K. Sakai, K. Ikeda, G. Carja, N. Matsushita, K. Okada, *Materials Letters* **2013**, 107, 138.
- [126] L. Liu, Z. Ji, W. Zou, X. Gu, Y. Deng, F. Gao, C. Tang, L. Dong, *Acs Catalysis* **2013**, 3, 2052.
- [127] J. A. Maciá-Agulló, A. Corma, H. Garcia, *Chemistry—A European Journal* **2015**, 21, 10940.
- [128] D. Lu, S. Ouyang, H. Xu, D. Li, X. Zhang, Y. Li, J. Ye, *ACS Applied Materials & Interfaces* **2016**, 8, 9506.
- [129] L. Liu, S. Ouyang, J. Ye, *Angewandte Chemie International Edition* **2013**, 52, 6689.
- [130] D. Chen, Z. Huang, H. Quan, S. Chen, J. Lin, X. Luo, L. Guo, *Science of Advanced Materials* **2016**, 8, 760.
- [131] J. Hou, Z. Wang, C. Yang, W. Zhou, S. Jiao, H. Zhu, *The Journal of Physical Chemistry C* **2013**, 117, 5132.
- [132] J. Ran, J. Zhang, J. Yu, M. Jaroniec, S. Z. Qiao, *Chemical Society Reviews* **2014**, 43, 7787.
- [133] W. Li, Y. Bai, W. Zhuang, K.-Y. Chan, C. Liu, Z. Yang, X. Feng, X. Lu, *The Journal of Physical Chemistry C* **2014**, 118, 3049.
- [134] Y. Noda, B. Lee, K. Domen, J. N. Kondo, *Chemistry of Materials* **2008**, 20, 5361.
- [135] J. N. Kondo, K. Domen, *Chemistry of Materials* **2008**, 20, 835.
- [136] H. Tu, L. Xu, F. Mou, J. Guan, *Journal of Materials Chemistry A* **2016**, 4, 16562.
- [137] Q. Kuang, S. Yang, *ACS Applied Materials & Interfaces* **2013**, 5, 3683.
- [138] L. Hui, C. Xianliu, Y. Shicheng, L. Zhaosheng, Z. Zhigang, *European Journal of Inorganic Chemistry* **2014**, 2014, 3731.
- [139] W. Jiao, Y. Xie, R. Chen, C. Zhen, G. Liu, X. Ma, H.-M. Cheng, *Chemical Communications* **2013**, 49, 11770.

- [140] J. Zhao, Y. Zou, X. Zou, T. Bai, Y. Liu, R. Gao, D. Wang, G.-D. Li, *Nanoscale* **2014**, 6, 7255.
- [141] Q. Wu, S. Bao, B. Tian, Y. Xiao, J. Zhang, *Chemical Communications* **2016**, 52, 7478.
- [142] F. Zhang, A. Yamakata, K. Maeda, Y. Moriya, T. Takata, J. Kubota, K. Teshima, S. Oishi, K. Domen, *Journal of the American Chemical Society* **2012**, 134, 8348.
- [143] M. Hojamberdiev, H. Wagata, K. Yubuta, K. Kawashima, J. J. M. Vequizo, A. Yamakata, S. Oishi, K. Domen, K. Teshima, *Applied Catalysis B: Environmental* **2016**, 182, 626.
- [144] M. Qureshi, K. Takanabe, *Chemistry of Materials* **2017**, 29, 158.
- [145] a) N. Shehzad, M. Tahir, K. Johari, T. Murugesan, M. Hussain, *Journal of CO2 Utilization* **2018**, 26, 98; b) S. Zeng, P. Kar, U. K. Thakur, K. Shankar, *Nanotechnology* **2018**, 29, 052001; c) U. Ulmer, T. Dingle, P. N. Duchesne, R. H. Morris, A. Tavasoli, T. Wood, G. A. Ozin, *Nature Communications* **2019**, 10, 3169.
- [146] H. Yu, S. Yan, P. Zhou, Z. Zou, *Applied Surface Science* **2018**, 427, 603.
- [147] Q. Han, Y. Zhou, L. Tang, P. Li, W. Tu, L. Li, H. Li, Z. Zou, *RSC Advances* **2016**, 6, 90792.
- [148] B. Zhenfeng, Z. Jian, W. Jing, C. Fenglei, H. Yuning, Q. Xufang, C. Yong, S. Meiqing, L. Hexing, L. Yunfeng, *Angewandte Chemie International Edition* **2011**, 50, 1105.
- [149] J. Wang, Z. Bian, J. Zhu, H. Li, *Journal of Materials Chemistry A* **2013**, 1, 1296.
- [150] W. Zhao, C. Liu, L. Cao, X. Yin, H. Xu, B. Zhang, *RSC Advances* **2013**, 3, 22944.
- [151] M. M. Lee, J. Teuscher, T. Miyasaka, T. N. Murakami, H. J. Snaith, *Science* **2012**, 338, 643.
- [152] Q. Jiang, Y. Zhao, X. Zhang, X. Yang, Y. Chen, Z. Chu, Q. Ye, X. Li, Z. Yin, J. You, *Nat. Photon.* **2019**, 13, 460.
- [153] P. Atienzar, T. Ishwara, B. N. Illy, M. P. Ryan, B. C. O'Regan, J. R. Durrant, J. Nelson, *Journal of Physical Chemistry Letters* **2010**, 1, 708.
- [154] P. Roy, D. Kim, K. Lee, E. Spiecker, P. Schmuki, *Nanoscale* **2010**, 2, 45.
- [155] K. M., N. K., N. L., *Advanced Materials* **2007**, 19, 3425.
- [156] a) L. I. Halaoui, N. M. Abrams, T. E. Mallouk, *The Journal of Physical Chemistry B* **2005**, 109, 6334; b) F. Ramiro-Manzano, P. Atienzar, I. Rodriguez, F. Meseguer, H. Garcia, A. Corma, *Chem. Commun.* **2007**, 3, 242.
- [157] K. Zhu, N. R. Neale, A. Miedaner, A. J. Frank, *Nano Letters* **2007**, 7, 69.
- [158] B. O'Regan, M. Grätzel, *Nature* **1991**, 353, 737.
- [159] U. Bach, D. Lupo, P. Comte, J. E. Moser, F. Weissörtel, J. Salbeck, H. Spreitzer, M. Grätzel, *Nature* **1998**, 395, 583.
- [160] S. Pitchaiya, M. Natarajan, A. Santhanam, V. Asokan, A. Yuvapragasam, V. Madurai Ramakrishnan, S. E. Palanisamy, S. Sundaram, D. Velauthapillai, *Arabian J. Chem.* **2018**, In Press.
- [161] A. Kojima, K. Teshima, Y. Shirai, T. Miyasaka, *Journal of the American Chemical Society* **2009**, 131, 6050.
- [162] H. J. Snaith, *The Journal of Physical Chemistry Letters* **2013**, 4, 3623.
- [163] H.-S. Kim, C.-R. Lee, J.-H. Im, K.-B. Lee, T. Moehl, A. Marchioro, S.-J. Moon, R. Humphry-Baker, J.-H. Yum, J. E. Moser, M. Grätzel, N.-G. Park, *Scientific Reports* **2012**, 2, 591.
- [164] H. Yu, L. Wang, M. Dargusch, *Solar Energy* **2016**, 123, 17.
- [165] E. J. W. Crossland, N. Noel, V. Sivaram, T. Leijtens, J. A. Alexander-Webber, H. J. Snaith, *Nature* **2013**, 495, 215.
- [166] H. G. Yang, C. H. Sun, S. Z. Qiao, J. Zou, G. Liu, S. C. Smith, H. M. Cheng, G. Q. Lu, *Nature* **2008**, 453, 638.

- [167] C. Y. Jiang, W. L. Koh, M. Y. Leung, S. Y. Chiam, J. S. Wu, J. Zhang, *Applied Physics Letters* **2012**, 100, 113901.
- [168] G. Lu, A. Linsebigler, J. T. Yates, *The Journal of Physical Chemistry* **1994**, 98, 11733.
- [169] S. Yang, Y. C. Zheng, Y. Hou, X. H. Yang, H. G. Yang, *Physical Chemistry Chemical Physics* **2014**, 16, 23038.
- [170] M. Xu, P. Ruan, H. Xie, A. Yu, X. Zhou, *ACS Sustainable Chemistry & Engineering* **2014**, 2, 621.
- [171] C. Helmut, A. Markus, *Angewandte Chemie International Edition* **2005**, 44, 5576.
- [172] J. Lin, L. Zhao, Y.-U. Heo, L. Wang, F. H. Bijarbooneh, A. J. Mozer, A. Nattestad, Y. Yamauchi, S. X. Dou, J. H. Kim, *Nano Energy* **2015**, 11, 557.
- [173] K. Li, J. Liu, X. Sheng, L. Chen, T. Xu, K. Zhu, X. Feng, *Chemistry – A European Journal* **2018**, 24, 89.
- [174] a) Z. Bian, J. Zhu, J. Wen, F. Cao, Y. Huo, X. Qian, Y. Cao, M. Shen, H. Li, Y. Lu, *Angewandte Chemie International Edition* **2011**, 50, 1105; b) X. Feng, K. Zhu, A. J. Frank, C. A. Grimes, T. E. Mallouk, *Angewandte Chemie International Edition* **2012**, 51, 2727.
- [175] Z. Zhu, X. Zheng, Y. Bai, T. Zhang, Z. Wang, S. Xiao, S. Yang, *Physical Chemistry Chemical Physics* **2015**, 17, 18265.
- [176] S. Ito, P. Liska, P. Comte, R. Charvet, P. Pechy, U. Bach, L. Schmidt-Mende, S. M. Zakeeruddin, A. Kay, M. K. Nazeeruddin, M. Gratzel, *Chem. Commun.* **2005**, 34, 4351.
- [177] a) Q. Zhang, C. S. Dandeneau, X. Zhou, G. Cao, *Advanced Materials* **2009**, 21, 4087; b) D. C. Look, D. C. Reynolds, J. R. Sizelove, R. L. Jones, C. W. Litton, G. Cantwell, W. C. Harsch, *Solid State Communications* **1998**, 105, 399.
- [178] L. De Marco, D. Calestani, A. Qualtieri, R. Giannuzzi, M. Manca, P. Ferro, G. Gigli, A. Listorti, R. Mosca, *Solar Energy Materials and Solar Cells* **2017**, 168, 227.



Jinan Niu received his Bachelor of Materials Science and Engineering from China University of Mining and Technology (CUMT) in 2004. He obtained his Ph.D degree in Mineral Materials Engineering at CUMT in 2010. He had stayed at Instituto de Tecnología Química (ITQ) in Spain for one year as an academic visiting scholar (2017.10-2018.10). Currently, he is an associate professor at CUMT. His current research interests primarily focus on (1) synthesis of porous photo/electro-catalysts towards environmental remediation and energy

regeneration; and (2) regulation of interface reaction between clay and other phases towards loading, adsorption, catalysis etc. applications.



Hermenegildo García is full Professor at the Instituto de Tecnología Química of the Technical University of Valencia and Honorary Adjunct Professor at the Center of Excellence in Advanced Materials Research of King Abdullaziz University. Prof. Garcia has been active in the field of heterogeneous catalysis working with porous catalysts and NPs, as well as in the photocatalytic production of solar fuels. Prof. Garcia is doctor Honoris Causa from the University of Bucharest and the recipient of the 2011 Janssen-Cilag award given by the Spanish Royal Society of Chemistry and the 2015 Jaume I prize for Novel Technologies.



Josep Albero obtained the Chemical Engineering degree from the Jaume I University of Castellon (Spain) in 2005. Later he obtained his M.Sc. degree from Rovira I Virgili University in 2009. He worked in the synthesis and characterization of nanocrystalline semiconductor quantum dots for photovoltaic applications when received his PhD in the group of E. Palomares at ICIQ. Afterwards he joined Prof. Garcia group in ITQ as postdoctoral fellow. His research interest is the photo-induced charge transfer reactions in nanostructured materials and their applications in renewable energies and solar fuels production.



Pedro Atienzar obtained his Ph.D. (2007) from the Instituto de Tecnología Química (UPV-CSIC) at the Universidad Politécnica de Valencia under the supervision of Prof. Hermenegildo García. Afterwards he joined the group of Prof. Jenny Nelson in the Department of Physics at Imperial College London, where he worked as a post-doctoral fellow (2007–2009) in the field of hybrid and polymeric photovoltaic devices. Currently, he is Tenured Scientific of CSIC (Spanish National Research Council) at the Instituto de Tecnología Química. His major research interest is the development of photoactive materials for optoelectronics, photonics and energy.

The table of contents entry should be 50–60 words long and should be written in the present tense and impersonal style (i.e., avoid we). The text should be different from the abstract text.

**Keyword:** photocatalysis, single crystal, environmental remediation, photovoltaics, solar fuels

Jinan Niu, Josep Albero, Pedro Atienzar and Hermenegildo García\*

**Porous single crystal based inorganic semiconductor photocatalysts for energy production and environmental remediation: preparation, modification and applications**

ToC figure ((Please choose one size: 55 mm broad  $\times$  50 mm high **or** 110 mm broad  $\times$  20 mm high. Please do not use any other dimensions))

